

Surfactant-Assisted Chemical Vapour Deposition of Gold Nanoplates with Highly Smooth Surface

by

Weipeng Zhang M. Eng.; B. Sc.

A thesis submitted to the Faculty of Graduate and Postdoctoral Affairs in partial fulfillment of the requirements for the degree of

Master of Science

in

Chemistry

Carleton University
Ottawa, Ontario

©2016, Weipeng Zhang

Abstract

Tetrahydrothiophene (THT), as a surfactant, was studied for the shape control of gold nanoplates via chemical vapour deposition (CVD). Dense gold nanoplates (6 μm) with a highly smooth surface were deposited by using 1,3-diisopropyl-imidazol-2-ylidene gold (I) hexamethyldisilazide at 370°C, with 45 mtorr of THT. Similar but isolated nanoplates were attained with 15-35 mtorr of THT at 430°C. Along with single-crystalline structure, a $\{111\}$ plane of the nanoplates was confirmed by determining the gold stacking fault, $\frac{1}{3}\{422\}$ diffractions in selected area electron diffraction (SAED) patterns. Purity of the nanoplates was shown by energy dispersive X-ray spectroscopy (EDS) and X-ray photoelectron spectroscopy (XPS) analysis, both showing gold metal without significant sulfur impurities. THT preferably capped the gold $\{111\}$ plane which lowered the surface energy, leading to a smooth surface and large size. Gold precursor supply influenced the particle size and mechanism of the crystal growth, as well as the particle density.

Acknowledgements

First of all, I would like to give my most sincerely thank to my parents for the support of my study abroad, no matter on spirit or finance. I love you, forever.

Second, thanks, Seán, my supervisor, as well as the first Canadian I meet. I will never forget your professional attitudes to science, as well as your height, tattoo, the love for wine, also your reaction towards the DEVIL EGGS... Thank you.

Third, thanks, everybody in the Barry Lab. I'm grateful for your help for the lab works, no matter on chemistry, housework, or just cleaning. Matt, especially, thanks to be my helper for this two year.

Finally, thanks, all my friends, from all over the world.

好人一生平安。Safety would be along with a kind person for all his life.

Table of Contents

Abstract.....	ii
Acknowledgements	iii
Table of Contents	iv
List of Figures and Tables.....	vii
1 Introduction.....	1
1.1 Gold Films.....	1
1.2 Gold Nanoplates.....	2
1.3 Chemical Vapour Deposition.....	3
1.3.1 Precursors and Reductants.....	3
1.3.2 Steps and Processes	4
1.3.3 CVD Kinetics.....	5
1.4 Crystal Growth Mechanism	6
1.4.1 Small Nanoparticle Growth	7
1.4.2 Shaped Crystal Growth.....	10
1.5 Growth Directing Surfactants.....	18
1.5.1 Selective Adsorption.....	19
1.5.2 Self-Assembled Monolayers.....	20
1.5.3 Hydrophile Lipophile Balance.....	21
1.6 Surfactant-Assisted CVD.....	22
1.7 Flow Conditions.....	24
1.8 Project Overview.....	26

2	Screening Gold CVD	29
2.1	System Construction	29
2.1.1	Separated-Feeding-Route Apparatus	29
2.1.2	Combined-Feeding-Route Apparatus	31
2.2	Test Depositions.....	35
2.2.1	Control Run	35
2.2.2	Blank Run	37
2.3	Surfactant Selection	38
2.3.1	Tetrahydrofuran	38
2.3.2	1,3-Di-t-butyl-Imidazol-2-Ylidene Carbene	40
2.3.3	Tetrahydrothiophene.....	45
2.4	Summary	47
3	THT-Assisted Gold CVD.....	48
3.1	Structural Investigation	48
3.1.1	Morphology	48
3.1.2	Elemental Analysis	50
3.1.3	Crystalline Structural Analysis	51
3.2	Role of Surfactant	54
3.2.1	Pressure Effects.....	54
3.2.2	Surface Morphology	59
3.2.3	Particle Size	68
3.2.4	Surfactant Residual	74
3.3	Gold Supply Control	77

3.3.1	Flake Density	77
3.3.2	Shape Preference.....	79
3.3.3	Particle Size	80
3.4	Summary	84
4	Conclusions.....	86
5	Future Work.....	88
6	Experimental Section.....	89
	References	93

List of Figures and Tables

Figure 1. Schematic diagram for the process of gold CVD.....	5
Figure 2. Deposition rate-temperature relation curve of CVD.	6
Figure 3. Models for typical shapes of small metallic nanocrystals.	8
Figure 4. Growth models of small nanoparticles with stacking fault.	9
Figure 5. Possible models for the gold stacking fault.....	10
Figure 6. Growth model of nanocubes.....	11
Figure 7. Growth model of nanowires.....	12
Figure 8. Growth models of triangular and hexagonal nanoplates.	14
Figure 9. Growth model of nanorods.....	15
Figure 10. Growth and reconstruction models of $\{110\}$ elongated nanorods.	16
Figure 11. Growth model of nanostars.	17
Figure 12. Growth model of branched particles.	18
Figure 13. Schematic Diagram for the growth of shaped gold particles via SAM.....	21
Figure 14. Knudsen numbers and flow conditions.	26
Figure 15. Schematic diagram for synthesis of the gold precursor.....	27
Figure 16. Schematic diagram for the separated-feeding-route CVD apparatus.....	31
Figure 17. Diagrams for the combined-feeding-route CVD apparatus.....	33
Figure 18. Schematic diagram for the nitrogen flow CVD apparatus.	34
Figure 19. Locations of the gold depositions.....	35
Figure 20. SEM images of gold particles deposited at $T_d = 430^\circ\text{C}$	36
Figure 21. SEM images of gold particles deposited at $T_d = 430^\circ\text{C}$	37
Figure 22. THF pressure-time relation curves.	39

Figure 23. Schematic diagram for reaction network of THF via H-abstraction.	40
Figure 24. Diagram of 1,3-di-t-butyl-imidazol-2-ylidene carbene (NHC).	41
Figure 25. SEM images of gold particles deposited at $T_d = 430^\circ\text{C}$ with NHC.	42
Figure 26. Schematic diagram for NHC-assisted gold CVD.	44
Figure 27. SEM images of gold particles deposited at $T_d = 430^\circ\text{C}$ with THT.	46
Figure 28. SEM images of gold particles deposited at $T_d = 370^\circ\text{C}$ with THT.	49
Figure 29. EDS spectrum of the gold nanoplate deposited at $T_d = 370^\circ\text{C}$, $P_{\text{THT}} = 45$ mtorr.	50
Figure 30. TEM image and SAED patterns of the gold nanoplate deposited at $T_d = 370^\circ\text{C}$, $P_{\text{THT}} = 45$ mtorr.	51
Figure 31. Facet identification of the gold nanoplate deposited at $T_d = 370^\circ\text{C}$, $P_{\text{THT}} = 45$ mtorr.	52
Figure 32. Model of spatial relationship between the electron beam and the gold nanoplates.	54
Figure 33. SEM images of gold particles deposited at $T_d = 370^\circ\text{C}$ with nitrogen or THT.	55
Figure 34. SEM images of gold particles deposited at $T_d = 430^\circ\text{C}$ with nitrogen or THT.	57
Figure 35. SEM images of gold particles deposited at $T_d = 430^\circ\text{C}$ with THT.	60
Figure 36. SEM images of gold particles deposited at $T_d = 370^\circ\text{C}$ with THT.	62
Figure 37. Growth model of the blank gold CVD.	63
Figure 38. Growth model of the gold films with partially capped by THT.	64
Figure 39. Growth model of the gold films with fully capped THT.	65

Figure 40. Models of bonding between gold and THT.....	66
Figure 41. <i>HLB</i> values of compounds with circled hydrophilic atoms.....	67
Figure 42. Models of dipoles for the surfactant molecules.....	68
Figure 43. SEM images of gold particles deposited at $T_d = 430^\circ\text{C}$ with THT.....	69
Figure 44. SEM images of gold particles deposited at $T_d = 370^\circ\text{C}$ with THT.....	71
Figure 45. Growth models of the gold films with THT.....	73
Figure 46. EDS spectra of gold particles at $P_{\text{THT}} = 45$ mtorr.....	75
Figure 47. XPS spectrum of the gold films deposited at $T_d = 370^\circ\text{C}$, $P_{\text{THT}} = 45$ mtorr....	76
Figure 48. SEM images of gold particles at $P_{\text{THT}} = 35$ mtorr.....	78
Figure 49. SEM images of gold particles with THT.....	80
Figure 50. SEM images of gold particles deposited at $T_d = 370^\circ\text{C}$ with THT.....	81
Figure 51. SEM images of gold particles deposited at $T_d = 310^\circ\text{C}$ with THT.....	82
Figure 52. Surface area-THT pressure relation curve on fine gold particles.....	84
Table 1. Properties and applications of surfactants with different <i>HLB</i> values.....	22
Table 2. Knudsen flow data of gases.	58

1 Introduction

1.1 Gold Films

Gold is a useful metallic material for numerous applications. Gold films are potentially interesting for developments in biosensors,¹⁻³ catalysts⁴⁻⁶ and photonic materials,^{7,8} due to the excellent conductivity, conversion efficiency and anisotropies of metallic particles. Gold particles in surface plasmon resonance (SPR) applications have seen a growing interest because of the significant interactions with light, enhancing the availability of photovoltaic technology in different fields.⁹⁻¹² It can be expected that creative discoveries for gold metal nanofabrication and applications are on the horizon since it is valuable and promising for scientific applications.

Shape control is a fundamental goal of metallic materials science.¹³ Gold films with particles in different shapes have a variety of useful properties. A single gold nanorod has been shown to, *vitro* and *in vivo*, act as a two-photon luminescence reagent providing high contrast and having a low quenching probability.¹⁴ The achievement of gold nanoplasmonic probes with platinum implanted on gold surfaces made it possible to monitor the process of catalytic reactions, based on changes in refractive index.¹⁵ An innovative mechanism of drug release was established using polymer-coated gold nanocages, melting the polymer coating to release a captured payload by highly efficient photo-thermal conversion.¹⁶ Gold "bowties" were synthesized to generate ultraharmonics with the help of field-enhanced effects.¹⁷ Thus, morphological research of gold particles is an essential branch of nanotechnology.

1.2 Gold Nanoplates

Gold nanoplates receive abundant attention for their outstanding optical and conductive performance. With a smooth plane on the atomic level, a thin single-crystalline layer is an ideal target for plasmonic substrates with a large patterning area.¹⁸ The splendidly smooth surface, as well as the high aspect ratio, makes gold nanoplates adept at conductivity, reflectivity¹⁹ and chemical stability,²⁰ for larger contact areas.²¹ Thus, gold nanoplates have significant potentials for SPR applications,^{22,23} and surface-enhanced raman scattering (SERS),^{24,25} as well as electronic conductive adhesives (ECAs).²⁶

Since first reported in 2004, much work had been done on preparation of gold nanoplates.²⁷ Machinable single-crystalline gold nanoplates were prepared through chemical reduction showing a two-step growth model in solution.²⁸ Other research closely detailed shape control by using poly (vinylpyrrolidone) (PVP), in addition to the plasmon resonance.²⁹ With cetyltrimethylammonium bromide (CTAB), triangular gold nanoplates were synthesized in high yield and tunable size distribution, investigated for plasmonic properties by UV-Vis-NIR adsorption spectroscopy.³⁰ A method for thickness control was demonstrated recently using HAuCl_4 , CTAB and ascorbic acid.³¹

However, vapour depositions of gold nanoplates have been seldom mentioned in the literature compared with liquid-phase chemistry. Though successfully produced by CVD, gold particles were still generated with less control.³² Consequently, it would be a breakthrough if a reliable route was discovered for controllable gold nanostructure fabrication via deposition methods.

1.3 Chemical Vapour Deposition

Chemical vapour deposition (CVD) is a typical technology for producing metallic films.³³ Unlike physical vapour deposition (PVD), CVD involves chemical reactions during the deposition including precursor decomposition and surface reactions, as well as adsorption and desorption.³⁴ When employed into a furnace tube, gaseous precursors are delivered at high temperatures and arrive at the surface of substrates via diffusion. By use of a reducing gas or heat (or both), precursors are reduced to generate crystal nuclei that then form continuous films through continued chemical reduction.³⁵

1.3.1 Precursors and Reductants

Metal containing precursors, usually inorganic or organ-metallic complexes, are used as sources to make metallic films by CVD. Apart from the central metallic ions, organic ligands often work as stabilizers to allow film deposition in mild conditions.³⁶⁻³⁸ It is an overall requirement that precursors should be highly volatile and thermally stable since a high temperature is often used during depositions.³⁹ Chemical reactivity and low melting points are also criteria for the selection of precursors.

For gold CVD, it is not recommended to use reduction gas, especially hydrogen, as a reductant during depositions because hydrogen can reduce gold precursors at an extremely fast rate at low temperatures, even room temperature. This would lead to an uncontrollable reduction during CVD, making the deposition hard to control.

1.3.2 Steps and Processes

A brief process on gold CVD is shown in Figure 1.^{32,35} Volatile precursors are evaporated and introduced into the furnace to form a main gas flow within the apparatus (1). At high temperatures, gas phase reactions occur and can produce surface reactive compounds which are able to interact with the substrates (2). Such a process is sustainable and simultaneous because of the continual input of precursor gas. The surface reactive products are physisorbed on the surface via gas phase transportation (3). Surface diffusion can occur on surface-activated molecules. The metallic centers residing on the surface can become immobilized by reaction with hydroxyl (or other) groups on the surface through chemisorption (4). An equilibrium between adsorption and desorption of the molecules can occur, which is influenced by temperature (5). In a furnace, reactive gold (I) surface groups can be reduced to form small gold nanoparticles, releasing oxidized ligands to the atmosphere (6).

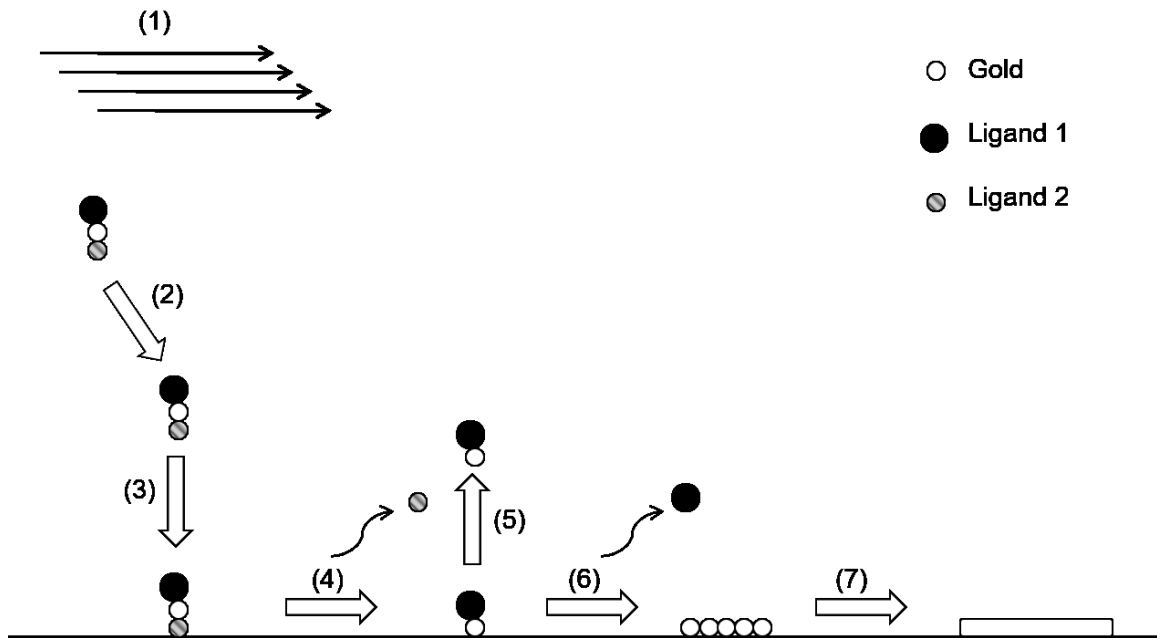


Figure 1. Schematic diagram for the process of gold CVD. (1) main gas flow; (2) gas phase reactions; (3) gas phase transportation; (4) surface diffusion; (5) precursor desorption; (6) surface reactions; (7) continuous film formation. Reproduced with permission from Reference 32 and 35.

1.3.3 CVD Kinetics

Generally, there are two main types of film deposition rate during the kinetic process of CVD, called the surface-reaction rate limited regime and mass-transport limited regime (Figure 2).⁴⁰ At lower temperatures, the deposition rate is mainly influenced by surface reactions because the reaction rate is low but larger amounts of precursors exist just above the surface (1). Thus, the deposition rate (R_D) would be sensitive to temperature, leading to difficulties in deposition control. On the contrary, if the temperature is higher, reactants will be quickly consumed because of a faster surface. The deposition rate in this case depends on diffusion, as mass transport process, with less response to changes in temperature (2). It could be, therefore, possible to control film depositions for uniformed

morphology since a (unavoidable) temperature gradient does not seriously impact film growth.

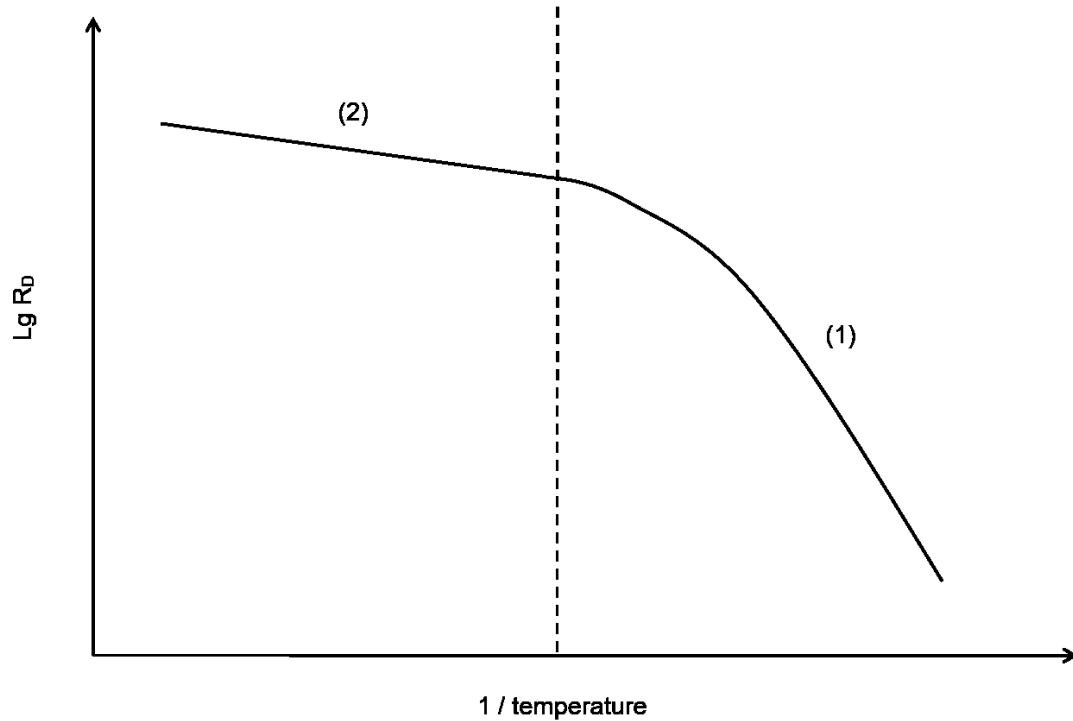


Figure 2. Deposition rate-temperature relation curve of CVD. (1) surface-reaction rate limited; (2) mass-transport limited. Reproduced with permission from Reference 40.

1.4 Crystal Growth Mechanism

Crystal growth of noble metals is an essential aspect of nanotechnology. It is typically divided into two different stages, the establishment of small nanoparticulate nucleation points (crystal seeds) and shaped crystal formation.⁴¹

1.4.1 Small Nanoparticle Growth

Due to the tiny size of nanoparticle seeds, structural fluctuations easily occur during particle formation in moderate conditions, even at room temperature, because the total surface energy of different morphologies are so similar that the energy barrier between them are low.⁴² In addition, the oscillation rate between different seed morphologies rises significantly with decreasing size.

Shapes of single-crystalline materials, especially face-centered cubic (FCC) noble metals, are usually predicted by the Wulff condition resulting in a series of polyhedrons (Figure 3).⁴³ The increasing order of atomic surface energy for FCC facets is $\gamma_{(111)} < \gamma_{(100)} < \gamma_{(110)}$. The Wulff model predicts a truncated octahedron with hexagonal (100) and square (111) facets when $\gamma_{(110)}/\gamma_{(111)} \cong \sqrt{3/2}$ (Figure 3a), while the less stable (110) facets would appear otherwise (Figure 3b).⁴⁴ Tetrahedron (Figure 3c) is a typical shape of small metallic crystals coming from multiply folded symmetry (Figure 3d, e).^{44,45} A special decahedral structure can also be found where (111) facets formed boundaries of the decahedron (Figure 3f) to further lower surface energy.⁴⁶⁻⁴⁸

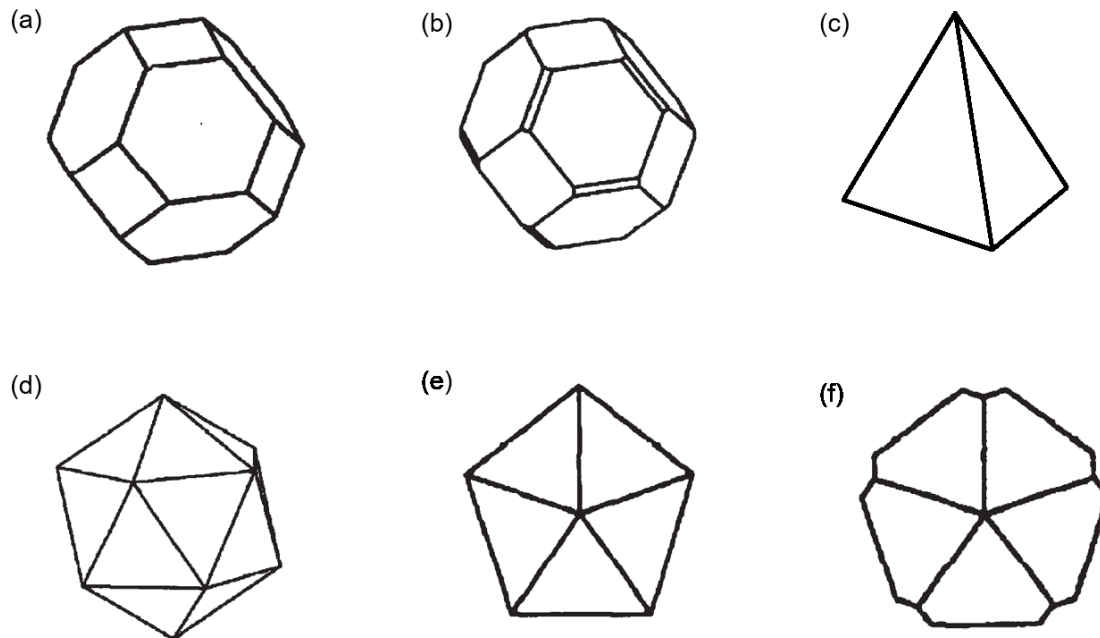


Figure 3. Models for typical shapes of small metallic nanocrystals. (a) truncated octahedron; (b) truncated octahedron with extra (110) truncations; (c) tetrahedron; (d) icosahedron; (e) decahedron; (f) Mark's decahedron. Reproduced with permission from Reference 41 and 44.

Some metals, such as gold, silver and copper, are known to form triangular nuclei with a $\{111\}$ face via stacking faults (Figure 4).⁴⁹ The relatively small atomic radii of these metals results in a low stacking fault energy, allowing this uncommon morphology.⁵⁰ So the tetrahedral metallic seeds (Figure 4d) more easily produce stacking faults by reconstructing atomic arrangement within nanocrystals. Two possible models for stacking fault formation in gold nanocrystals have been proposed: one with a ledge facing an edge (*V*-ledge, Figure 5a), and another one with a ledge facing a vertex (*I*-ledge, Figure 5b).⁵¹ It was calculated that the energy of a *V*-ledge is 0.05 eV/atomic layer, compared to 0.12 eV/atomic layer for an *I*-ledge, because those models formed different angles of the facets, 70.5° and 109.5° for *V*-ledge and *I*-ledge respectively. Thus, the *V*-ledge model is more reasonable for the formation of gold stacking faults.

There are three concave edges generated within a twinned tetrahedral crystal (Figure 4c) which contain a single stacking fault, making these the activated sites for deposition during the crystal growth. The concavities, therefore, grow in a much faster rate than the convex edges, and then small nanoparticle flakes (Figure 4d, e) can be obtained.⁴⁵

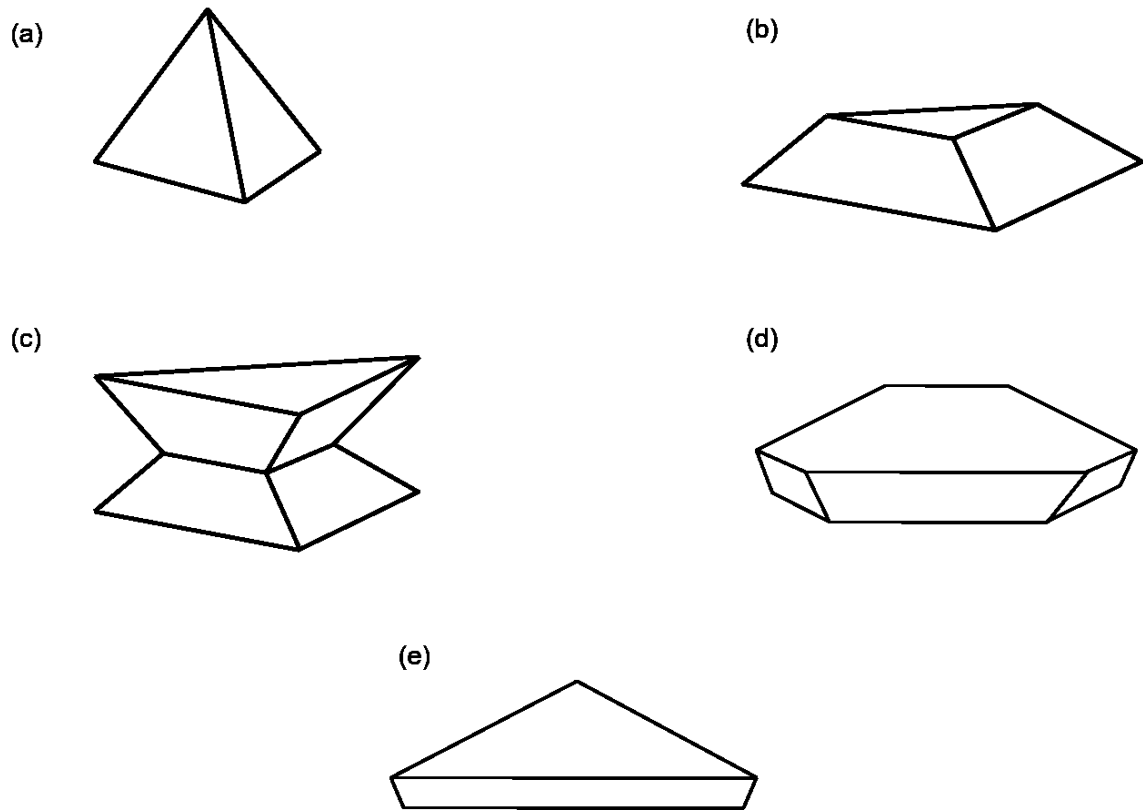


Figure 4. Growth models of small nanoparticles with stacking fault. (a) tetrahedral nanocrystals; (b) nanocrystals with stacking fault; (c) twinned crystal with stacking fault; (d) hexagonal crystal seed; (e) triangular crystal seed. Reproduced with permission from Reference 41 and 49.

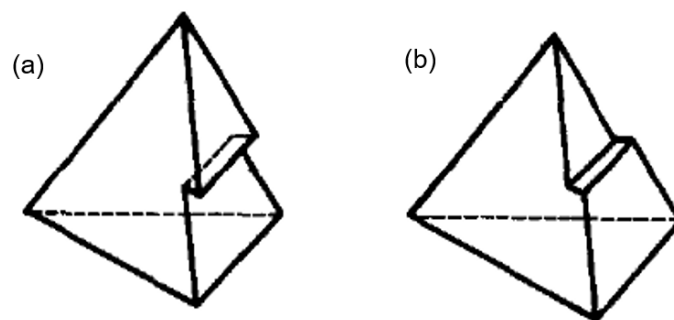


Figure 5. Possible models for the gold stacking fault. (a) *V*-ledge; (b) *I*-ledge. Reproduced with permission from Reference 51.

1.4.2 Shaped Crystal Growth

Once nucleated, nanocrystals with a given shape may grow into larger nanostructures with different shapes depending on the growth conditions. Here the key factor for shape control is lower potential surface energy.⁴⁴ In the following section, several typical mechanisms for producing nanocubes, nanowires, nanoplates, nanorods, nanostars, and branched particles will be outlined.

1) *Nanocubes*

Nanocubes with $\{100\}$ facets have been known for a long time.^{52,53} Xia's research group first demonstrated the synthesis of single-crystalline silver nanocubes with exclusively $\{100\}$ facets.⁵⁴ The subsequent observation of truncated nanocubes was seen with a lower ratio of $\{220\}$ to $\{111\}$ signal intensities in the X-ray diffratogram (XRD). Based on this discovery, it was inferred that nanocubes could be obtained by the selective growth of $\{111\}$ facets, which grow into the eight vertices of the cube (Figure 6).⁴⁵

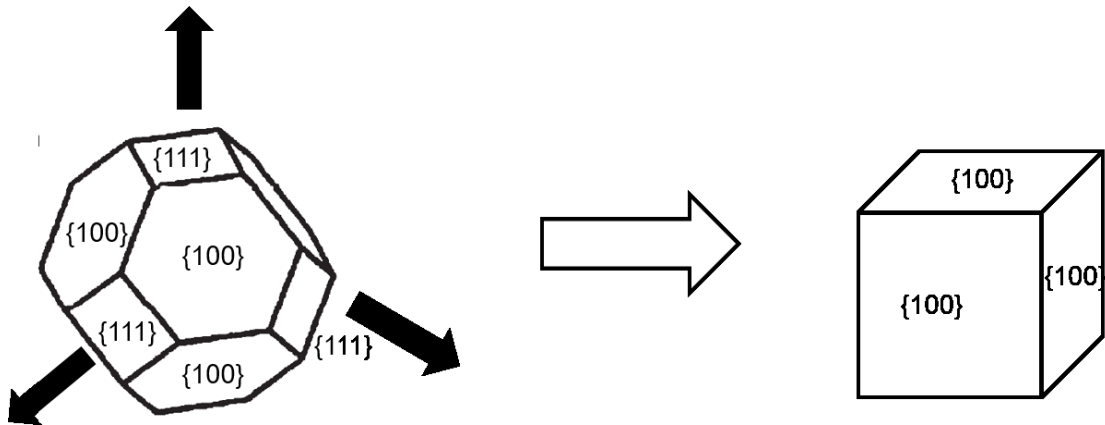


Figure 6. Growth model of nanocubes. Reproduced with permission from Reference 45.

2) Nanowires

Nanowires are very popular for their ability to make porous structures leading to large surface area which is useful for sensors and catalysts.^{55,56} Nanowires with a pentagonal cross-section and a $\langle 110 \rangle$ growth direction are common for gold (Figure 7a).⁵⁷ These grow from decahedral seeds, which are composed of five tetrahedral crystallites twinned together along $\{111\}$ facets. A possible mechanism was revealed when a small piece of crystal attached to the incomplete decahedron was seen to become a fast-growing side (Figure 7b).⁵⁸ Thus, the elongated growth was templated by twinned decahedron with selectively growth at the convex edges, assisted by a surfactant specific to $\{100\}$ coverage.

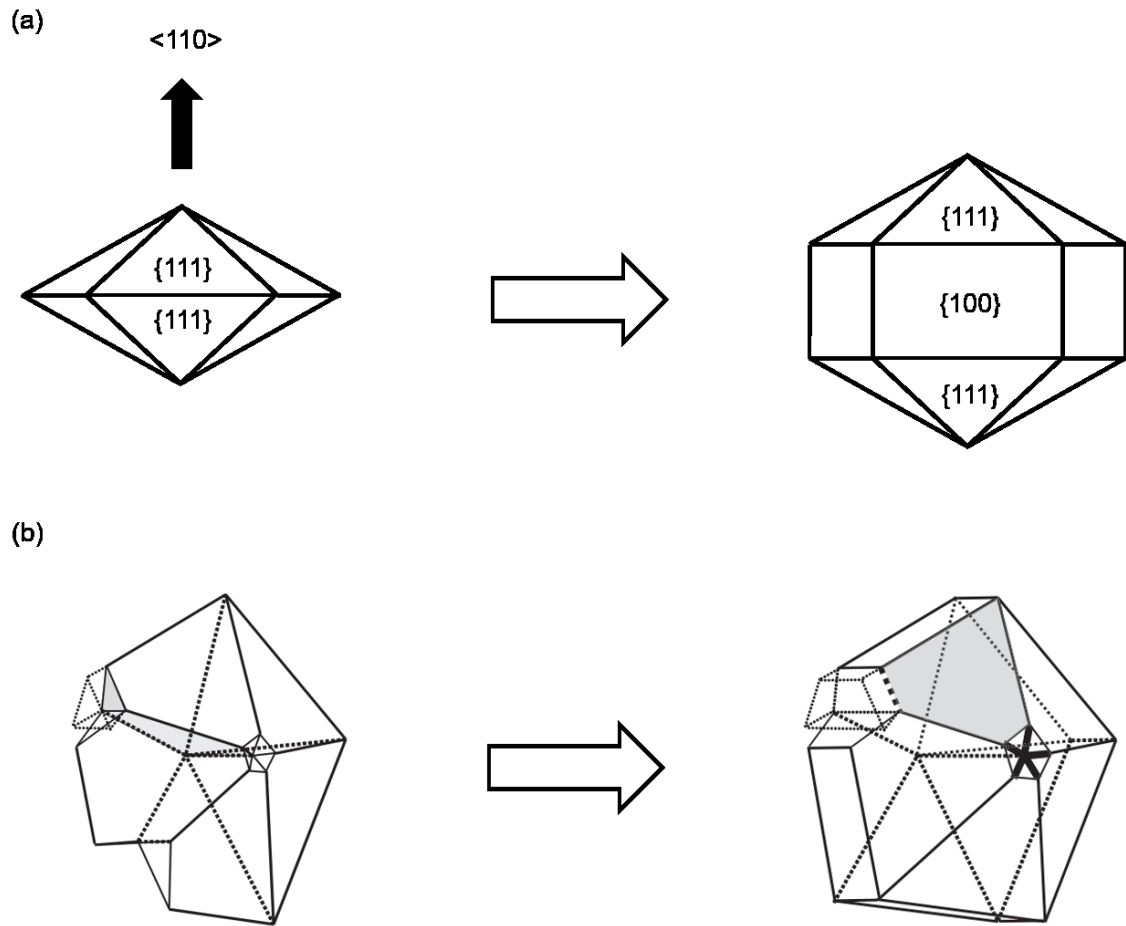


Figure 7. Growth model of nanowires. (a) growth direction of nanowires; (b) twinning model of the elongated growth. Reproduced with permission from Reference 45 and 58.

3) Nanoplates

Hexagonal and triangular nanoplates are grown from seed crystals containing one or more parallel stacking faults in the $\{111\}$ plane.⁵⁹ The higher surface energy at the stacking fault causes preferred growth in that plane.⁶⁰ Growth anisotropy is enhanced when the $\{111\}$ facets of the growing nanoplate are selectively stabilized by a growth-directing surfactant.

The shape of the nanoplate (hexagonal or triangular) depends on the number of stacking faulted twinned crystals.⁵⁸ Triangular nanoplates are generated from singly-twinned seed crystals (Figure 8a-c); while hexagonal nanoplates are generated from doubly-twinned hexagonal seeds (Figure 8d-f). The singly-twinned seed crystal possesses three concave edges and three convex edges, defined as concave (A) and convex (B), respectively. Growth on concave (A) is much faster than on convex (B) because of its higher surface energy.⁶¹ In contrast, the doubly-twinned seed crystal possesses six equivalent edges composed of both concave and convex regions, leading to a similar growth rate at all edges.

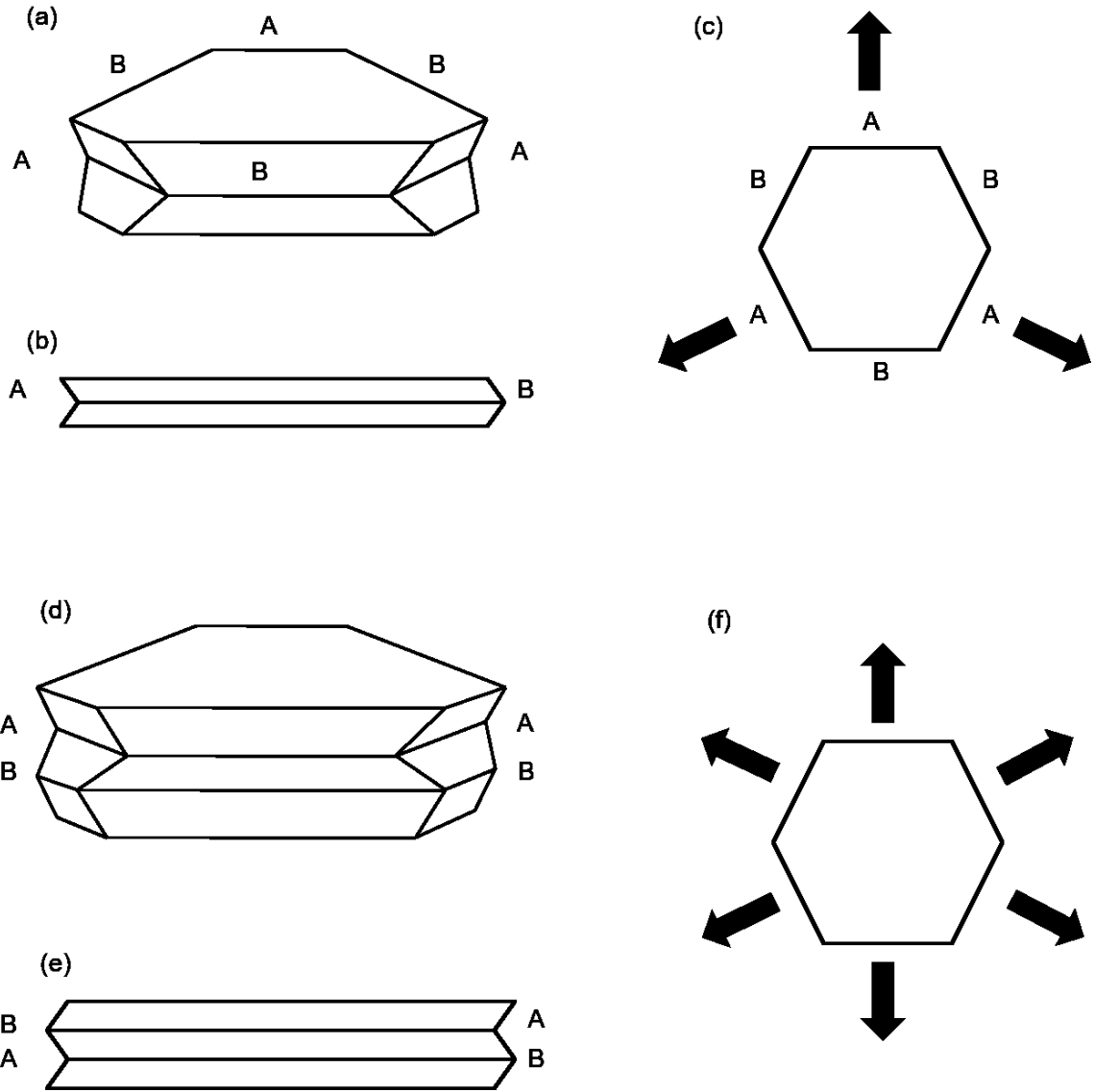


Figure 8. Growth models of triangular and hexagonal nanoplates. (a) singly-twinned hexagon; (b) cross section of the singly-twinned hexagon; (c) growth direction of the singly-twinned hexagon; (d) doubly-twinned hexagon; (e) cross section of the doubly-twinned hexagon; (f) growth direction of the doubly-twinned hexagon. Reproduced with permission from Reference 58.

4) Nanorods

Nanorods are distinguished from nanowires by their elongated cross-section.⁵⁸ One model for nanorod growth is depicted in Figure 9. Nanorods, like triangular nanoplates, origi-

nate from singly-twinned seed crystals. One-dimensional growth occurs to produce a nanorod when a crystal twins to a concave edge of the singly-twinned seed crystal, generating a new active growth site.^{44,58}

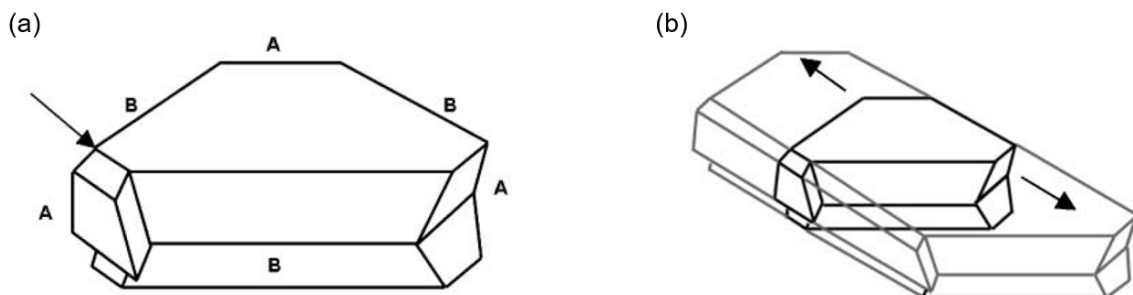


Figure 9. Growth model of nanorods. (a) singly-twinned hexagon with an attached crystal; (b) growth direction of the nanorod. Reproduced with permission from Reference 44 and 58.

Another type of nanorod has been prepared electrochemically and capped by micelles.⁶² It is abnormal for gold nanostructures to have elongated $\{110\}$ facets since these have the highest surface energy among $\{100\}$, $\{110\}$ and $\{111\}$ facets. However, the $\{110\}$ facets were thought to be stabilized by both surfactant adsorption and surface reconstruction. The latter has been seen by scanning tunneling electron microscopy (STEM), and this reconstruction increases the surface area from $\sqrt{2}a^2$ to $\sqrt{3}a^2$ while lowering the surface energy from $7.701/a^2$ to $6.928/a^2$ (Figure 10b, c).⁶² As interatomic distance increases, stronger surfactant bonds to the gold surface would be allowed to form. Once the surfactant was employed to the crystal, the $\{110\}$ facets with lower surface energy would selectively adsorb the surfactant and be capped to show a $\langle 100 \rangle$ growth direction.

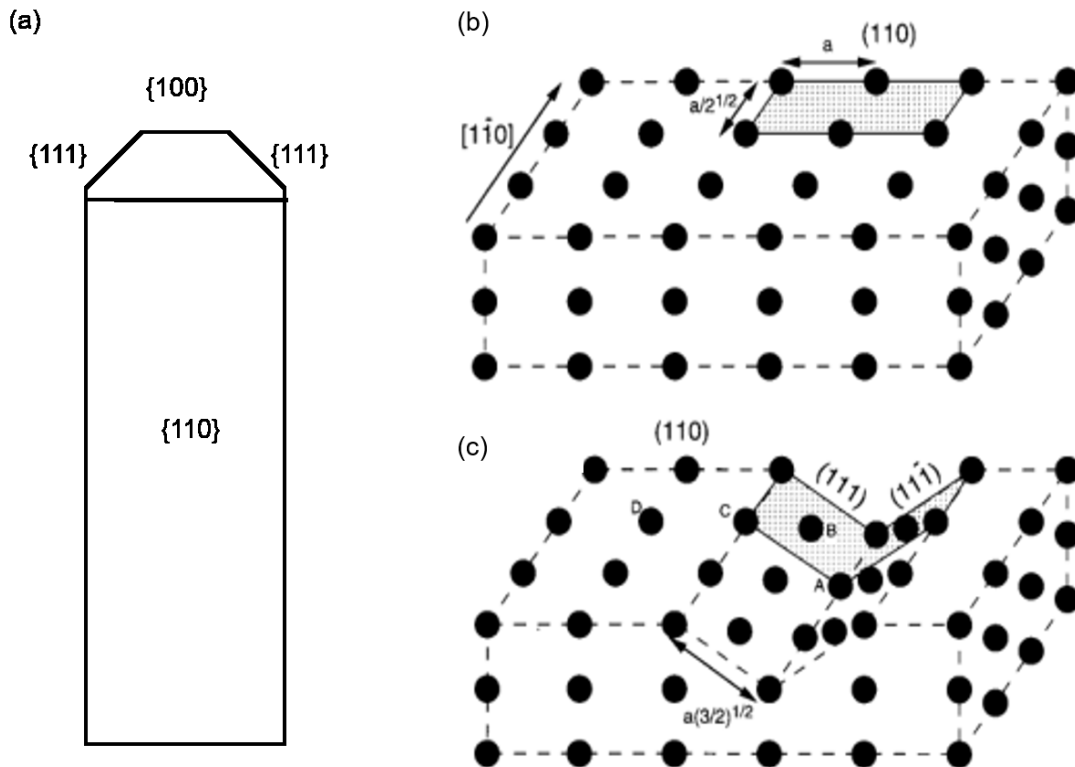


Figure 10. Growth and reconstruction models of {110} elongated nanorods. (a) {110} elongated gold nanorod; (b) atomic model of an ideal {110} facets; (c) atomic model of the reconstructed {110} facets. Reproduced with permission from Reference 62.

5) Nanostars

Gold nanostars have 20 sharp, reactive vertexes which makes them useful in catalysis because of multiple activated points.⁶³⁻⁶⁵ Nanostars form from icosahedral seed crystals (Figure 11a) through growth of each {111} facet into a sharp point. The shape transformation can be visualized as follows: each triangular {111} facet is split into six smaller triangles (Figure 11b) sharing a central point (Figure 11c).⁶⁶ The points are pulled out to make the arms of the nanostars which are hexagonal pyramid shaped (Figure 11d). The geometry of the nanostars is consistent with a model where the faces of the arms are {321}

facets. The $\{321\}$ facets are generated with the help of surfactants because of the lower h/k and l/k values.^{67,68}

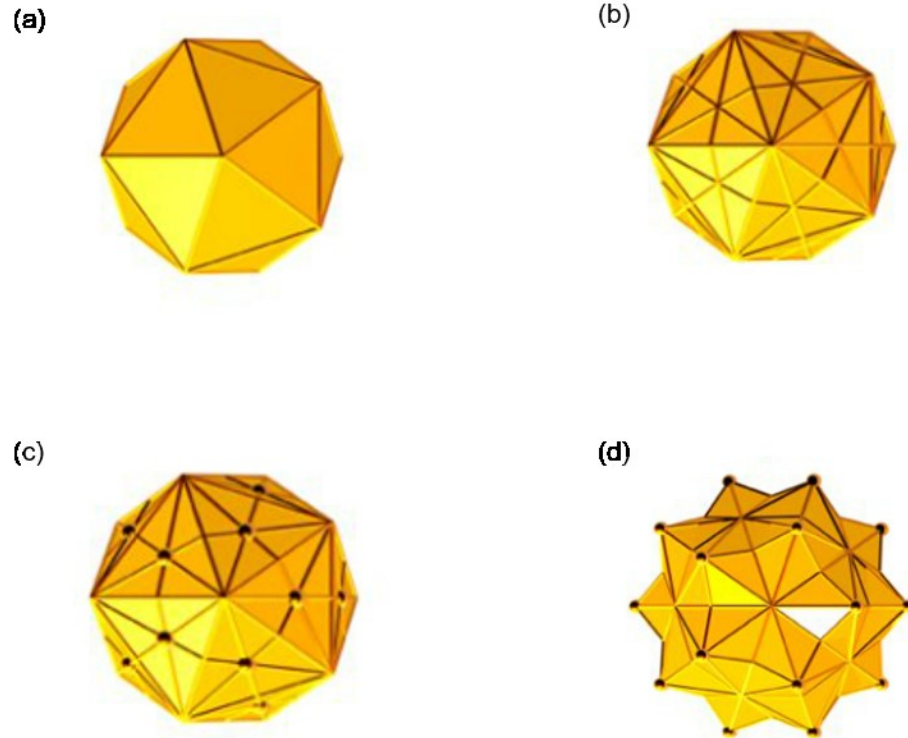


Figure 11. Growth model of nanostars. (a) icosahedron; (b) split icosahedral facets; (c) icosahedron with protuberant points; (d) nanostar. Reproduced with permission from Reference 66.

6) *Branched Particles*

Branched silver pentagonal nanowires are known, and result from the coalescence of separate nanowires.⁶⁹ The twinning occurs between two $\{111\}$ facets of the nanowires tips (Figure 12).⁴⁴ This is evidenced by the fact that the $\langle 110 \rangle$ axes of twinned wires are rotated with respect to each other by an angle of 36° . The branching is most extensive at higher temperatures, but also occurs in a lesser degree and in shorter forms at lower temperatures.

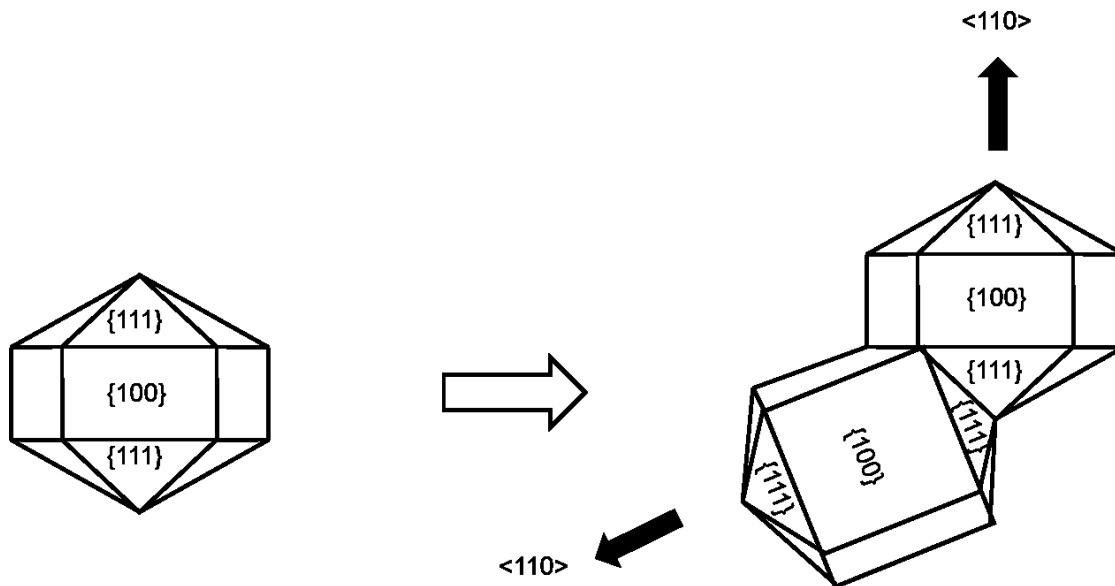


Figure 12. Growth model of branched particles. Reproduced with permission from Reference 44.

1.5 Growth Directing Surfactants

In the context of colloidal synthesis, surfactants are compounds which are adsorbed to the surface of nanostructure and lower the surface tension interfacing with the surrounding medium. Thus, surfactants serve to stabilize both colloids and nanostructures which would otherwise have high surface energies. Typically, surfactants have both hydrophilic and hydrophobic functional groups for interacting with both the solid material and the surrounding medium.⁷⁰

Not only stabilizers, surfactants are commonly employed for shape control of noble metal nanostructures through a process known as directed growth. This is possible because surfactants are adsorbed with different strength to different crystal facets, and growth is selectively slowed at the facets with a capping agent has a high steric bulk, like with hydrophobic chains. With surfactants, several particular shapes of gold had been de-

veloped like nanowires,^{71,72} nanorods,^{14,73-75} nanostars,^{66,76} and nanoplates,^{27,28,30,31,77} to name a few.

1.5.1 Selective Adsorption

Typically, selective adsorption occurs on $\{111\}$ facets since this is the closest packed and lowest surface energy crystal plane in the FCC structure.⁴⁴ This is exploited for shape control, such as in the synthesis gold nanoplates in solution using cetyltrimethylammonium bromide (CTAB)⁷⁷⁻⁸⁰ or poly (N-vinyl-2-pyrrolidone) (PVP) as surfactants.^{28,29,81-83} Both surfactants have long, hydrophobic hydrocarbon chains which effectively slow the growth on $\{111\}$ facets. The reaction kinetics were found to be first order in Au^{n+} , and the reaction rate depended on CTAB concentrations due to the selective adsorption of $\{111\}$ facets.⁸⁴

Other facets such as $\{110\}$ and $\{100\}$ can be capped to generate other morphologies.⁸⁵⁻⁸⁷ Apart from surface energy, atomic reconstruction of a crystal face also contributes to facet formation due to larger interatomic spaces allowing surfactants be more easily absorbed.^{62,66} Gold tetrahedron, a single-crystalline seed, consists of $\{111\}$ twinning planes, $\{110\}$ surfaces and stepped $\{100\}$ facets.⁸⁸ Gold nanowires as described above can be synthesized with the help of CTAB.⁸⁹ During making gold nanostars, a preferred adsorption on $\{321\}$ facets with dimethylamine (DMA) was the key to form the sharp tips of the stars, as well as using PVP as a stabilizer of the $\{111\}$ facets.⁶⁶

1.5.2 Self-Assembled Monolayers

Self-assembled monolayer (SAM) formation is a useful technique to make gold nanoparticles.⁹⁰⁻⁹² Typical SAM processes have been described often.⁹³⁻⁹⁷ Precursors are synthesized by inorganic metallic materials and surface active organic compounds. Via specific mechanisms, precursor molecules automatically assemble together to form particles in particular shapes (Figure 13).

Organic compounds with thiol groups can be used to make gold nanoplates.^{96,98} Gold (III) is reduced to gold (I) by quaternary ammonium salts (NR_4X), forming the gold precursors. Sodium borohydride (NaBH_4) then reduces gold (I) to gold (0) crystals and release ammonium ligands. Meanwhile, thiol works as a surfactant by capping the $\{111\}$ plane of the crystals (Figure 13a). Gold nanoplates with $\{111\}$ surfaces are consequently produced whose shape is influenced by the gold/thiol ratio.⁹⁸ Gold nanowires can be fabricated by using oleylamine as a reductant and surfactant.⁹⁷ With a similar process, gold (III) is partially reduced to gold (I) and make complex molecules with oleylamine. Following this, gold (0) crystals are obtained by further reduction, and the shapes of the resulting nanostructures are controlled by self-assembly of oleylamine at the elongated sections (Figure 13b).

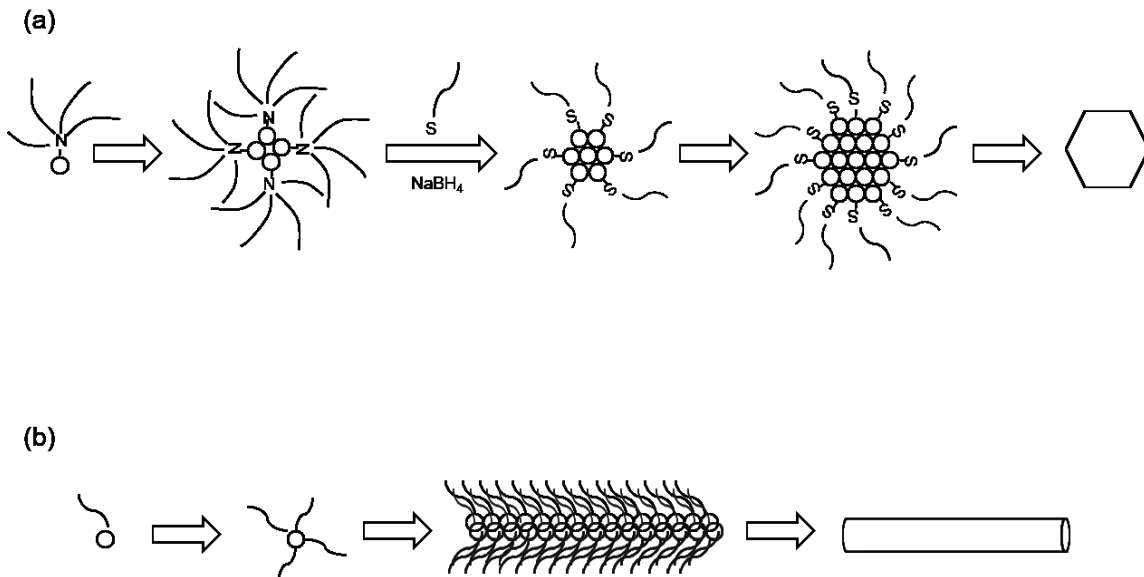


Figure 13. Schematic Diagram for the growth of shaped gold particles via SAM. (a) hexagonal nanoplates; (b) nanowires. Reproduced with permission from Reference 96 and 97.

1.5.3 Hydrophile Lipophile Balance

Given the relatively strong surface dipole of metals, compounds with stronger dipoles would be higher probable to be attracted on the surface due to stronger van der Waals interactions. The hydrophile lipophile balance (*HLB*) has been used to compare the hydrophilicity of surfactants, especially among those with different hydrophilic heteroatoms.⁹⁹ For non-ionic surfactants, the *HLB* values can be determined using Equation 1, qualitatively comparing the number of hydrophilic and hydrophobic functional groups or atoms, with an assumption that the attractive force is proportional to the mass of those hydrophilic groups:

$$HLB = \frac{\text{mass of hydrophilic atoms or groups}}{\text{molecular mass}} \times 20 \quad (1)$$

Table 1 shows *HLB* rankings for water solutions of various surfactants and the relevant applications. With low *HLB* values (e.g., 4-8), the surfactants can be used as emulsifier to suspend hydrophobic chemicals uniformly.⁹⁹ In contrast, surfactants with high *HLB* values (e.g., >16) would make hydrophobic solute resolve in polarized solvents.

Table 1. Properties and applications of surfactants with different *HLB* values.

Properties after mixing with water	<i>HLB</i> values	Potential applications
	0	
non-dispersed mixtures	2	
	4	emulsifiers
slight dispersed mixtures	6	
unstable emulsions	8	
	10	wetting agents
stable emulsions	10	
translucence	12	
	14	detergents
solution	16	
	18	solubilizers

1.6 Surfactant-Assisted CVD

There are several advantages of using CVD for preparing nanostructured gold thin film. Impurities can be minimized since no solvent is used and by-products can be designed to be volatile.¹⁰⁰ Additionally, nanostructures can be integrated directly into devices as no additional steps are required to transfer particles to a substrate, especially for water sensitive materials. Not only is this efficient, but it avoids potential alteration of morphology

which can occur during drying after wet chemistry.^{101,102} Thus, shape-controlled CVD would be a valuable technique to establish.

Compared with solution methods,³² fewer methods have been reported for shape control during CVD using a surfactant because many surfactants are non-volatile salts or polymers.¹⁰³ Volatilized elemental sulfur was employed as a surfactant to synthesize GaSb nanowires by stabilizing Sb atoms at the surface.¹⁰⁴ Smooth, {111} oriented copper films were obtained using iodine as a surfactant. In this case an *in situ* reflectivity detector was employed to precisely calibrate iodine dosing.⁶⁰ A couple of strategies have been reported for employing non-volatile surfactants in CVD. CTAB-stabilized SnS nanowires were synthesized by treating tin foil with a CTAB solution then exposing it gaseous H₂S.¹⁰⁵ Size-controlled gold nanoparticles were prepared by using tetraoctylammonium bromide (TOAB) as a surfactant through aerosol-assisted CVD (AACVD) with an arrow size distribution.¹⁰⁶

Though some progresses have been made in surfactant-assisted CVD, it is limited in terms of materials and morphologies, leaving plenty of room to explore this area of materials science. There is little literature on gold synthesis by CVD, in particular high aspect-ratio nanoplates. Some atoms, like sulfur^{95,107,108} and iodine,^{109,110} were used to passivate gold surfaces, making them potentially interesting for shape control of particles through CVD. As a volatile liquid, THT has the potential to control the shape of gold particles via CVD through its sulfur atom and the steric bulk of its hydrophobic ring. Also, the low cost of this material makes it attractive to be employed in an industrial setting. 1,3-diisopropyl-imidazol-2-ylidene gold (I) hexamethyldisilazide was shown to be an effective precursor for gold CVD.³² Since the resulting film showed initial interesting nano-

plate morphology, this precursor was the precursor of choice in this project: all gold CVD described below uses 1,3-diisopropyl-imidazol-2-ylidene gold (I) hexamethyldisilazide as precursors.

1.7 Flow Conditions

Precursor transport is heavily affected by gas velocity, which in turn may influence particle growth during CVD. Thus, the flow condition of the CVD experiment should be considered with respect to its influence on the formation of gold nanoplates. From on the ideal gas equation (Equation 2) and the average molecular mass from Equation 3.¹¹¹

$$PV = nRT \quad (2)$$

$$\bar{M} = \frac{P_1M_1 + P_2M_2}{P_1 + P_2} \quad (3)$$

Where P is the pressure of a gas, Pa; V is the volume of a gas, m³; n is the amount of substance, mol; R is the perfect gas constant, 8.314 m³·Pa·mol⁻¹·K⁻¹; T is the temperature, K; M is the molecular mass, kg·mol⁻¹.

Under high vacuum, intermolecular attractions are weaker leading to different kinetic properties of the gas.¹¹¹ Assuming ideal particles (as above), the molecular mean free path (MMFP) of the viscous gas can be estimated via Equation 4.¹¹² The mean molecular velocity (MMV) can be calculated with Equation 5 base on the Maxwell distribution.¹¹¹ Combining 3-5, Equation 6 can be used to determine the MMFP for a particular gas.

$$\lambda = \frac{\mu}{u} \cdot \frac{1}{\bar{C}} \quad (4)$$

$$\bar{C} = \sqrt{\frac{8RT}{\pi M}} \quad (5)$$

$$\lambda = \frac{1}{1.016} \cdot \frac{16}{5} \cdot \frac{\mu}{P} \cdot \sqrt{\frac{RT}{2\pi M}} \quad (6)$$

Where, λ is the MMFP of a gas, m; μ is dynamic viscosity of a gas, Pa·s; \bar{C} is the MMV, m·s⁻¹; u is a factor, $1.016 \times (5\pi/32)$; ¹¹² R is the perfect gas constant, 8.314 m³·Pa·mol⁻¹·K⁻¹; M is the molecular mass, kg·mol⁻¹; T is the temperature, K.

Knudsen numbers are typically used to describe gaseous molecular motion, showing flow conditions under high vacuum.¹¹³ The Knudsen numbers can be calculated from Equation 7.

$$Kn = \frac{\lambda}{L} \quad (7)$$

Where Kn is the Knudsen number; λ is the MMFP of a gas, m; L is the representative physical length scale, m.

When Kn is lower than 1/100, the gas would be defined as having a viscous flow because the molecular interactions are dominated by collisions between gaseous molecules (Figure 14b).¹¹³ On the contrary, a Knudsen flow would be categorized as having a Kn larger than 1/3. The MMFP is even longer than the length of the system. So instead of intermolecular collisions, gaseous molecules prefer to move "independently" performing heat transfer via collisions with the wall of a system (Figure 14c). If Kn is between 1/100 and 1/3, the gas would be in a transitional flow, mixing properties of viscous and Knudsen flow.

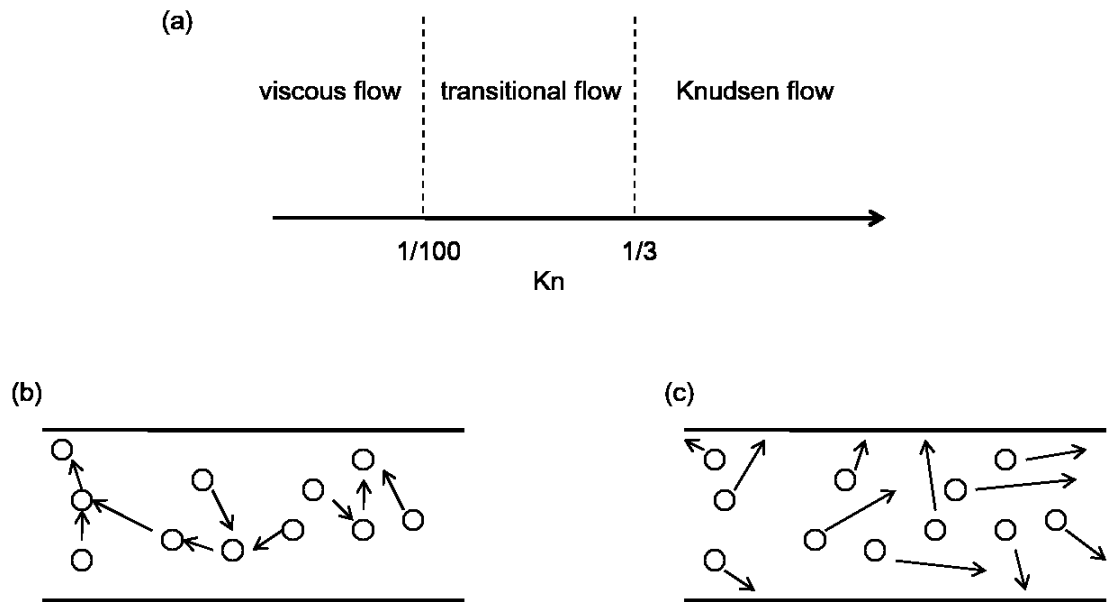


Figure 14. Knudsen numbers and flow conditions. (a) relationship between Knudsen numbers and flow types; (b) flow condition of the viscous flow; (c) flow condition of Knudsen flow.

1.8 Project Overview

The goal of this project was to develop a method for controlling the morphology of nanostructured gold films deposited by CVD. This entailed precursor synthesis, CVD apparatus construction, surfactant selection and detailed CVD studies employing the selected surfactant.

The precursor synthesis was undertaken according to a literature procedure (Figure 15).³² Detailed synthetic procedures are discussed in Chapter 6.

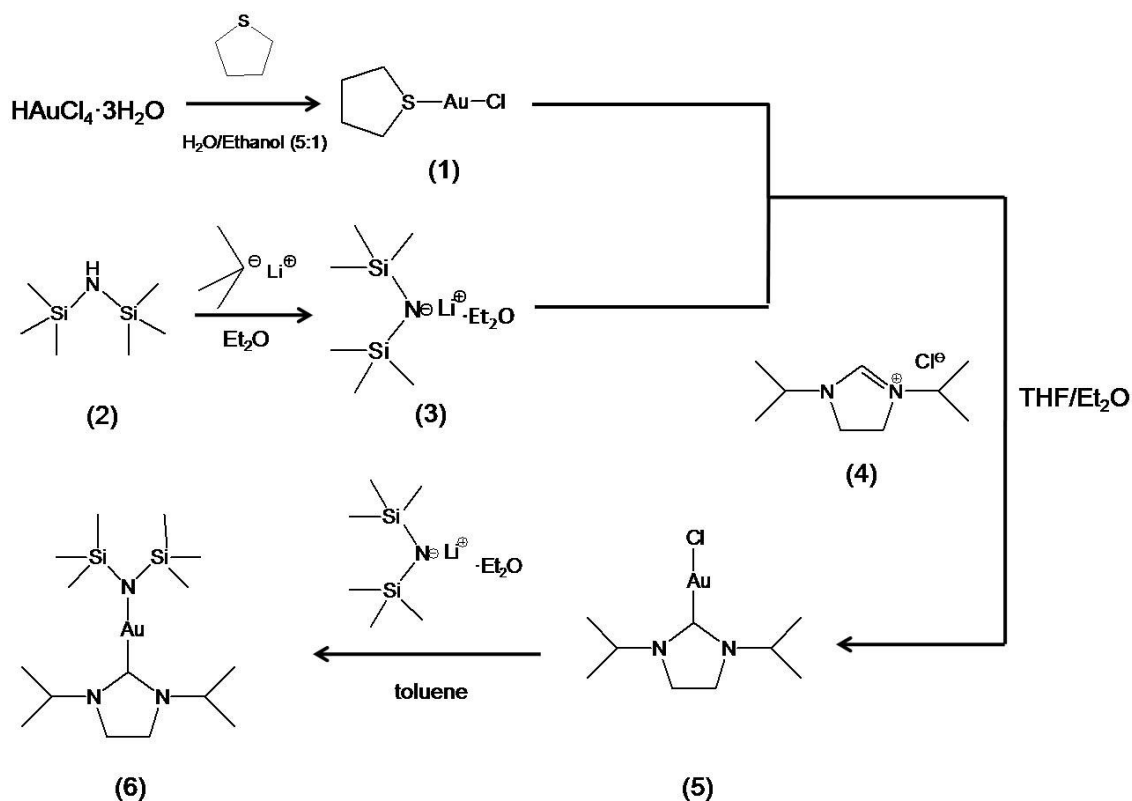


Figure 15. Schematic diagram for synthesis of the gold precursor. (1) tetrahydrothiophene gold (I) chloride; (2) hexamethyldisilazane; (3) lithium hexamethyldisilazide·diethyl ether; (4) 1,3-diisopropyl-4,5-dihydro-3H-imidazol-1-ium chloride; (5) 1,3-diisopropylimidazolidin-2-ylidene gold (I) chloride; (6) 1,3-diisopropyl-imidazol-2-ylidene gold (I) hexamethyldisilazide.

In Chapter 2, the CVD apparatus is outlined. Additionally, studies screening potential surfactants for use in CVD with the precursors (4, 6) are outlined. The candidate surfactants were tetrahydrofuran (THF), 1,3-di-t-butyl-imidazol-2-ylidene carbene (NHC) and tetrahydrothiophene (THT).

In Chapter 3, gold CVD studies using THT as the surfactant are discussed. The dependence of nanostructure shape, size, and surface morphology on the furnace temperatures and input pressure of THT are explored. The effect of changing the total system pressure is explored by using flowing nitrogen instead of THT at similar pressures. Imag-

ing characterization (SEM, TEM, and SAED) and compositional analysis (EDS and XPS) were conducted as well.

In Chapter 4, a brief summary of the results in this project is discussed, and the future work is elaborated in Chapter 5.

2 Screening Gold CVD

A new apparatus was established for the gold CVD. Using **4** only, control depositions and blank depositions were performed to investigate the effectiveness of the new constructed system. Some potential compounds then were studied to determine a useful surfactant for the further depositions. The detailed deposition of the process is discussed in Chapter 6.

2.1 System Construction

2.1.1 Separated-Feeding-Route Apparatus

Precursors and surfactants were input separately in the separate-feeding-route CVD apparatus (Figure 16). A mass flow controller (MFC, **4**, MKS P9B) was used for pressure control of the surfactant. There was a gate valve (**3**, Swagelok SS-43GS4) between the MFC and the surfactant bubbler (**2**, CCR Process Products, stainless steel, KF-25, 100 mm). A joint needle valve (**8**, Swagelok SS-1VS4-X) was positioned after the MFC, controlling the nitrogen (**1**, Praxair Instrument 4.8) for chamber filling. A control valve (**9**, Swagelok SS-43GS4) was set between it and the furnace pipe (**15**, CCR Process Products, stainless steel, CF-275, 24 inch, Φ 1.5 inch). On the other gas route, a glass precursor vial (**6**, Chemglass, CV-2100) was put inside a precursor bubbler (**5**, CCR Process Products, stainless steel, KF-25, 100 mm), using a gate valve (**7**, Swagelok SS-43GS4) to control the precursor feed. A nickel substrate boat (**10**, 12×1.0×0.38 (inch)) was positioned at the left end of the furnace pipe. With an independent temperature controller (Lindberg/Blue CC58114A Control Consoles), a heater (**11**, Lindberg/Blue HTF 55322A Hinged Tube Furnace) was used to maintain the furnace pipe at desired temperatures. A cross pipe

(CCR Process Products, stainless steel, KF-25 Cross) was installed to the right of the furnace pipe linking with a pressure gauge (12, Agilent/Varian 0531 Thermocouple Gauge Tube). A cold trap (14, stainless steel, KF-25) filled with liquid nitrogen was used to trap the by-products and excess surfactant during depositions. Vacuum was achieved with a roughing pump (13, General Electric SKCR47UG26BT) located on the right end of the CVD apparatus. Made of stainless steel, all tubes (Φ 0.25 inch) and pipes (KF-25) in the feeding system were wrapped by foil and heating tape to stabilize the input temperatures of the gaseous chemical components. The furnace pipe was sealed by nipples with copper O-rings (CCR Process Products, CF-35), while other units were sealed with stainless steel centering rings with rubber O-rings (CCR Process Products, KF-25), as well as two ferrule tube fitting (Swagelok, 0.25 inch).

Depositions were performed under a modified process based on the literature.³² However, no metallic gold deposition occurred using this apparatus. Instead, reflective gold metal collected at the inlet of the furnace pipe, suggesting that the precursors decomposed. The system was not likely suitable because the diffusion path was too long for precursor transport, leading to precursor decomposition prior to the substrates. Thus, the system had to be modified by shortening the route between the precursor bubbler and the substrates.

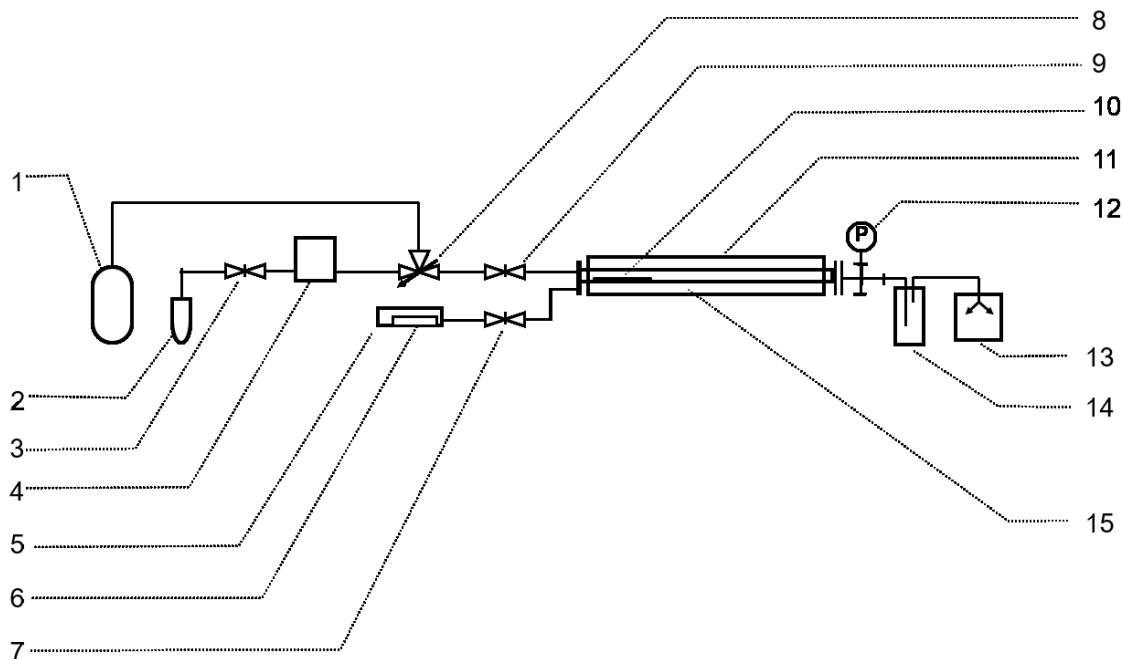


Figure 16. Schematic diagram for the separated-feeding-route CVD apparatus. (1) nitrogen tank; (2) surfactant bubbler; (3) gate valve; (4) MFC; (5) precursor bubbler; (6) precursor vial; (7) gate valve; (8) joint needle valve; (9) control valve; (10) substrates; (11) furnace heater; (12) pressure gauge; (13) roughing pump; (14) cold trap; (15) furnace pipe.

2.1.2 Combined-Feeding-Route Apparatus

Instead of a separate-route system, a single-input apparatus was designed for the gold depositions (Figure 17). A glass precursor vial (2, Chemglass, CV-2100) was placed in a precursor bubbler (1, CCR Process Products, stainless steel, KF-25, 100 mm) which was attached to a T-pipe (CCR Process Products, stainless steel, KF-25 Tee) connected in parallel to a furnace pipe (8, CCR Process Products, stainless steel, CF-275, 24 inch, Φ 1.5 inch). To control the pressure of surfactant, a gate valve (3, Swagelok SS-43GS4) and a needle valve (4, Swagelok, SS-4L-MH) were employed respectively between the T-pipe and surfactant bubbler (5, CCR Process Products, stainless steel, KF-25, 100 mm)

located on the vertical arm of the T-pipe. A cross pipe (CCR Process Products, stainless steel, KF-25 Cross) was installed on the right of the furnace pipe, linking to a pressure gauge (9, Agilent/Varian 0531 Thermocouple Gauge Tube). Positioned at the right end, a nitrogen tank (13, Praxair Instrument 4.8) with a control gate valve (12, Swagelok SS-43GS4) was used for back-filling. As discussed in Section 2.2.1, copper O-rings and KF-25 centering rings were used to seal the apparatus.

Temperature uniformity is an important factor to guarantee the reliability of depositions. As a tube furnace, coiled heaters provided the uniformity and the heating efficiency within the equipment. Moreover, corundum supports were used to hang the furnace pipe, insulating potential heat transfer between the furnace and surroundings. Also, thermal leaks between the supports and the furnace pipe were filled with glass wool (Fisher Scientific) to further maintain the heat uniformity in the furnace. The thermocouple for temperature monitoring was located in the middle of the furnace, similar to the locations of the deposited films. So the temperatures used to control the furnace can be reasonably affirmed as deposition temperatures.

For the comparison experiments, substituting surfactant over-pressure with nitrogen, another nitrogen tank (5, Praxair Instrument 4.8) with a control gate valve (Swagelok, SS-1VS4) was used to replace the surfactant bubbler (Figure 18).

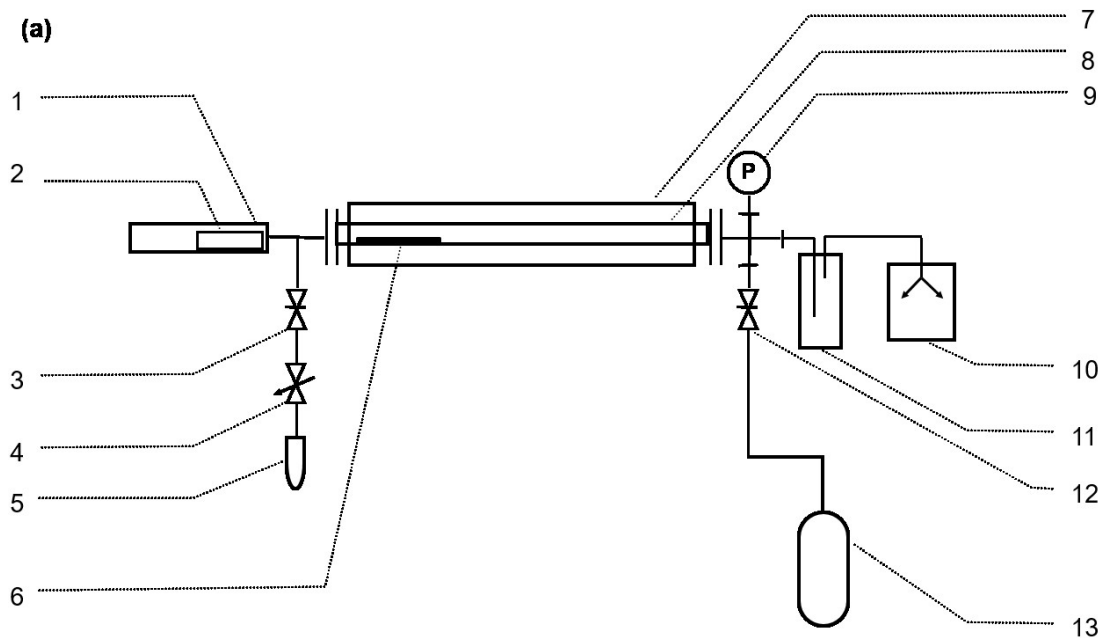


Figure 17. Diagrams for the combined-feeding-route CVD apparatus. (a) schematic diagram of the apparatus; (b) photo of the feeding system; (c) photo of the trapping system. (1) precursor bubbler; (2) precursor vial; (3) gate valve; (4) needle valve; (5) surfactant bubbler; (6) substrates; (7) furnace heater; (8) furnace pipe; (9) pressure gauge; (10) vacuum pump; (11) cold trap; (12) gate valve; (13) nitrogen tank.

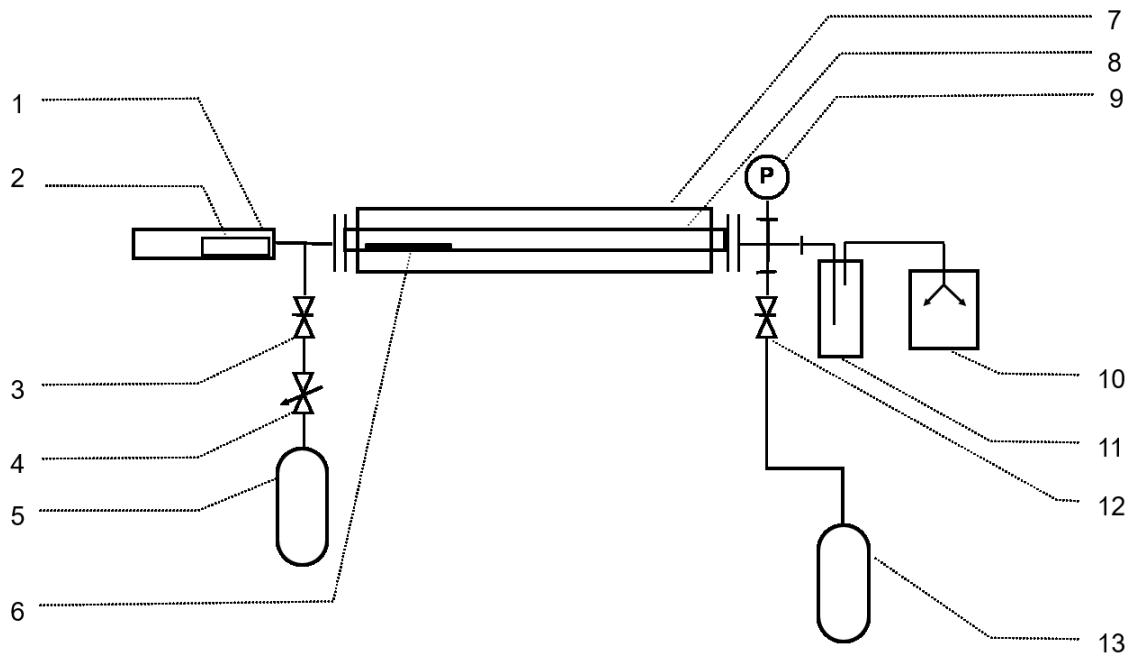


Figure 18. Schematic diagram for the nitrogen flow CVD apparatus. (1) precursor bubbler; (2) precursor vial; (3) gate valve; (4) needle valve; (5) nitrogen tank; (6) substrates; (7) furnace heater; (8) furnace pipe; (9) pressure gauge; (10) vacuum pump; (11) cold trap; (12) gate valve; (13) nitrogen tank.

Gold depositions were found at specific locations on the substrate boat, which was influenced by temperatures (Figure 19). At 430°C, gold films were located at 13-20 cm from the left of the boat (1). The films moved a bit further to 15-23 cm at 370°C because of slower decomposition at this lower temperature (2). At 310°C, further rightward film depositions located at 23-30 cm could be observed (3). Additional gas flow also affected the film position. With 45 mtorr of nitrogen at 430°C, the precursor transport was assisted and spread further, resulting to further depositions at 23-30 cm (4).

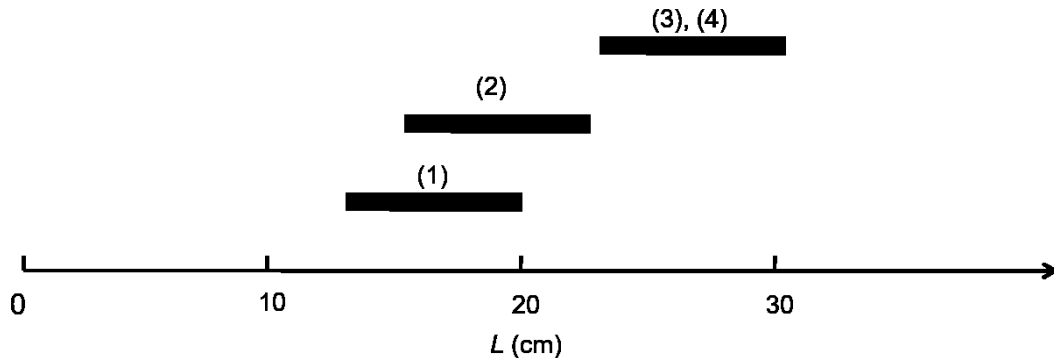


Figure 19. Locations of the gold depositions. (1) 13-20 cm: $T_d = 430^\circ\text{C}$; (2) 15-23 cm: $T_d = 370^\circ\text{C}$; (3) 23-30 cm: $T_d = 310^\circ\text{C}$; (4) 23-30 cm: $T_d = 370^\circ\text{C}$, $P_N = 45$ mtorr.

2.2 Test Depositions

Using 4 only, two different depositions were employed to check validity of the constructed CVD apparatus. During the control runs, only the precursor input route was used to repeat the reported depositions.³² Meanwhile, the "blank" runs used both precursor and surfactant input route to fabricate gold films, with nitrogen flowing through surfactant route.

2.2.1 Control Run

At 430°C , a large number of nanoparticles with irregular sizes were found (Figure 20a). Shapes were varied: plates, belts and ribbons, showing some shape control of the depositions (Figure 20b). The nanoparticle sizes were widely distributed, ranging from 200 nm to $4\ \mu\text{m}$ (Figure 20b, d). The nanofeature's surfaces were rough with obvious secondary nucleation (Figure 20c). Quantities of small nanoparticles resulting from different kinds of seeds were apparent on the substrates (Figure 20d). These depositions resulted in a denser collection of nanoparticles in larger sizes compared with previous work under

similar conditions (Figure 20e).³⁹ The main reason for this is that the temperature was more stable and better controlled in the new apparatus. With less fluctuation of temperatures, the particle growth proceeded more regularly.

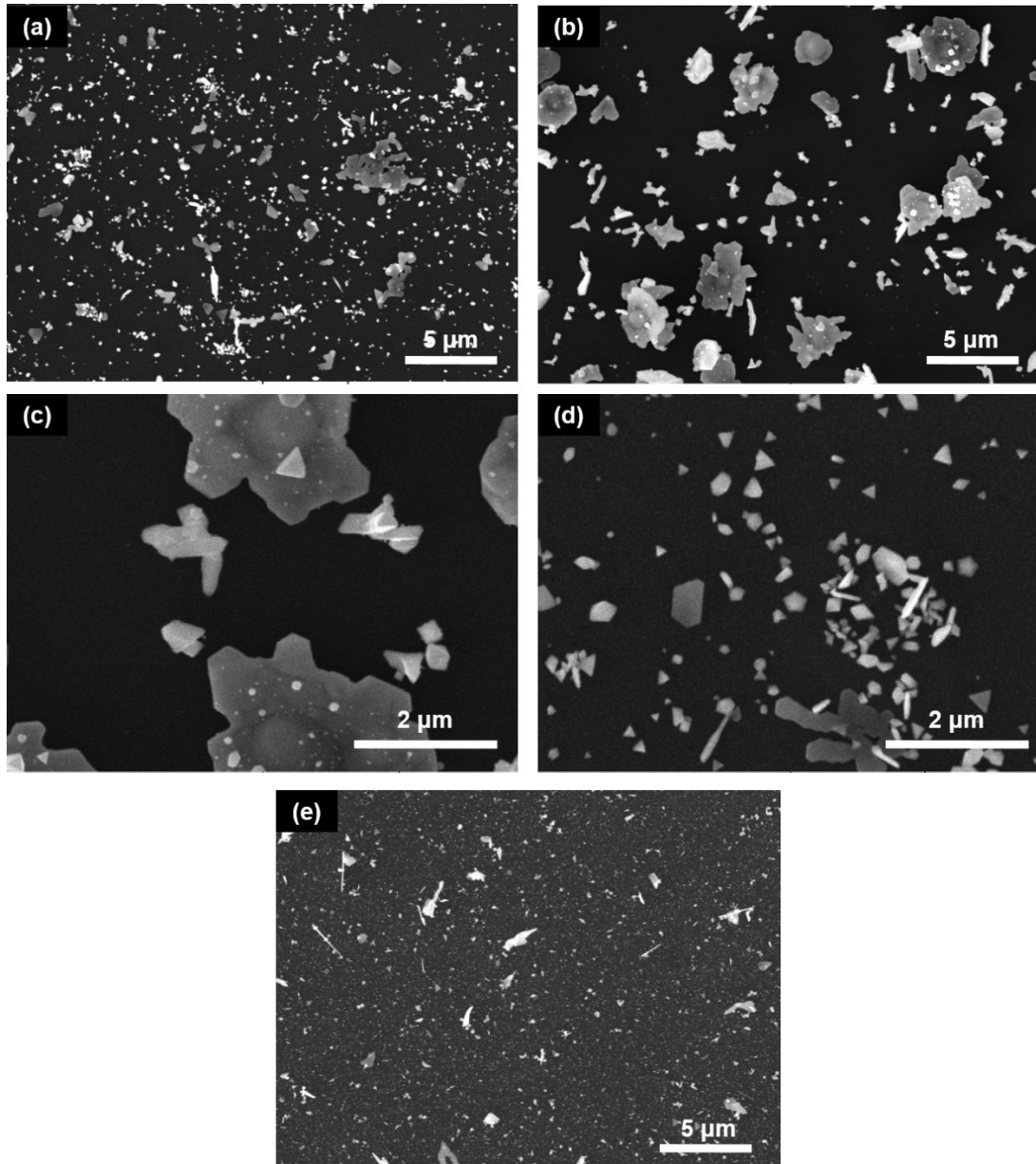


Figure 20. SEM images of gold particles deposited at $T_d = 430^\circ\text{C}$. (a-d) control depositions; (e) SEM image in Reference 39.

2.2.2 Blank Run

On the whole, nanoparticles produced from the blank runs were similar to the control runs. At 430°C, the surfactant feeding route was opened to emulate conditions when surfactant was used. Compared with the control run (Figure 21a), the blank depositions showed small nanoparticles in similar densities (Figure 21b). Sizes looked larger as well as more highly regular. However, shapes were not uniform, again demonstrating weak shape control during the depositions. Complete nanoplates were not formed, leaving irregular gaps at the edges.

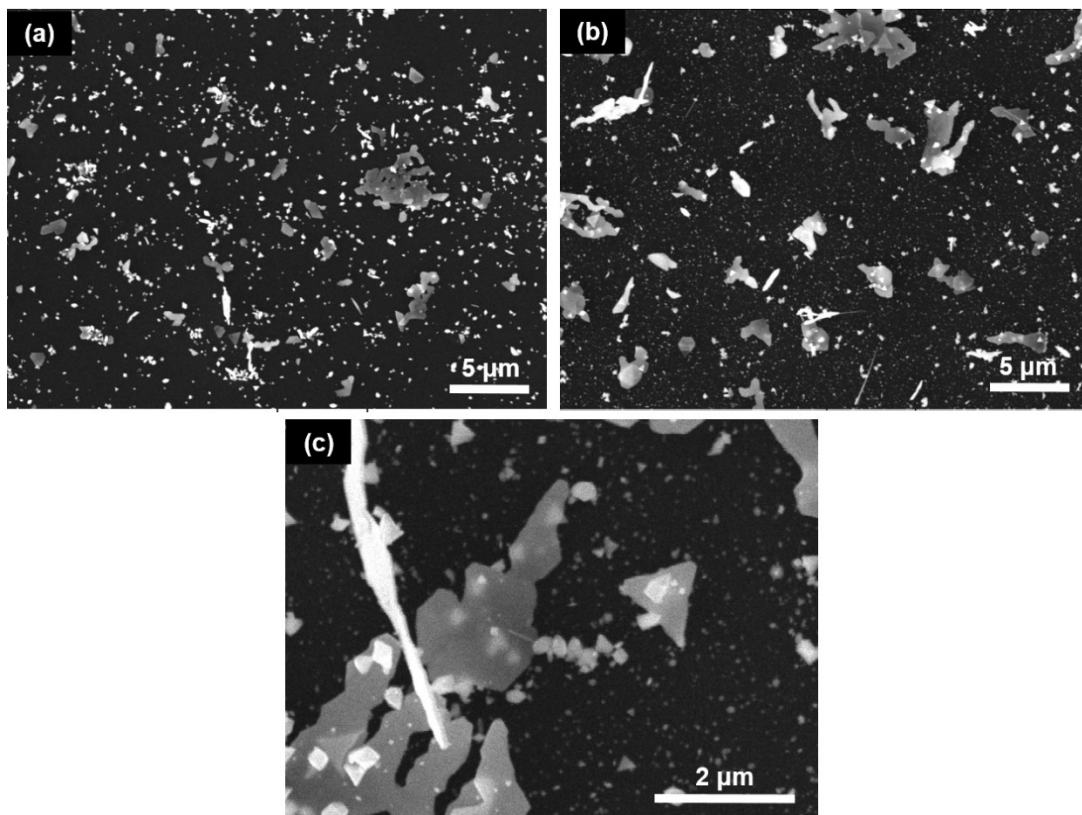


Figure 21. SEM images of gold particles deposited at $T_a = 430^\circ\text{C}$. (a) control depositions; (b) blank depositions; (c) detailed image of the blank depositions.

2.3 Surfactant Selection

In this section, several surface active chemicals were assessed for shape control during the gold CVD, including tetrahydrofuran (THF), 1,3-di-*t*-butyl-imidazol-2-ylidene carbene (NHC) and tetrahydrothiophene (THT). THF is a common solvent with low toxicity and straight-forward handling. The oxygen has the potential to interact with gold as the surface moiety. THT, the odorant used in the natural gas industry, is cheap and bears sulfur that is able to form a strong bond with gold. With a similar structure to the ligands of precursor **4**, the NHC may be useful for shape control of gold since the precursors demonstrated some shape control during the reported initial deposition of gold particles.³²

2.3.1 Tetrahydrofuran

The experiments were performed at 370°C, with 35 mtorr of THF. There was no deposition on the substrates under these experimental conditions. The THF pressures were measured every 5 minutes. The pressure dropped quickly when the deposition started (Figure 22), reaching equilibrium at 5 mtorr after 15 minutes (1). In contrast, the THF flow was stable for two hours at room temperature, which was a typical time for the deposition experiments (2).

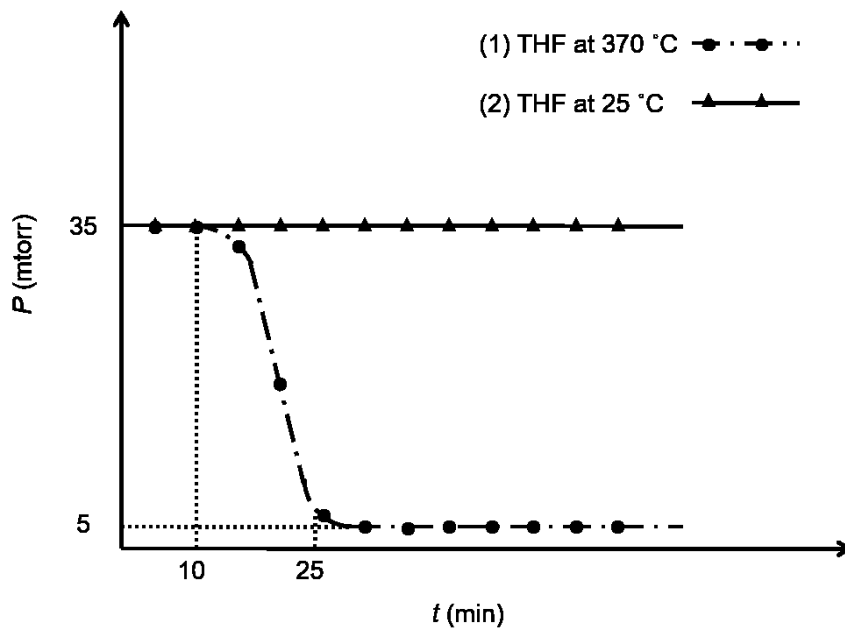


Figure 22. THF pressure-time relation curves. (1) $T = 370^{\circ}\text{C}$; (2) $T = 25^{\circ}\text{C}$.

THF is a reactive chemical leading to a network of free radical reactions (Figure 23).¹¹⁴ When exposed to light or heat, THF reacts to form 2-tetrahydrofuryl or 3-tetrahydrofuryl radical depending on temperatures. However, the former is favored because of the H atom adjacent to the oxygen center, making it more easily be abstracted. The residual oxygen in the apparatus could be consumed to form hydroperoxytetrahydrofuryl radicals via different mechanisms. These radicals may react with **4** before it arrives at the surface. So there was no deposition due to insufficient precursor supply. The pressure in the system drops quickly since those radicals may also react with the ligands released from the precursor, probably adsorbed to the metallic substrate boat and reactor walls during the CVD. Therefore, THF is not suitable to use as a surfactant for the gold CVD and other surfactant candidates have to be evaluated.

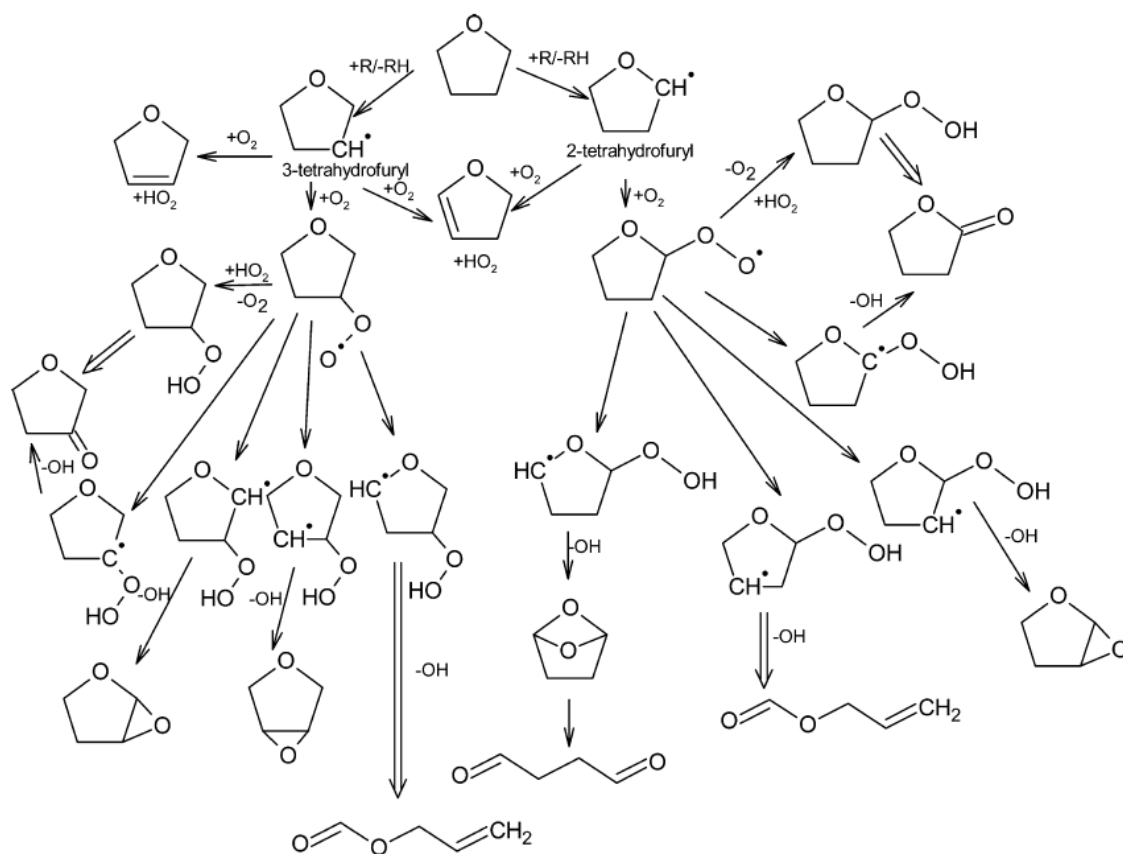


Figure 23. Schematic diagram for reaction network of THF via H-abstraction. Double arrows represent multi-step reactions. Reproduced with permission of Reference 114.

2.3.2 1,3-Di-*t*-butyl-Imidazol-2-Ylidene Carbene

The NHC-assisted gold CVD were undertaken at 430°C with 0 mtorr, 5 mtorr, 10 mtorr and 15 mtorr of NHC (Figure 24) respectively. Without NHC, dense misshapen plates were found with a lot small nanoparticles (Figure 25a, b). The particles were in highly irregular morphology with obvious secondary nucleation. Small nanoplates in truncated triangles appeared with 5 mtorr of NHC. However, small nanoparticles dominated the deposition which suggested weaker shape control than the blank run using **4** only (Figure 25c, d). At 10 mtorr, NHC helped to generate nano-ribbons which were larger than the

particles found with 5 mtorr of NHC, along with a small number of hexagons. As well, denser and larger small nanoparticles were found compared with those deposited with 5 mtorr of NHC (Figure 25e, f). With 15 mtorr of NHC, no particles in identifiable shapes were attained showing weak shape control during the depositions (Figure 25g, h).

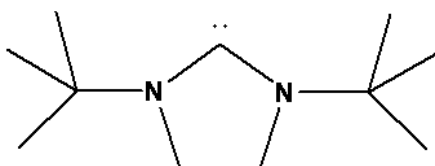


Figure 24. Diagram of 1,3-di-*t*-butyl-imidazol-2-ylidene carbene (NHC).

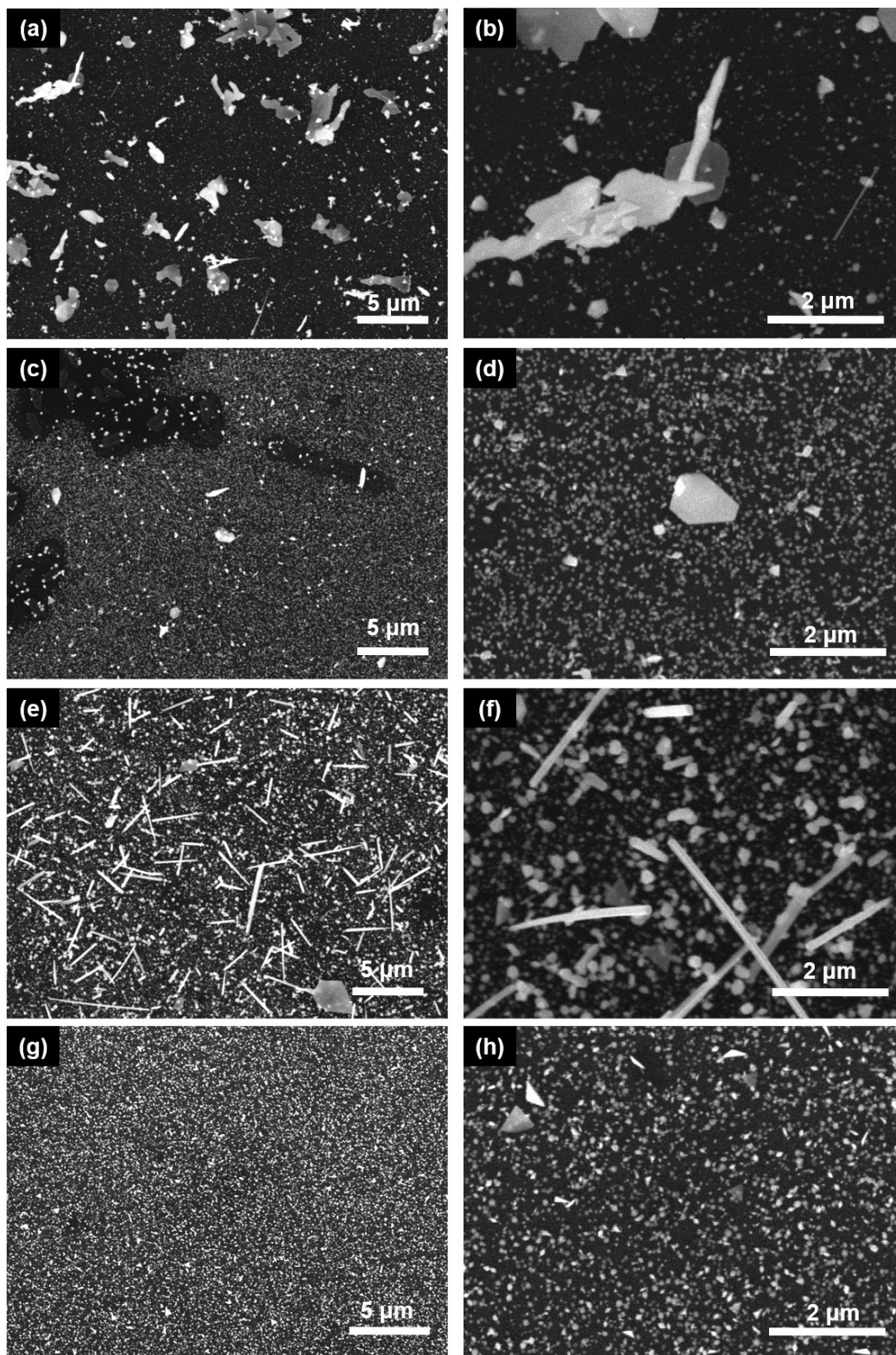


Figure 25. SEM images of gold particles deposited at $T_d = 430^\circ\text{C}$ with NHC. (a, b) $P_{\text{NHC}} = 0$ mtorr; (c, d) $P_{\text{NHC}} = 5$ mtorr; (e, f) $P_{\text{NHC}} = 10$ mtorr; (g, h) $P_{\text{NHC}} = 15$ mtorr.

A supposed model of the NHC-assisted gold CVD process is shown below (Figure 26a).^{32,35} As a strong electron donor, the NHC reacted with the precursors to form new compounds by replacing the N-heterocyclic ligands (Figure 26b). Shape control is weaker using the new compounds (2) because of weaker interactions with gold (discussed in section 3.2). Compared with the 4 (1), the new compounds allow stronger desorption, along with possibly weaker adsorptions. So there is no enhanced shape control during the depositions with 5 mtorr of NHC. With 10 mtorr of NHC, the shape control is strengthened, generating ribbons instead of small nanoparticles. The higher concentration of NHC allow higher absorption rates on specific facets (likely elongated {111} for ribbons) to lower the surface energy. With 15 mtorr of NHC, the excessive NHC caps all the surfaces on the particles without selectivity. Thus, small nanoparticles again dominate the morphology without observable shapes.

In summary, the NHC emerges as exhibiting weak shape control on nanoparticles because of its weak surface activity. A different option is needed to perform shape control via the gold CVD.

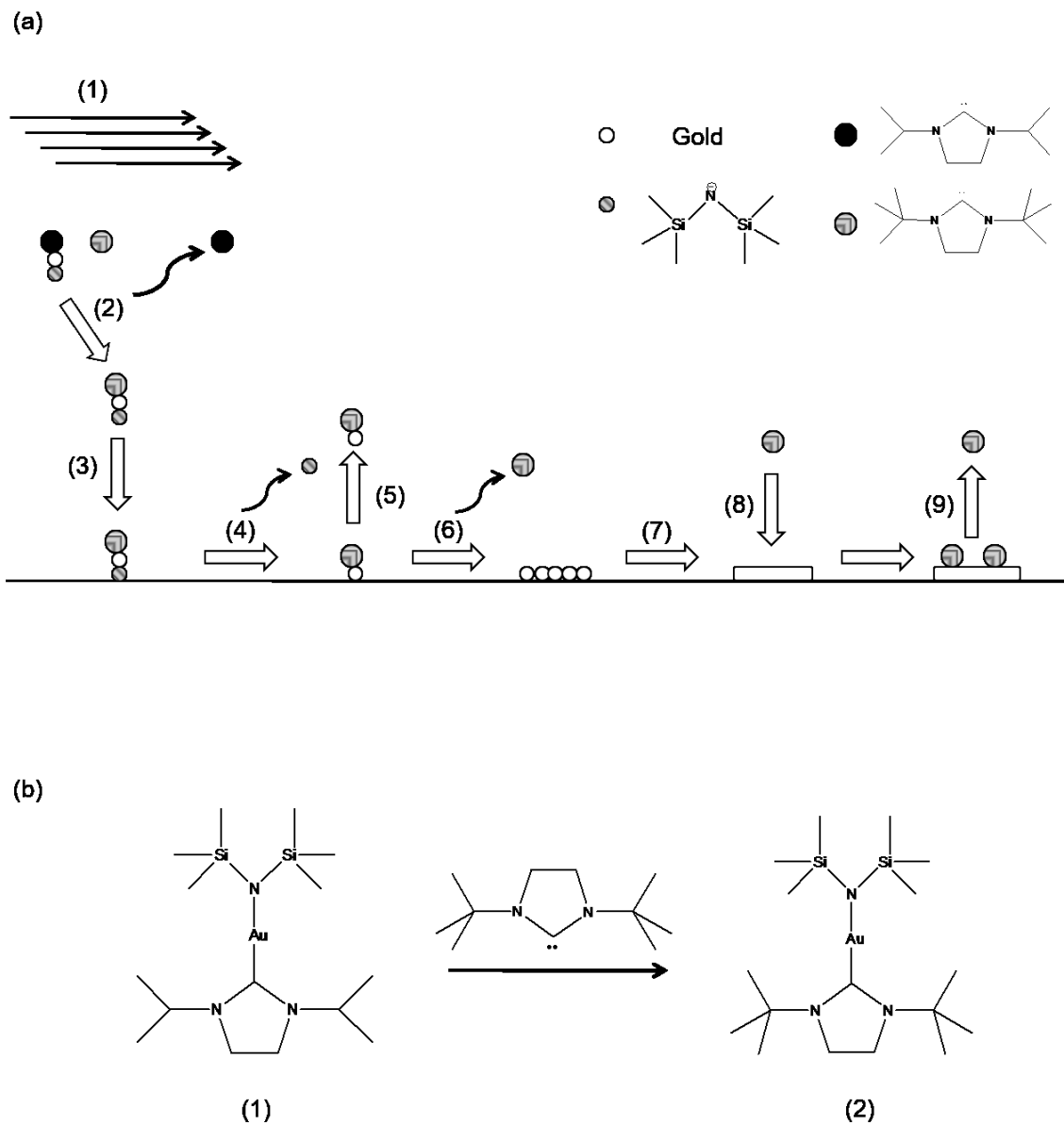


Figure 26. Schematic diagram for NHC-assisted gold CVD. (a) suggested process: (1) main gas flow, (2) NHC substitution reaction, (3) adsorption of the substituted precursor, (4) surface diffusion; (5) precursor desorption, (6) surface reaction, (7) continuous film formation, (8) shape control adsorption of NHC, (9) desorption of the NHC; (b) suggested reaction between the NHC and 4.

2.3.3 Tetrahydrothiophene

These depositions were performed at 430°C with THT at 5 mtorr, 10 mtorr and 15 mtorr respectively. These depositions resulted in a series of uniform gold films.

The morphologies deposited with 5 mtorr of THT were small triangular nanoparticles (Figure 27c, d), compared with the blank depositions with the **4** only (Figure 27a, b). The particles were also bigger but not regular, still demonstrating a weak shape control. Larger flat surfaces began to form, although secondary nucleation is still obvious, as are the poorly formed edges. With 10 mtorr of THT, the secondary nucleation was suppressed, more often showing smooth, planar surfaces (Figure 27e, f). The deposited shapes were more regular with smoother edges than the particles deposited with 5 mtorr of THT. Additionally, the particles (e.g., 3 μm) were with narrower size distribution. With 15 mtorr of THT, isolated hexagonal nanoplates appeared with significantly less small nanoparticles, which were entirely different from the deposition experiments with the **4** only (Figure 27g, h). Secondary nucleation was eliminated forming a smooth surface. Shapes were highly regular in hexagons with smooth edges which suggested excellent shape control by THT. The nanoplates were enlarged significantly (e.g., 5 μm), while the small nanoparticles decreased in size. In addition, some gold small particles were located beneath the gold nanoplates. This was thought to be generated during the initial input of **4** evaporating below 70°C before THT was added to the apparatus.

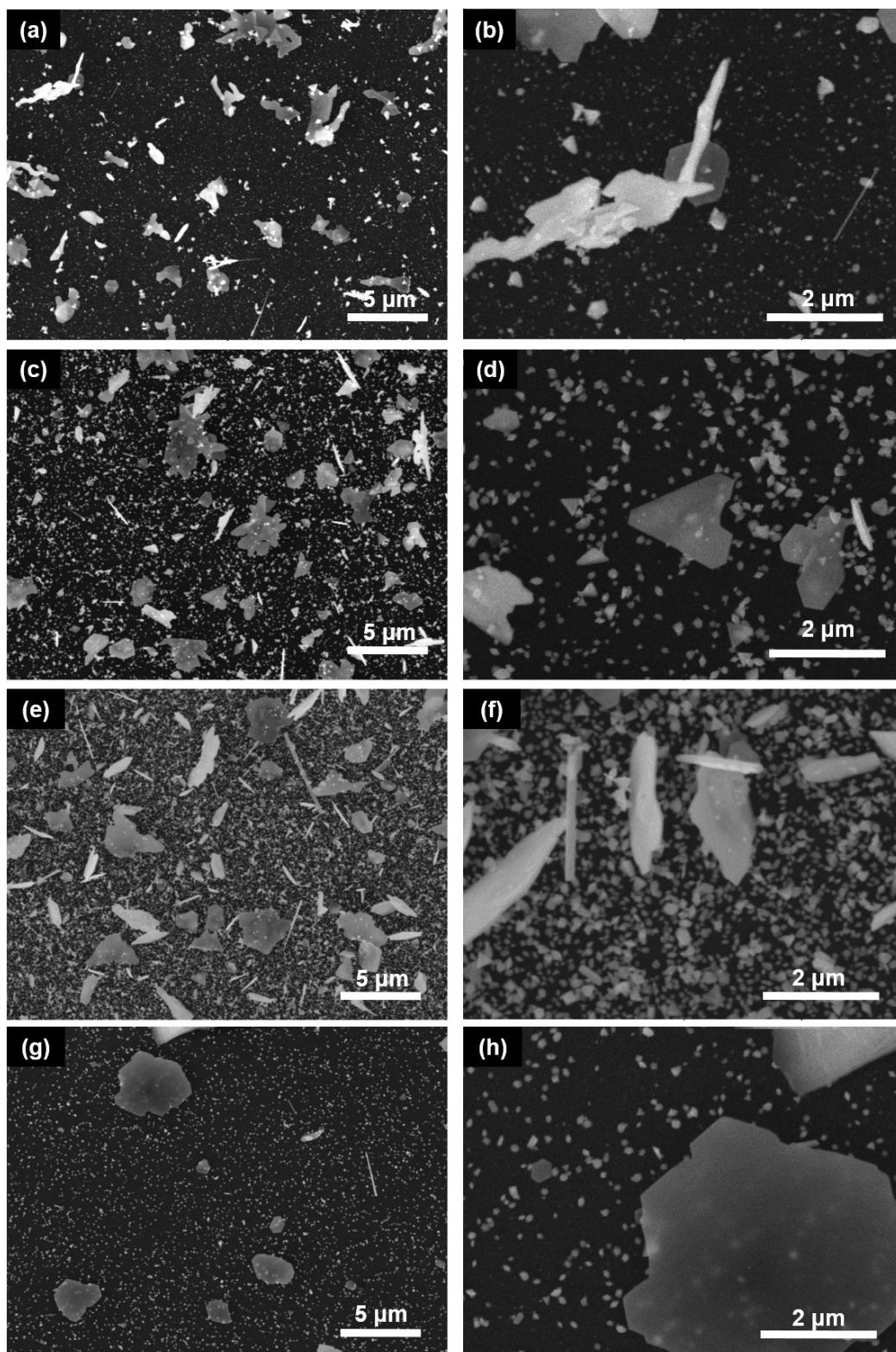


Figure 27. SEM images of gold particles deposited at $T_d = 430^\circ\text{C}$ with THT. (a, b) $P_{\text{THT}} = 0$ mtorr; (c, d) $P_{\text{THT}} = 5$ mtorr; (e, f) $P_{\text{THT}} = 10$ mtorr; (g, h) $P_{\text{THT}} = 15$ mtorr.

2.4 Summary

In this chapter, a combined-feeding-route CVD apparatus was established to perform gold CVD. Control depositions and blank depositions were undertaken by using **4** only to ensure reproducibility of the depositions. A series of compounds was investigated to seek a suitable surfactant for controlled morphology gold nanoparticle CVD. Due to thermal reactivity, THF was oxidized to generate free radicals which apparently reacted with the gold precursors. Pressure of THF dropped rapidly during the depositions and no gold films were found because of the limited gold precursor supply. NHC was evidenced to show some shape control on particles, but the shapes were irregular. At 430°C, hexagonal nanoplates of a large size (e.g., 5 μm) were identified with 15 mtorr of THT. Obvious shape control was observed by using THT making this the best available surfactant for controlled morphology gold CVD.

3 THT-Assisted Gold CVD

A detailed research on gold nanoplates was performed using gold CVD and THT as a surfactant. The detailed deposition process is discussed in Chapter 6. The morphology was characterized by SEM and TEM, as well as SAED for crystalline structures. EDS and XPS were used to investigate the elemental content. Growth models are proposed herein to explain the mechanism of shape control on gold nanoplates by THT.

3.1 Structural Investigation

3.1.1 Morphology

At 370°C, many small nanoplates were observed along with small nanoparticles (Figure 28a). The orientation of the poorly formed flakes was disorganized and there was significant secondary nucleation on the gold features. The shapes and sizes were highly irregular showing weak shape control, with a mixture of triangles, ribbons and hexagons (Figure 28b). With 45 mtorr of THT, the nanoplates were obviously larger in somewhat irregular shapes, presenting obviously smooth edges (Figure 28c). Importantly, the surface of these features was smooth showing that no secondary nucleation occurred (Figure 28d). Edges of the gold nanoplates became smoother with less acute angles. Additionally, the small nanoparticles became less dense and smaller than in the depositions using **4** only.

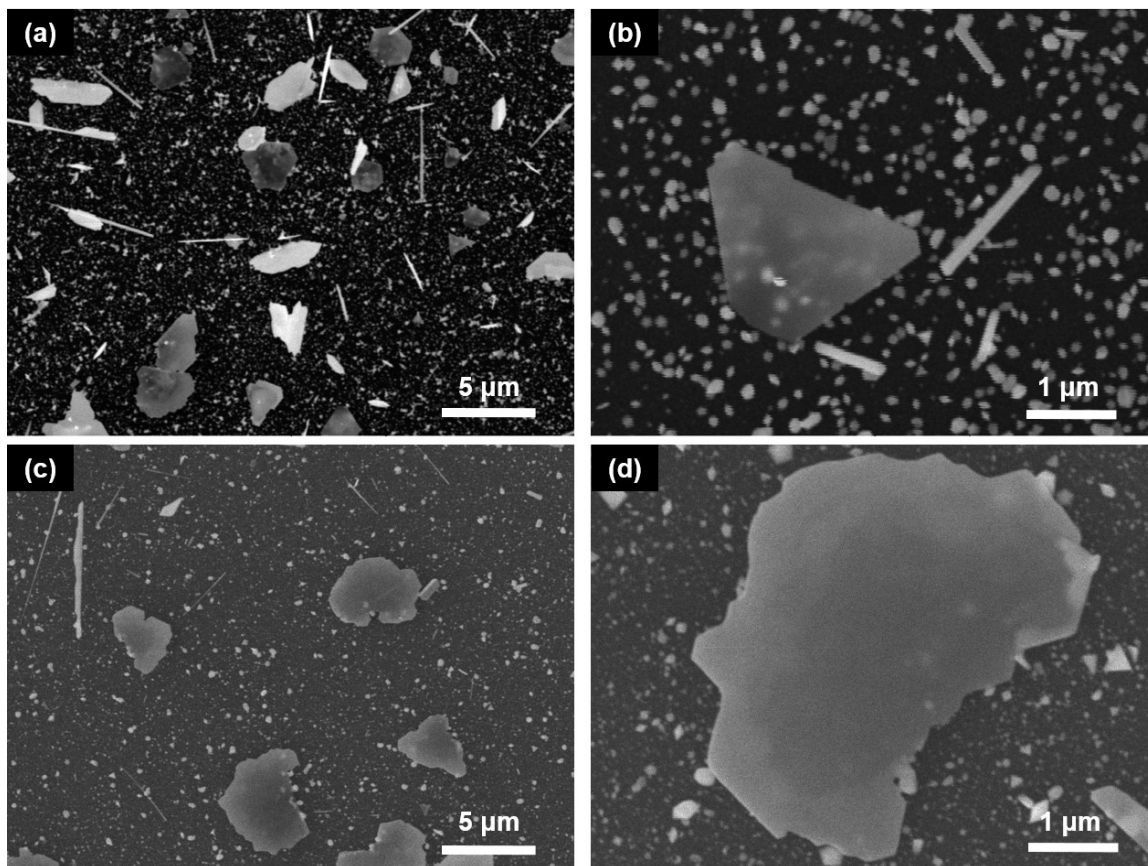


Figure 28. SEM images of gold particles deposited at $T_d = 370^\circ\text{C}$ with THT. (a, b) $P_{\text{THT}} = 0$ mtorr; (c, d) $P_{\text{THT}} = 45$ mtorr.

SEM was employed for the initial study on morphology of the deposited nanoplates. Further higher-resolution microscopy should be considered to further confirm the actual surface conditions of the nanoplates. Atomic force microscopy (AFM) or scanning tunneling microscopy (STM) might be used to accurately attain morphologic information on the plain of those nanoplates because of the detection for interaction changes between the probe and sample surface.^{115,116}

3.1.2 Elemental Analysis

EDS spectra were collected to find out the actual content of the nanoplates. The central part of a nanoplate was chosen to perform the EDS analysis (Figure 29a) and the elemental analysis in wt.% and at.% (Figure 29b).

Only gold and silicon signals were identified in the EDS. The nanoplates showed no additional signals within the detection limit (> 1 at.%). Notably there was no signal from the sulfur from THT. Due to the extremely thin nanoplates, the electron beam was able to reach the substrate, which is the source of the silicon signal.

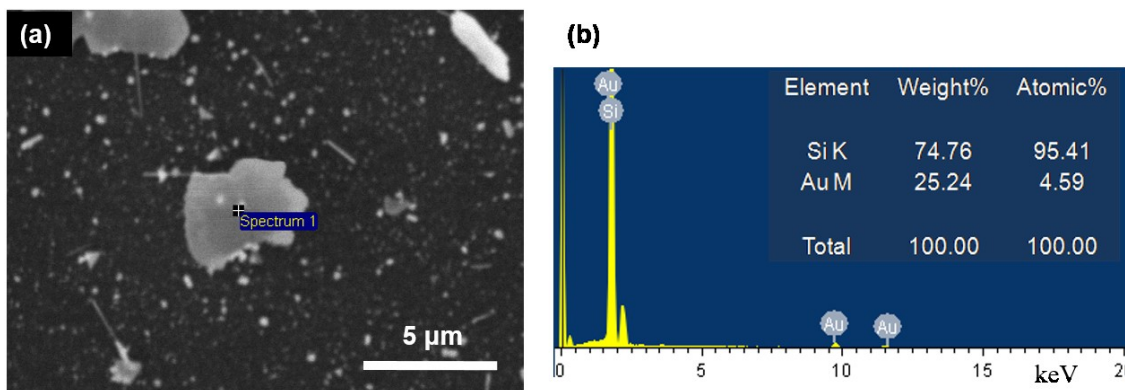


Figure 29. EDS spectrum of the gold nanoplate deposited at $T_d = 370^\circ\text{C}$, $P_{\text{THT}} = 45$ mtorr. (a) location of the spectrum; (b) elementary analysis of the gold nanoplate.

Therefore, the nanoplates were taken to be gold metal without significant impurity. But the EDS technique is not surface sensitive since electrons from the beam can penetrate entirely through the features. Thus, a more effective and specific technology has to be utilized for surface content detection (discussed in section 3.2).

3.1.3 Crystalline Structural Analysis

1) Crystalline State

Crystalline information of the gold nanoplates was needed to find out the facet type of the facial plane. Consequently, TEM imaging along with SAED was used to characterize the crystalline structure of the prepared gold nanoplates (Figure 30).

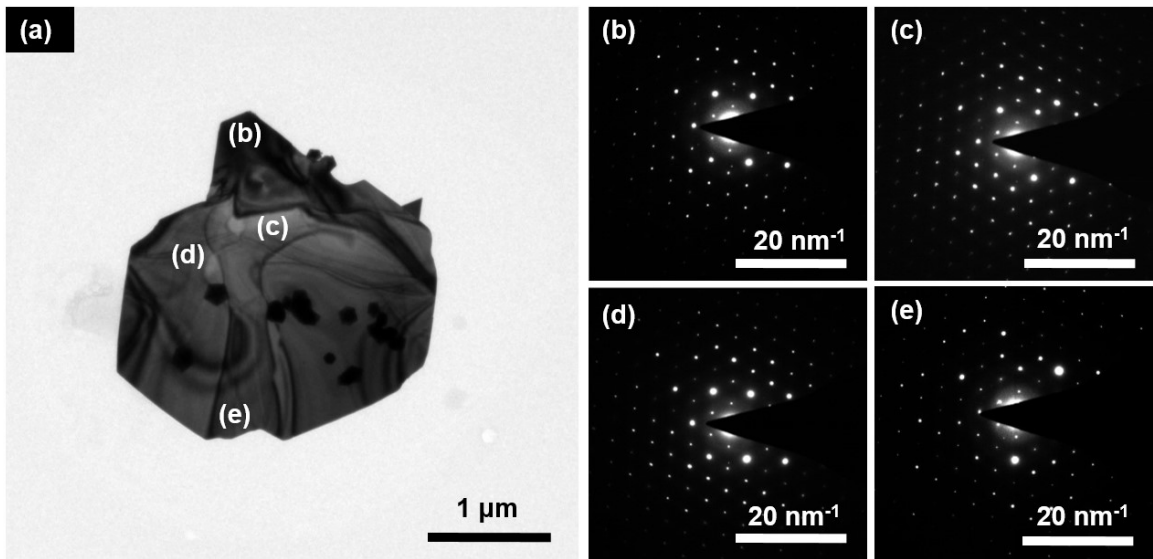


Figure 30. TEM image and SAED patterns of the gold nanoplate deposited at $T_d = 370^\circ\text{C}$, $P_{\text{THT}} = 45$ mtorr. (a) TEM image; (b-e) SAED patterns at different locations.

A relatively large and isolated feature (e.g., $3\ \mu\text{m}$) was imaged, along with some small nanoparticles exhibiting as hexagons, triangles and tetrahedrons (Figure 30a). Several positions on the plane were selected to fully characterize crystalline state since the nanoplate covered a large area (Figure 30b-e). The gold nanoplate presented a single-crystalline diffraction pattern with regular hexagonal. At least one group of forbidden diffractions was seen in the SAED with weaker intensity than the parent hexagonal pattern.

The diffraction spots showed similar arrangements among the four characterized positions, suggesting the same crystalline structure occurred throughout the plane.

2) Facet Identification of the Plane

The orientation of the face with respect to the direction of the electron beam was characterized to figure out the facet of the face. Such determination was made by measuring diffraction spots within the SAED pattern from Figure 30d (Figure 31).

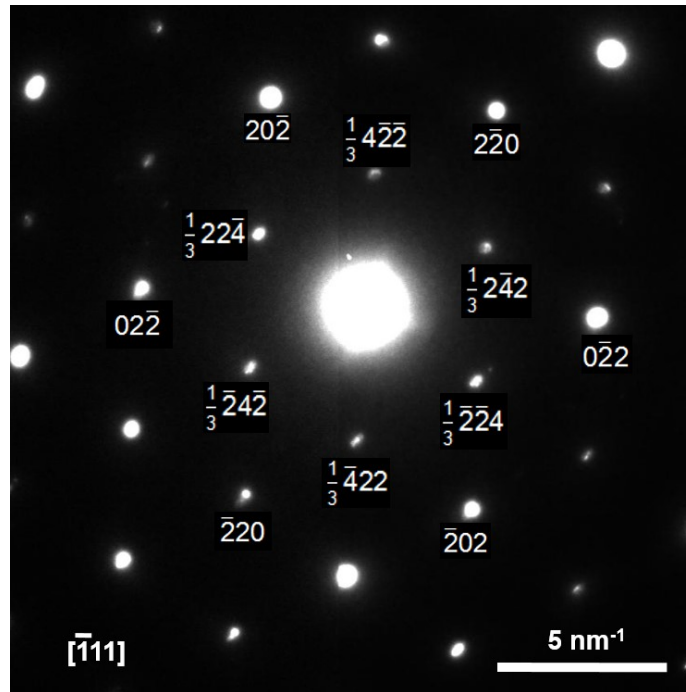


Figure 31. Facet identification of the gold nanoplate deposited at $T_d = 370^\circ\text{C}$, $P_{\text{THT}} = 45$ mtorr.

The facet distances were found by measuring the least distance of the symmetric spots through the center, calculating via Equation 8.¹¹⁷

$$d = \frac{2}{l} \quad (8)$$

Where d is the facet distance, nm; l is the least distance of two symmetric spots going through the center, nm⁻¹.

Two families of spots could be determined within the gold nanoplate. The 13.79 nm⁻¹ could be converted to a facet distance of 0.1450 nm which was characteristic for gold {220} facets.¹¹⁸ As allowed diffractions, the {220} spots were brighter and larger. Another value, 8.03 nm⁻¹, showed a facet distance of 0.249 nm. This value is the characteristic distance of the forbidden diffraction, $\frac{1}{3}\{422\}$,¹¹⁹ which evidenced the stacking fault in these gold crystals.^{59,120}

Then, via Equations 9-11, the direction of electron beam, $[uvw]$, can be calculated by obtaining two different diffractions, $\{h_1k_1l_1\}$ and $\{h_2k_2l_2\}$.¹¹⁷

$$u = k_1l_2 - l_2k_1 \quad (9)$$

$$v = l_1h_2 - h_1l_2 \quad (10)$$

$$w = h_1k_2 - k_1h_2 \quad (11)$$

With the discovered {220} and $\frac{1}{3}\{422\}$ diffractions, the calculated direction of the electron beam is $[\bar{1}11]$. As shown in Figure 32, the electron beam is perpendicular to the plane of the gold nanoplates, as well as those two diffraction groups. So the facet causing this diffraction pattern is {111} facet. All other diffraction patterns in Figure 30 showed similar results of spot positions and distances. Therefore, the plane of the gold nanoplate is verified as {111} facets.

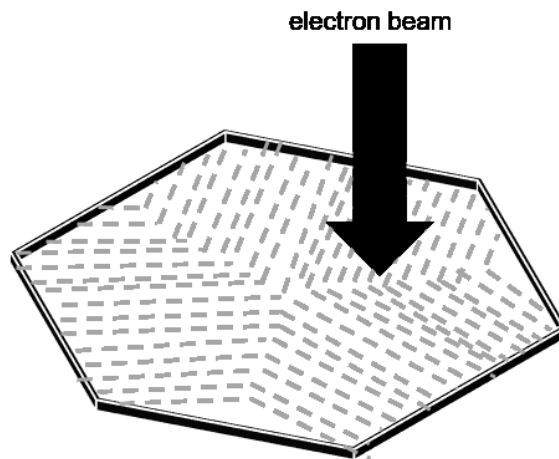


Figure 32. Model of spatial relationship between the electron beam and the gold nanoplates. The dashed lines represent assignments of gold atoms forming $\frac{1}{3}\{422\}$ facets. Reproduced with permission of Reference 120.

3.2 Role of Surfactant

3.2.1 Pressure Effects

1) 370°C Depositions

To distinguish the origin of shape control (i.e., whether it is due to THT or a change in pressure); gold depositions at 370°C were performed with an over-pressure 45 mtorr of THT or nitrogen (Figure 33). In the blank run, dense nanoplates with smaller sizes were observed (Figure 33a). Additionally, a lot of small particles along with several ribbons were as well. The shapes were highly irregular resulting from weaker shape control from the surfactants inherent in the ligand system of **4**. In contrast, with 45 mtorr of THT, nanoplate shapes were more filled out, which herein is defined as having a lower perimeter to surface area ratio (Figure 33c). Furthermore, small gold particles and ribbons were less

abundant. Even at a 30 μm scale, uniformed thickness could be assumed because of the similar shade of colors in the SEM image. The large gold flakes (e.g., 5 μm) had smooth surfaces and no secondary nucleation, showing effective shape control during the depositions (Figure 33d).

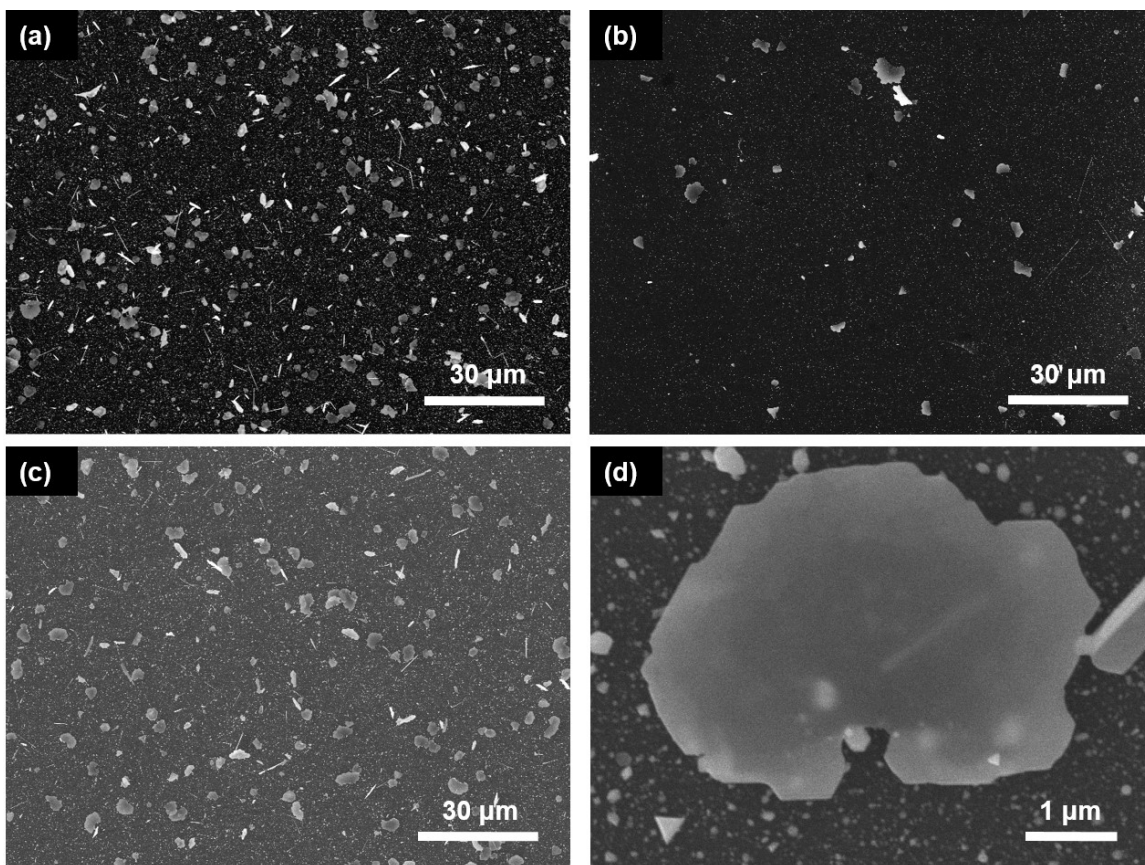


Figure 33. SEM images of gold particles deposited at $T_d = 370^\circ\text{C}$ with nitrogen or THT. (a) $P_{\text{THT}} = 0$ mtorr, $P_{\text{N}} = 0$ mtorr; (b) $P_{\text{N}} = 45$ mtorr; (c, d) $P_{\text{THT}} = 45$ mtorr.

The film moved 5 cm further along the deposition zone with 45 mtorr of nitrogen (Figure 33b). Nanoplates were still found, suggesting that the ligand system was exhibiting shape control on the gold particles. However, less dense nanoplates evidenced lower efficiency of the precursor supply on gold surface. Shapes were less symmetrical com-

pared with the blank and THT-assisted depositions. The nitrogen flow might change the precursor transport because branching growth on the nanoplates was more significant.

2) 430°C Depositions

At 430°C, similar depositions were performed with 15 mtorr of nitrogen to further investigate its effect on shape control. Compared with the blank depositions (Figure 34a, b), the nitrogen flow did not change the morphology of gold particles, nor the number of particles on the surface (Figure 34c, d). Several bigger nanoplates (e.g., 2 μm) were observed along with quantities of small nanoparticles. But the surface on the nanoplates showed obvious secondary nucleation. The shapes were still irregular and sizes were polydispersing. With 15 mtorr of THT, nanoplates were found in isolation, the faces of these plates were smooth with sharp edges and highly symmetric shapes (Figure 34e, f). Large nanoplates were easily discovered, again suggesting that THT was exhibiting excellent shape control.

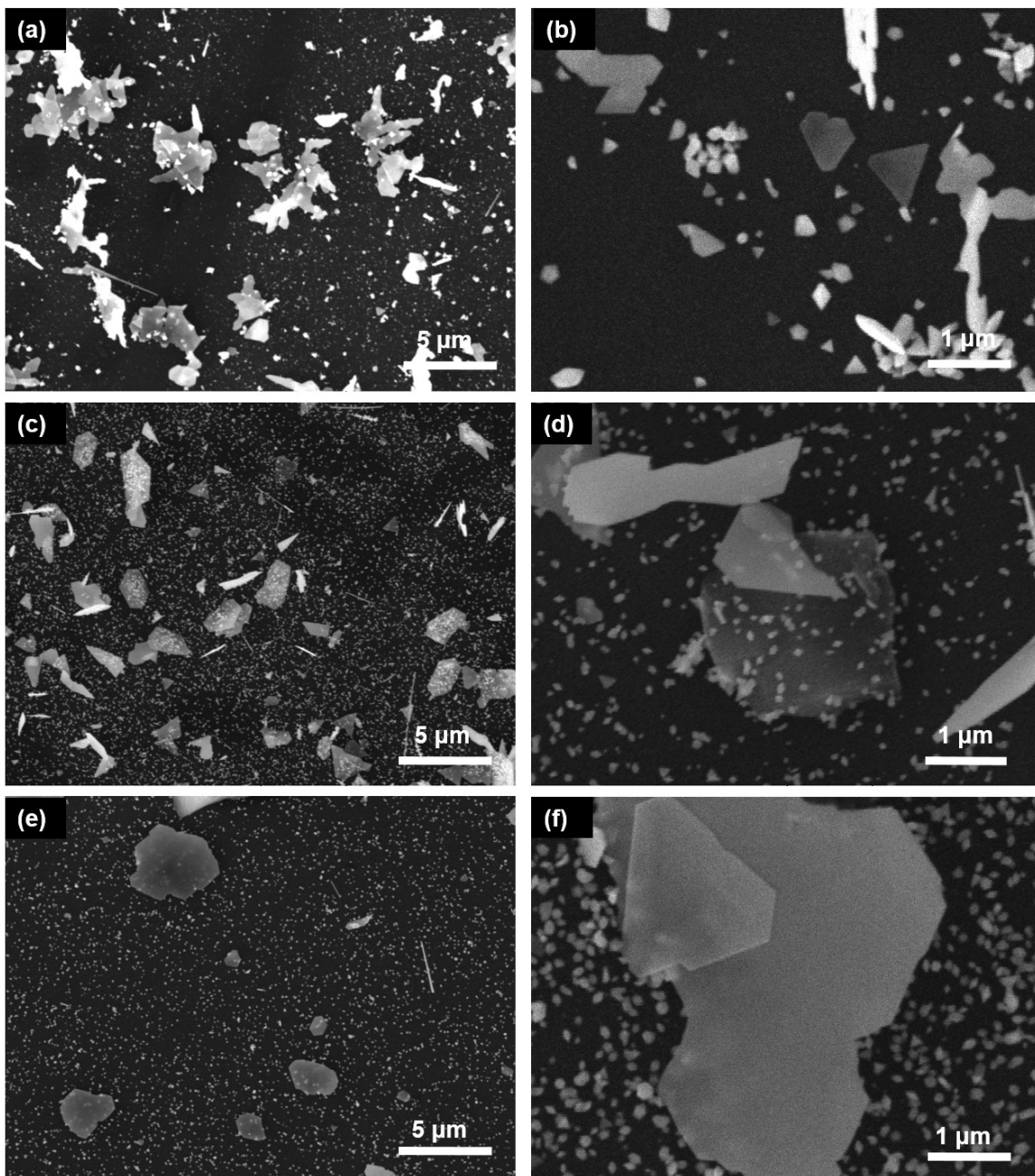


Figure 34. SEM images of gold particles deposited at $T_d = 430^\circ\text{C}$ with nitrogen or THT. (a, b) $P_{\text{THT}} = 0$ mtorr, $P_{\text{N}} = 0$ mtorr; (c, d) $P_{\text{N}} = 15$ mtorr; (e, f) $P_{\text{THT}} = 15$ mtorr.

3) Flow Conditions

In Table 2, molecular data were calculated to verify that the gas was flowing under the Knudsen condition. Assumed as standard air, the viscosity of gas in the CVD apparatus is 3.232×10^{-5} Pa·s at 370°C and 3.425×10^{-5} Pa·s at 430°C.¹²¹ At 370°C and 430°C, the *Kn* of nitrogen flow was both higher than the THT flow, leading to less viscous flow. In an enhanced Knudsen condition, intermolecular collisions occur less because of the longer MMFP.¹¹³ The coefficient of viscosity is significantly decreased resulting to higher diffusion. Consequently, the nitrogen flow allowed for stronger diffusion which accelerated the flow velocity to move the gold films further to the inlet end.

Table 2. Knudsen flow data of gases.

Flow	<i>P</i> / mtorr	<i>T</i> /°C	\bar{M}^*	$\lambda^*/10^{-4}$ m	<i>Kn</i> /10 ⁻²
Nitrogen	45	370	28.7	6.41	1.83
THT	45	370	41.9	5.31	1.52
Nitrogen	15	430	28.8	8.32	2.38
THT	15	430	34.0	7.66	2.19

* Including the air consisted of base pressure.

However, flow condition is not the only factor influencing gold film positions. Indeed, temperatures significantly affect film depositions including location of deposition (discussed in section 2.1). Higher temperatures give higher *Kn* values which lead to a lower probability of intermolecular collisions. *Kn* values can only predict general collisions in gas-phase environment. Yet chemical reaction depends on "effective collisions" between molecules which is heavily impacted by temperatures.¹¹¹ At higher temperatures, the precursors would be more easily activated to perform "effective collisions" with heat transfer

exceeding energy barriers. Thus, compared with the films at 370°C, the precursors still decomposed faster at 430°C and gold were deposited closer to the precursor inlet despite improved gaseous diffusion.

Above all, THT has been shown to effectively improve shape control of the gold metal nanostructures deposited by CVD.

3.2.2 Surface Morphology

1) Secondary Nucleation

Secondary nucleation is an enhanced growth leading to branched structures or embossments. It would negatively affect surface morphology of the gold nanoplates, consuming gold precursors inefficiently and causing surface roughness.

Using **4** only, secondary nucleation was obvious on the surface of the deposited gold particles (Figure 35a). It occurred either on the surface or at the edges to form irregular branched shapes. Moreover, gold aggregations were also produced, likely due to additional gold island nucleation sites on the surface. With 5 mtorr of THT, the gold nanoplates showed a clearer surface with less secondary growth (Figure 35b). The nanoplates grew larger and formed more regular shapes, suggesting improved shape control. But much non-uniformity still existed at the edges of the nanoplates. With 10 mtorr of THT, more and larger gold nanoplates could be found (Figure 35c). Secondary nucleation was less significant, though the surface was still rough. Shapes were less irregular presenting sharper and longer edges. With 15 mtorr of THT, less dense but even larger (e.g., 5 μm) nanoplates could be found with increasingly regular shapes (Figure 35d). The nanoplates

presented a smooth surface without secondary nucleation, as well as well-formed edges. Additionally, small nanoparticles were grown at the substrate surface.

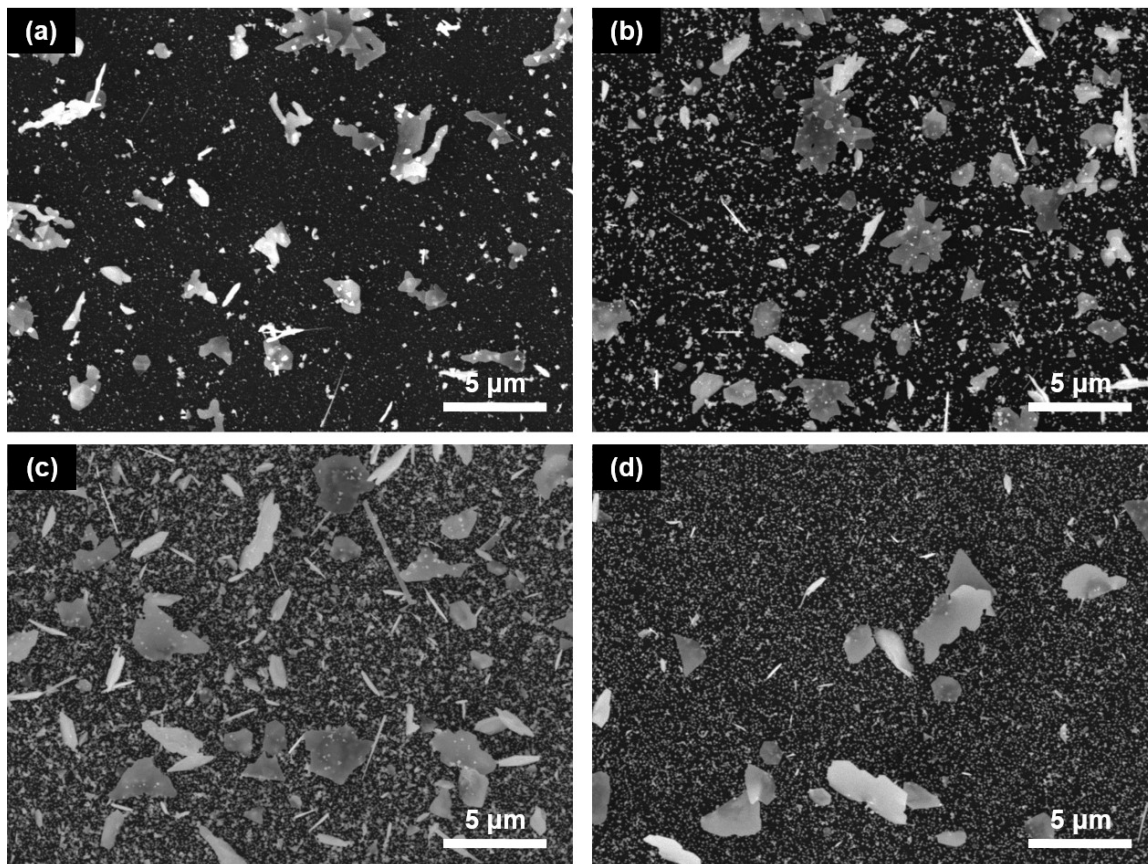


Figure 35. SEM images of gold particles deposited at $T_d = 430^\circ\text{C}$ with THT. (a) $P_{\text{THT}} = 0$ mtorr; (b) $P_{\text{THT}} = 5$ mtorr; (c) $P_{\text{THT}} = 10$ mtorr; (d) $P_{\text{THT}} = 15$ mtorr.

2) Surface Smoothness

Blank depositions with only 4 at 370°C produced a lot of simple gold nanoplates which were different from the types grown at 430°C (Figure 36a). These nanoplates were relatively small and grew alongside other nanoshapes (e.g., ribbons). Importantly, the surface was rough with embossments or hollows showing weak shape. Shapes were a highly irregular mix of hexagons, triangles and truncated structures. With 25 mtorr of THT, larger

gold nanoplates were present with fewer ribbons and other small particles (Figure 36b). The shapes of the nanoplates were more symmetric presenting better formed edges. However, imperfections could still be observed on the surface. With 35 mtorr of THT, the nanoplates demonstrated an even improved morphology with very smooth surfaces (Figure 36c). Eliminating sharp angles, the edges became smoother to form symmetric and regular shapes. Gold nanoplates with smooth and continuous surfaces resulted with 45 mtorr of THT (Figure 36d). No secondary nucleation could be found, which suggested good shape control during the depositions. Furthermore, large plates (e.g., 6 μm) could be seen with significantly smaller numbers of nanoparticles at the surface. Shapes were highly regular exhibiting hexagonal morphologies, with tiny amounts of triangles and ribbons.

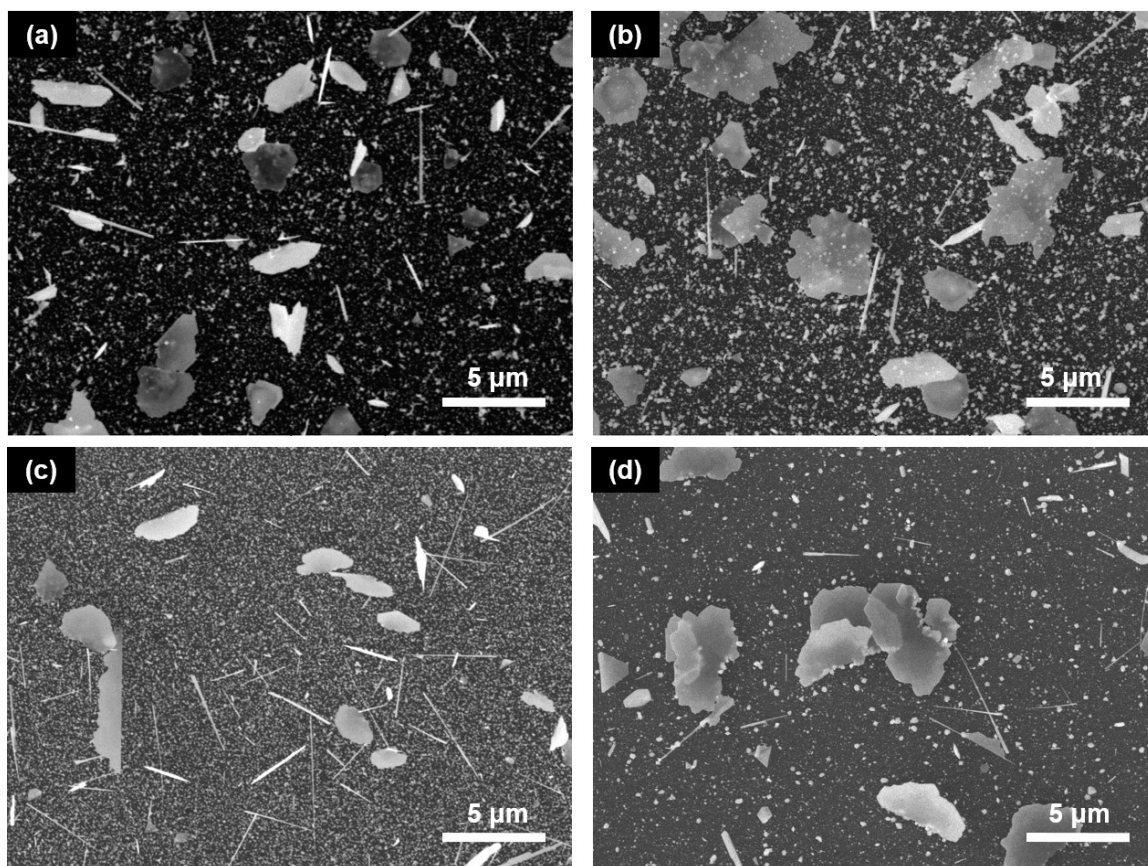


Figure 36. SEM images of gold particles deposited at $T_a = 370^\circ\text{C}$ with THT. (a) $P_{\text{THT}} = 0$ mtorr; (b) $P_{\text{THT}} = 25$ mtorr; (c) $P_{\text{THT}} = 35$ mtorr; (d) $P_{\text{THT}} = 45$ mtorr.

3) Models of Surface Construction

The surface model where the 1,3-diisopropyl-imidazol-2-ylidenyl ligands were adsorbed was demonstrated in the previous work.³² Due to the capability to lower surface energy, the carbene ligands were able to selectively cap the surface as a surfactant (Figure 37). Thus, gold nanoplates can be observed in the blank depositions with precursors only at both 370°C and 430°C (Figure 35a, 36a). However, the gold-carbene interactions are not strong enough on the growing surface, and this weak capping allowed the gold islands to

grow at different rates to form secondary nucleation, depending on the strength of carbene ligand adsorption.

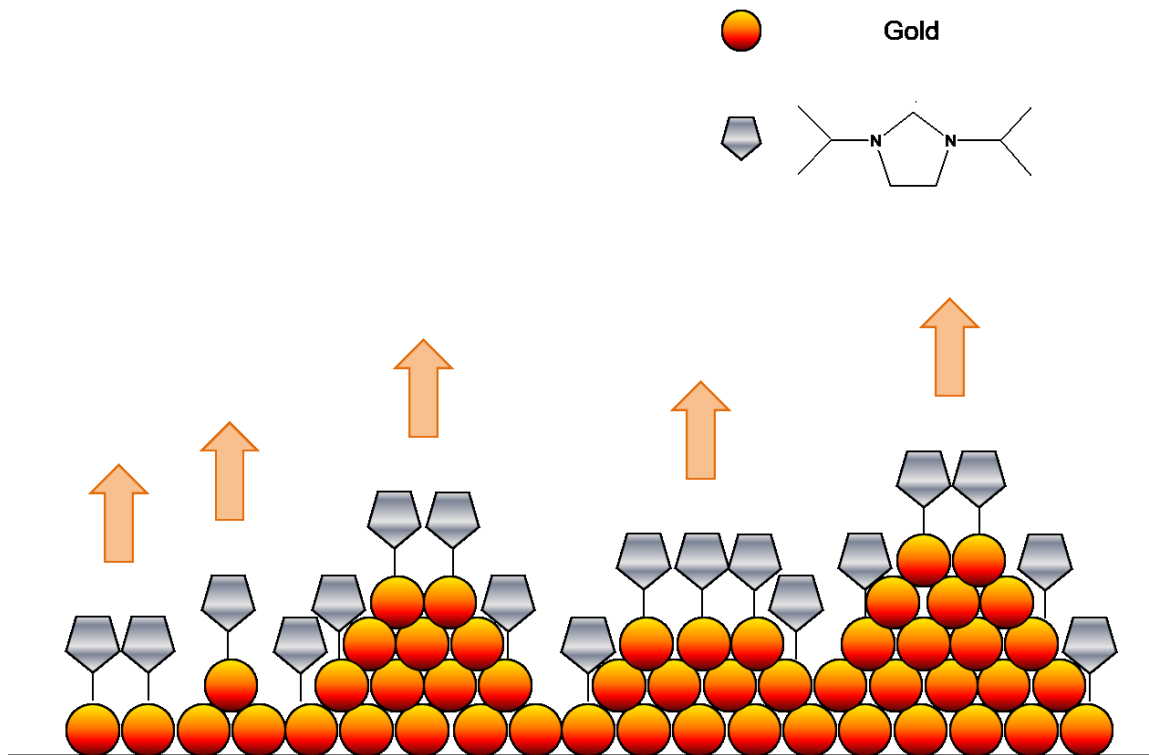


Figure 37. Growth model of the blank gold CVD.

When adsorbed to the growing gold surface, THT acts as a stronger surfactant by substituting the carbene ligands on the gold surface (Figure 38a). At lower pressures (e.g., 5 and 10 mtorr at 430°C), the substitution occurs but the concentration of THT is not high enough to fully cover the gold surface, capping partially instead (Figure 38b). At the sites capped by THT, gold islands grow more slowly due to the surface bond strength. In contrast, the faster growth on gold islands can still occur on sites occupied by the carbene. This leads to non-uniformity at the gold surface generating secondary nucleation. Thus,

due to the partial capping by THT, the gold nanoplates exhibit better shape control, a smoother surface, and more regular shapes than the precursor-provided carbene alone.

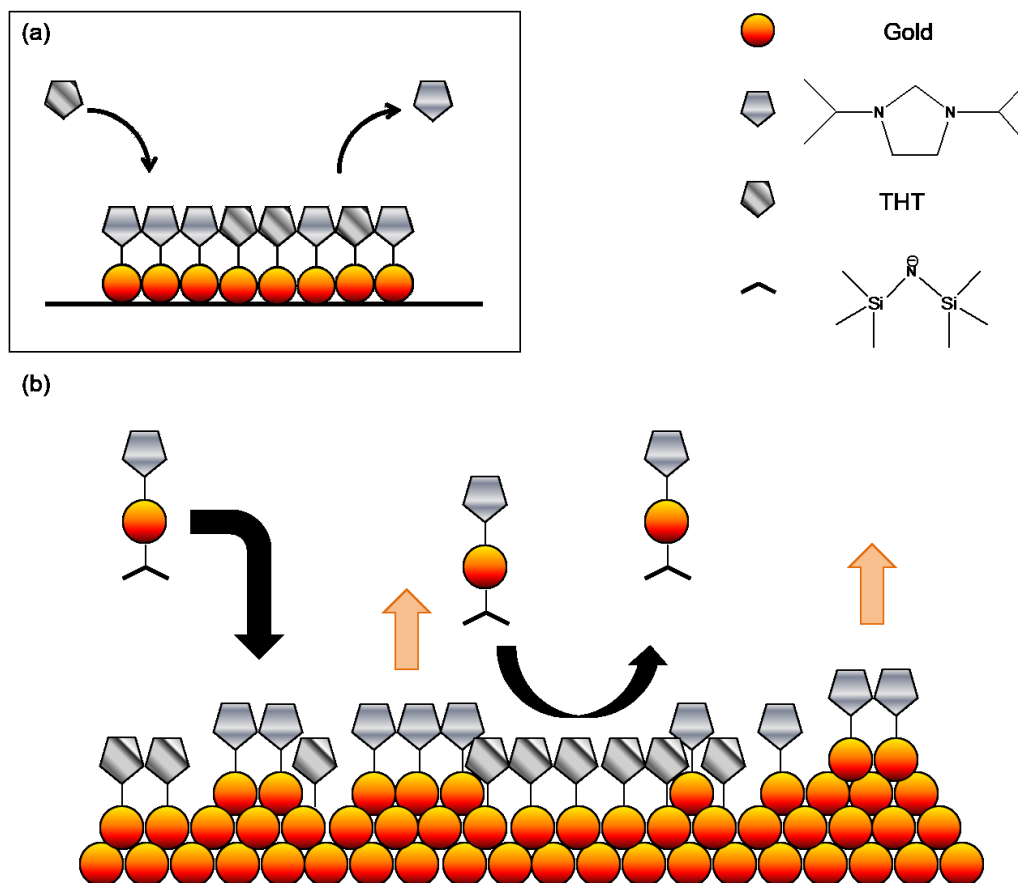


Figure 38. Growth model of the gold films with partially capped by THT. (a) ligand substitution; (b) different growth of gold.

At higher pressures (e.g., 45 mtorr at 370°C), THT caps the gold more efficiently to generate a smoother surface with lower surface energy. As with the higher surface energy, the stacking-faulted {111} plane would be preferably capped by THT to keep total surface energy within the particles low. Once the surface is fully capped, the gold precursors would seldom be adsorbed on the THT-covered face, thus avoiding further growth on the crystal islands (Figure 39a). Instead, the gold nanoplates grow at the edges enlarging the

nanoplate size (Figure 39b). Therefore, large hexagonal gold nanoplates exhibiting a {111} plane (e.g., 6 μm) are produced because of the capping effect of THT.

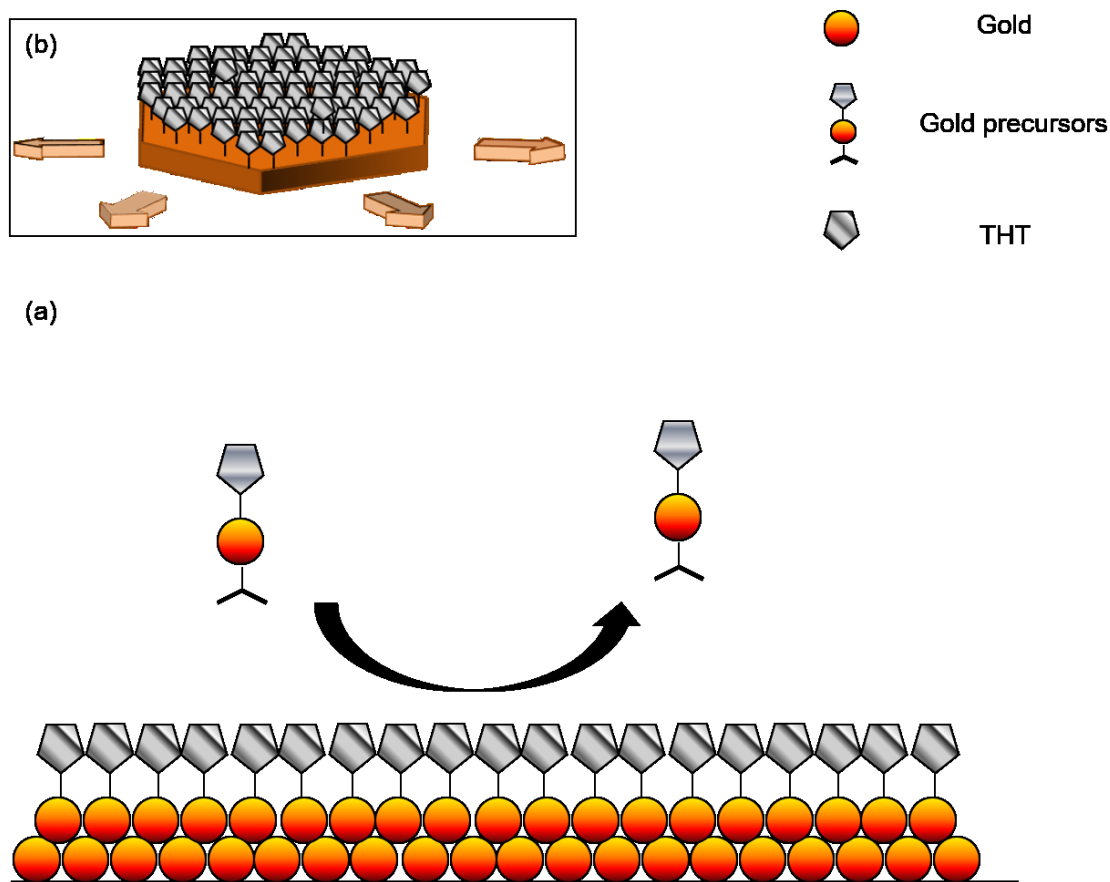


Figure 39. Growth model of the gold films with fully capped THT. (a) capping condition on the surface; (b) overall growth model of gold nanoplates.

It is interesting to note that during the precursor synthesis, THT is substituted by the N-heterocyclic ligands (Figure 14). However, THT is able to replace the N-heterocyclic ligands during the gold metal CVD. Likely reason for this is different Au-S bonding between THT gold (I) chloride and THT-capped gold (0) surface. THT makes a covalent bond with gold (I) via *sp* orbital hybridization, resulting to a linear compound (Figure 40a). However, gold (0) has been reported to make a weaker, coordination bond with the sulfur

lone pair to stabilize the gold particles.¹²² Thus, the bonding mode between THT and gold at the gold metal surface is a weaker interaction because both covalent bonding and anti-bonding orbital are fully occupied by electrons (Figure 40b). The strength of gold interaction on the surface significantly depends on the hydrophilicity of the surfactant compounds.

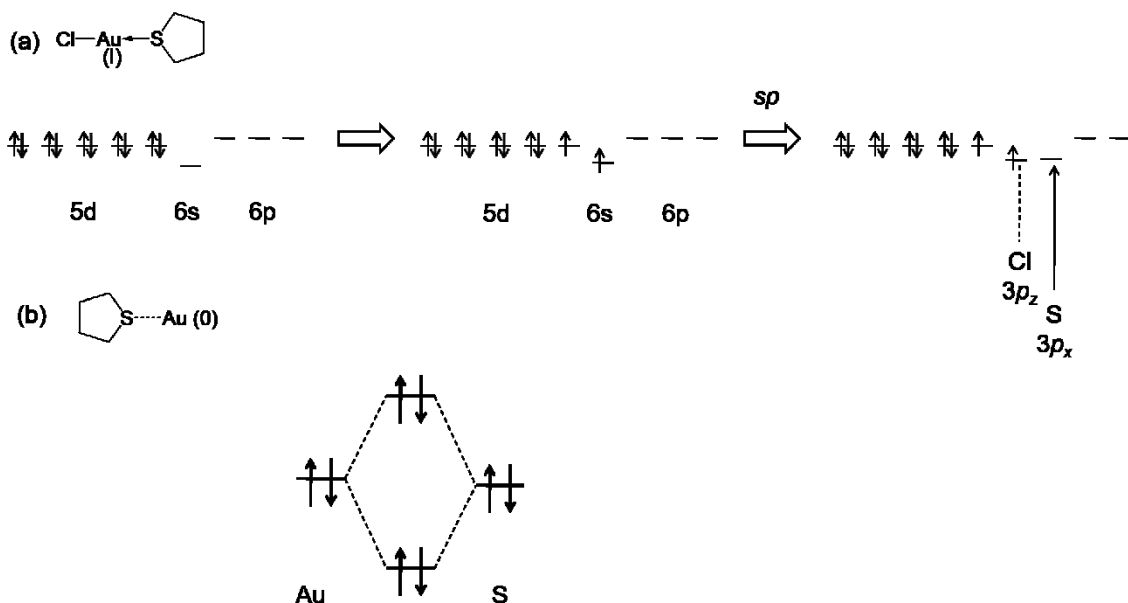


Figure 40. Models of bonding between gold and THT. (a) orbital hybridization for tetrahydrothiophene gold (I) chloride; (b) molecular orbital for THT-capped gold.

For the purposes of *HLB* ranking, sulfur is defined as the hydrophilic atom within THT compounds (Figure 41a). This gives it *HLB* 7.27, and so THT shows stronger hydrophilicity than the carbene with an *HLB* of 5.19. The carbene ligands are less hydrophilic because of their additional alkyl groups, as well as lighter hydrophilic atoms (Figure 41b). Accordingly, THT is more favored to reside on the gold surface, predicting substitution of the N-heterocyclic ligands. With a lower *HLB* of 4.40 (Figure 41d), the t-

butyl NHC showed even weaker shape control on the depositions, forming gold ribbons instead (Figure 23).

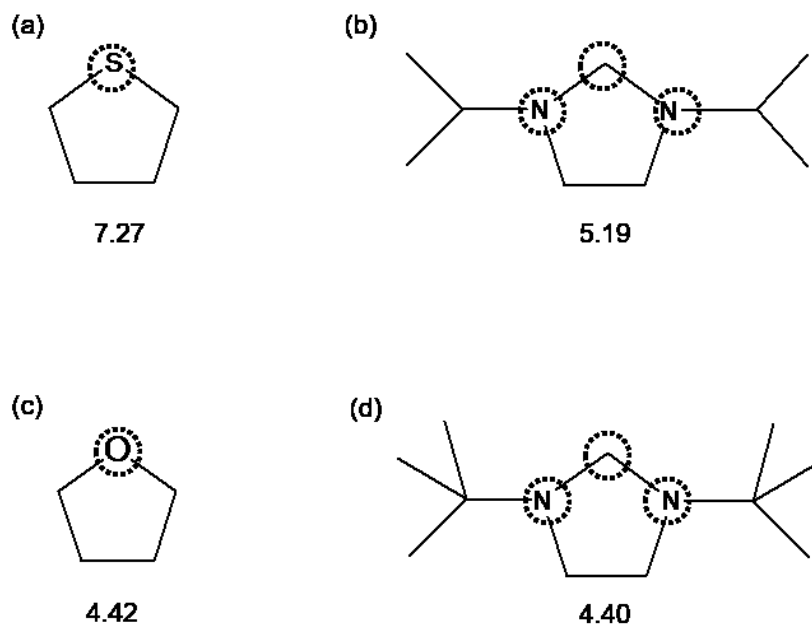


Figure 41. *HLB* values of compounds with circled hydrophilic atoms. (a) THT; (b) the N-heterocyclic ligands composing **4**; (c) THF; (d) the NHC.

HLB values are proportional to the coordinative interactions with gold because of gold's inherent hydrophilicity. Also, the coordinative interactions mainly depend on the polarity of the molecules. Within THT, the C-S dipoles are directed to the sulfur since its electronegativity (2.58) is slightly higher than carbon (2.55).¹²³ With component dipoles in the same direction, C-S dipoles contribute to the total dipole combining with dipoles of the lone pairs (Figure 42a). In contrast, in the NHC structures, the C-N dipoles are directed toward the nitrogen atoms which compete with the dipole of carbon lone pair (Figure 42b). Accounting for the additional methyl groups, the total dipole of the NHC is further decreased making even weaker molecular polarizations (Figure 42c). Thus, THT

presents the strongest interactions with gold, while the NHC is the weakest among these molecules, which agrees with the order of the *HLB* values.

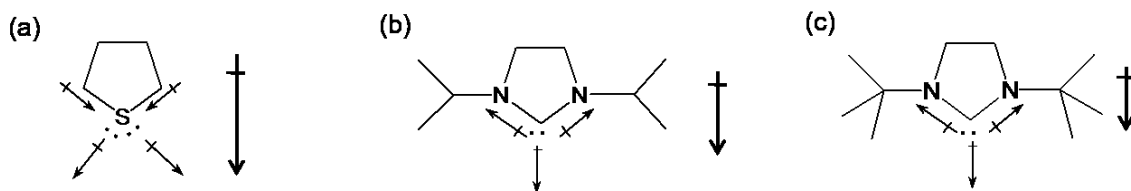


Figure 42. Models of dipoles for the surfactant molecules. (a) THT; (b) the N-heterocyclic ligands composing **4**; (c) the NHC. Bold arrows show total dipoles of the molecules.

3.2.3 Particle Size

Particle size is another important factor for this structural investigation. Temperatures are likely to change the mass and heat transport within the system. In the following section, depositions at different temperatures are discussed separately.

1) 430°C Depositions

At 430°C, gold depositions were performed with 0 mtorr, 5 mtorr, 15 mtorr, 25 mtorr, and 35 mtorr of THT. Without THT, gold particles with irregular shapes were obtained with a large disparity of sizes (Figure 43a). With 5 mtorr of THT, small hexagonal and triangular particles were found (e.g., 1.5 μm) (Figure 43b). The size distribution began narrowing, but sizes were still poly-dispersing. With 15 mtorr of THT, large gold nanoplates (e.g., 5 μm) were observed (Figure 43c). Compared with the blank run with **4** only, sizes were increased significantly although the nanoplates were now relatively isolated from one another. At 25 mtorr, THT showed similar size control keeping the nanoplates in the 5 μm range (Figure 43d). With 35 mtorr of THT, the isolated gold nanoplates again

showed similar sizes (e.g., 5 μm) compared with the other runs with THT (e.g., 15, 25 mtorr) (Figure 43e).

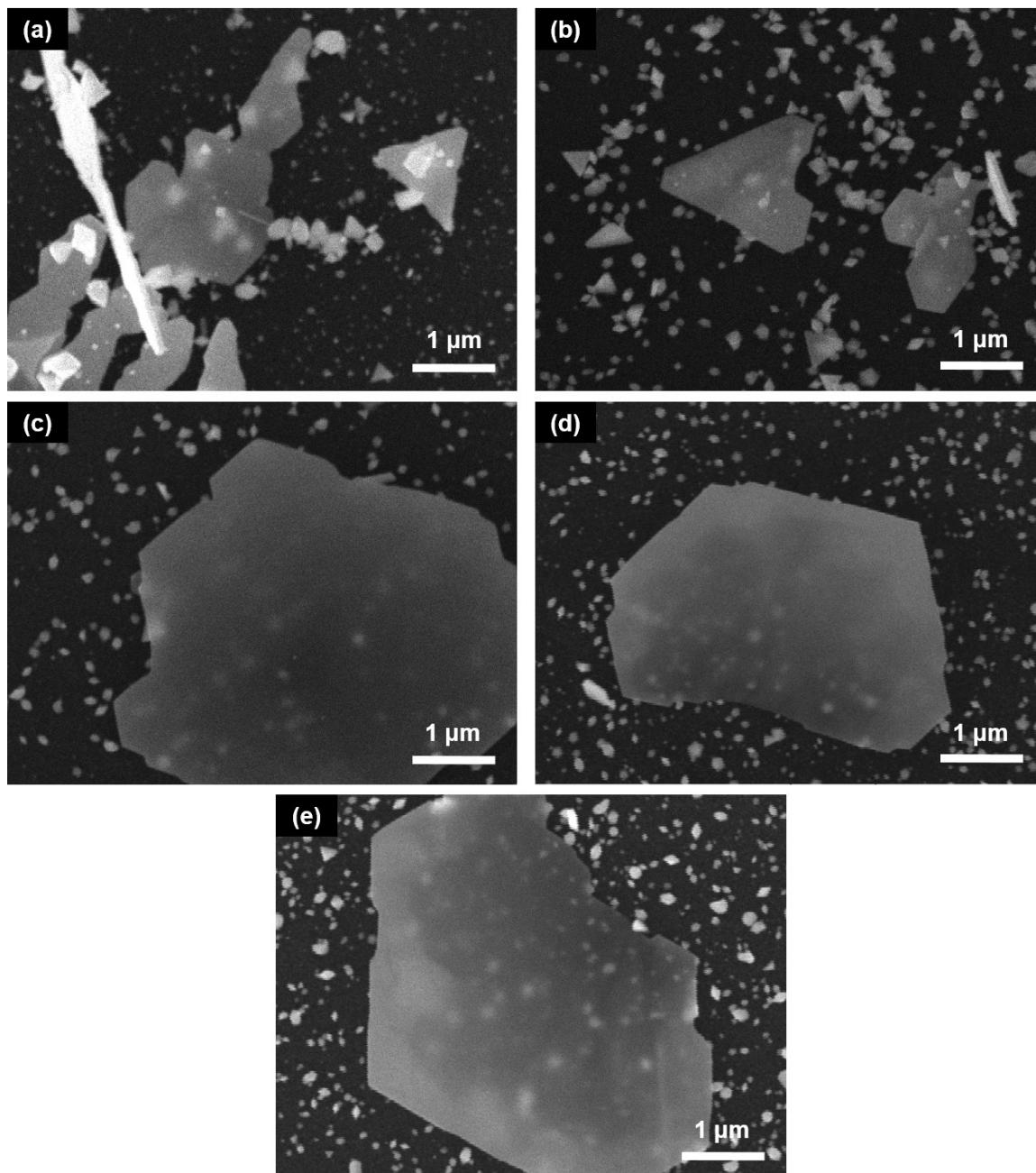


Figure 43. SEM images of gold particles deposited at $T_d = 430^\circ\text{C}$ with THT. (a) $P_{\text{THT}} = 0$ mtorr; (b) $P_{\text{THT}} = 5$ mtorr; (c) $P_{\text{THT}} = 15$ mtorr; (d) $P_{\text{THT}} = 25$ mtorr, (e) $P_{\text{THT}} = 35$ mtorr.

2) 370°C Depositions

Further size enhancement was investigated at 370°C by using THT. The blank depositions with only **4** showed larger gold nanoplates than those deposited at 430°C. Different trials were undertaken by using THT at 0 mtorr, 25 mtorr, 35 mtorr and 45 mtorr respectively. Without THT, only small nanoplates (e.g., 1 μm) were found as hexagons or triangles (Figure 44a). Sizes were more regular than those under the same flows at 430°C. With 25 mtorr of THT, hexagonal nanoplates grew bigger (e.g., 3 μm) in addition to there being less small particles (Figure 44b). With 35 mtorr of THT, even bigger (e.g., 4 μm) gold nanoplates could be observed along with smaller nanoparticles (Figure 44c). The biggest nanoplates (e.g., 6 μm) were found with 45 mtorr of THT (Figure 44d). In contrast, growth of small particles was significantly limited.

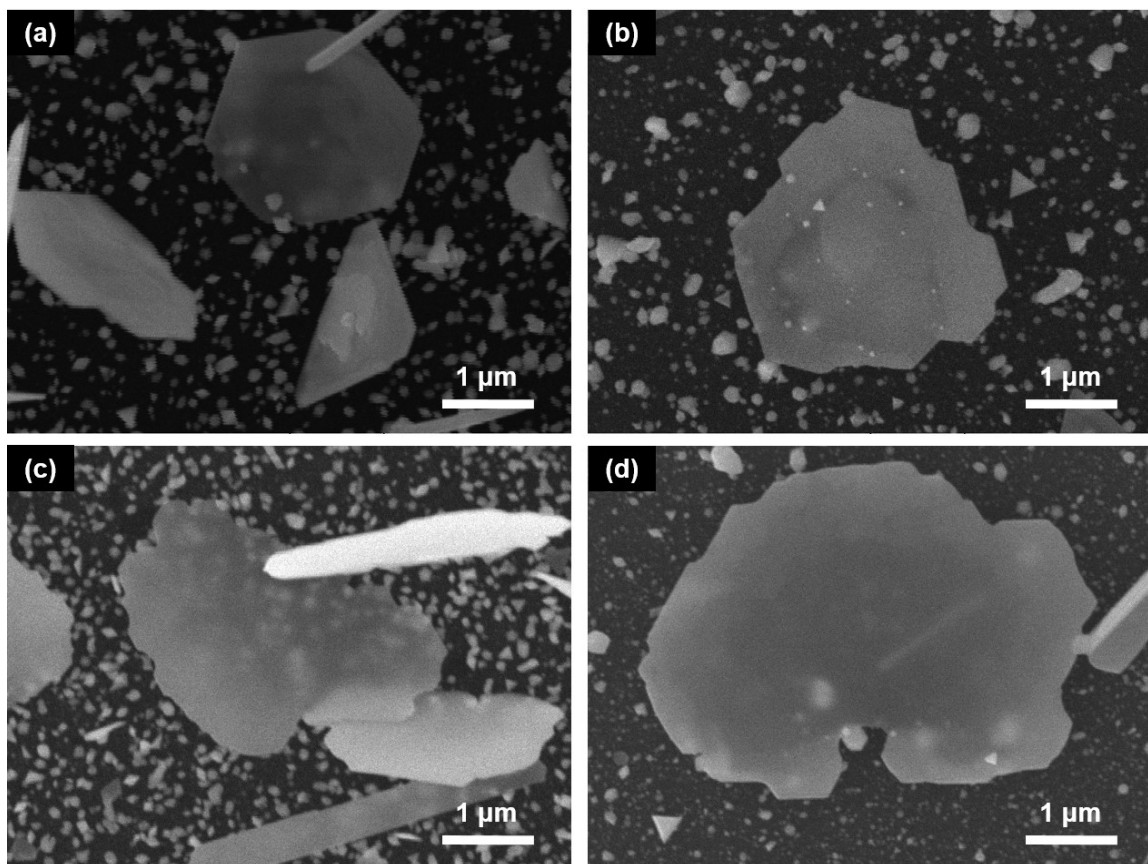


Figure 44. SEM images of gold particles deposited at $T_d = 370^\circ\text{C}$ with THT. (a) $P_{\text{THT}} = 0$ mtorr; (b) $P_{\text{THT}} = 25$ mtorr; (c) $P_{\text{THT}} = 35$ mtorr; (d) $P_{\text{THT}} = 45$ mtorr.

3) Models of Size Enhancement

A suggested model for size enhancement by THT is presented herein to show the mechanism of the flake growth (Figure 45). The particle size of the gold nanoplates was proportional to the pressure of THT within a certain range. To maintain the plane, THT preferably attaches to the gold $\{111\}$ plane attaining a lower surface energy. THT capping is suggested to play an essential role on growth preference varying sizes of the gold nanoplates.

Without THT, the gold precursors join in nanoparticle growth without selection accounting for similar surface conditions (1). Crystal seeds grow equally and more nanoparticles are produced, leading to precursor competition among those seeds. Thus, larger numbers of nanoplates are generated with small sizes, and nucleation continues to occur, giving a wide variety of plate sizes. In contrast, THT substitutes the carbene ligands to further lower the surface energy, giving higher stability of the gold plane (2). So the partially capped surfaces are more likely to attain gold adatoms at their growth edges, resulting in bigger nanoplates. Once the plane is fully capped, the surface will attract a high proportion of adatoms to reside at the edges of the nanoplates (3). Large gold nanoplates are easier to grow (e.g., 5 μm) with a dominant precursor supply. Therefore, the nanoplates grow with 45 mtorr of THT produce a larger plane than those with less THT because of the lower surface energy maintaining the plane.

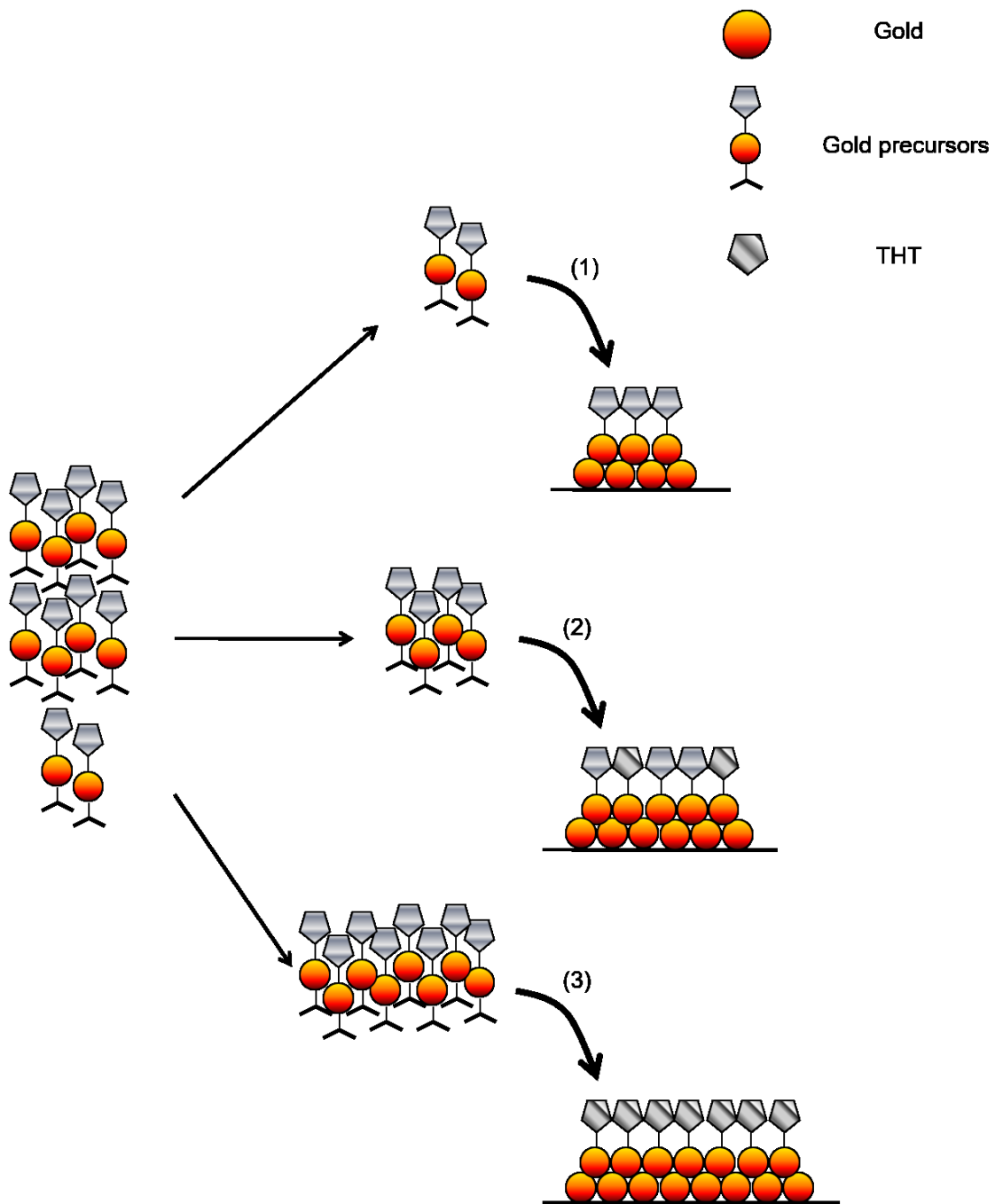


Figure 45. Growth models of the gold films with THT. (1) non-capped; (2) partially capped; (3) completely capped.

3.2.4 Surfactant Residual

Having residual THT on the gold surface post-deposition would be undesirable since this would add impurities at the surface that might impact the characteristics of the material. An ideal scenario would be if THT can be completely desorbed once the shape control is completed. Thus, compositional characterization was used to investigate the overall composition of the gold nanoplate surfaces. Specifically, XPS was used to determine the composition of the gold surface, and EDS was used to measure the bulk impurities.

1) EDS Spectrum

Sulfur is likely to reside on the surface at low temperatures because desorption occurs slowly which is potentially harmful to gold nanoplates. Consequently, gold nanoplates deposited at 370°C and 310°C were characterized by EDS analysis (Figure 46). Overlapping nanoplates attained at 370°C were selected since these had the best chance to show a strong sulphur signal (Figure 46a). Only gold and silicon signals were found, showing the purity of the obtained gold nanoplates (Figure 46b). A sulphur signal (~2.20 keV) could not be significantly measured with a detection limit (e.g., 1 at.%). From the films deposited at 310°C, a small nanoplate was chosen because there were no big nanoplates observed on the substrates (Figure 45c). Sulphur content could also not be measured here, and the spectrum showed only gold and silicon (Figure 45d). Using EDS alone is not sufficient to fully explore the elemental content in the gold nanoplates because the detection limit for such technique is high, and the penetration depth of the electrons is 10s of nanometers. Surface sulphur might be lost in the detection limit of such a technique.

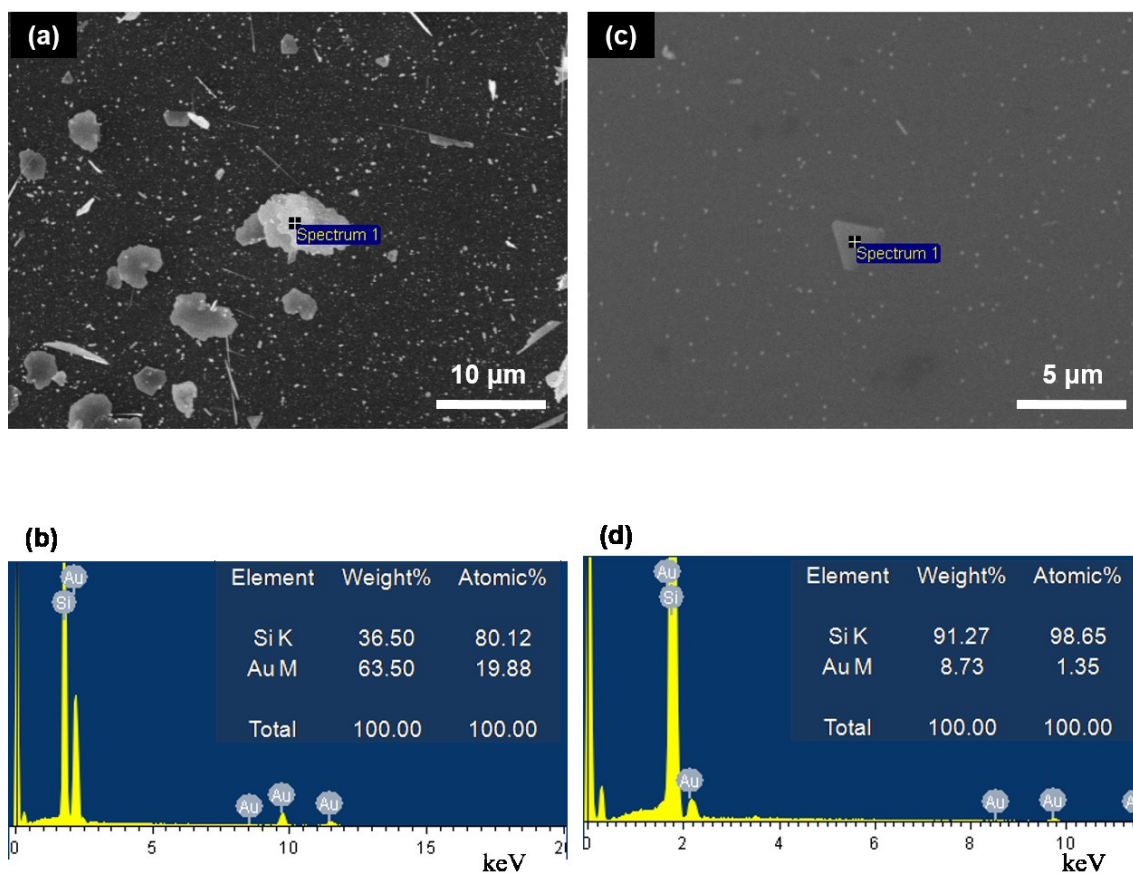


Figure 46. EDS spectra of gold particles at $P_{\text{THT}} = 45$ mtorr. (a, b) $T_d = 370^\circ\text{C}$; (c, d) $T_d = 310^\circ\text{C}$; (a, c) locations of the spectra (SEM); (b, d) elementary analysis of the gold films.

2) XPS Spectrum

With higher sensitivity (0.1 at%), XPS is a useful technique to characterize the composition of the gold nanoplates. It is especially suitable to determine elemental information on the surface since only electron escaping from the surface (50-70Å) can be detected. Gold nanoplates deposited at 370°C were selected for the XPS investigation. A strong peak (~ 533 eV) was found in the survey spectra (Figure 47a) which belonged to O_{1s} signal, probably coming from the incidental environment. Two similar peaks (~ 353 eV and 336 eV) corresponding to $\text{Au}_{4p_{3/2}}$ and $\text{Au}_{4p_{5/2}}$ and a small peak (~ 292 eV) for C_{1s} was discov-

ered. The carbon signal is likely due to adventitious carbon from the atmosphere. The peaks of Si_{2s} (~ 153 eV) and Si_{2p} (~ 99 eV) were found due to the silicon (100) substrate. Finally, another pair of gold signals relating to $\text{Au}_{4f 5/2}$ (~ 88 eV) and $\text{Au}_{4f 7/2}$ (~ 84 eV) were also found in the survey scan.

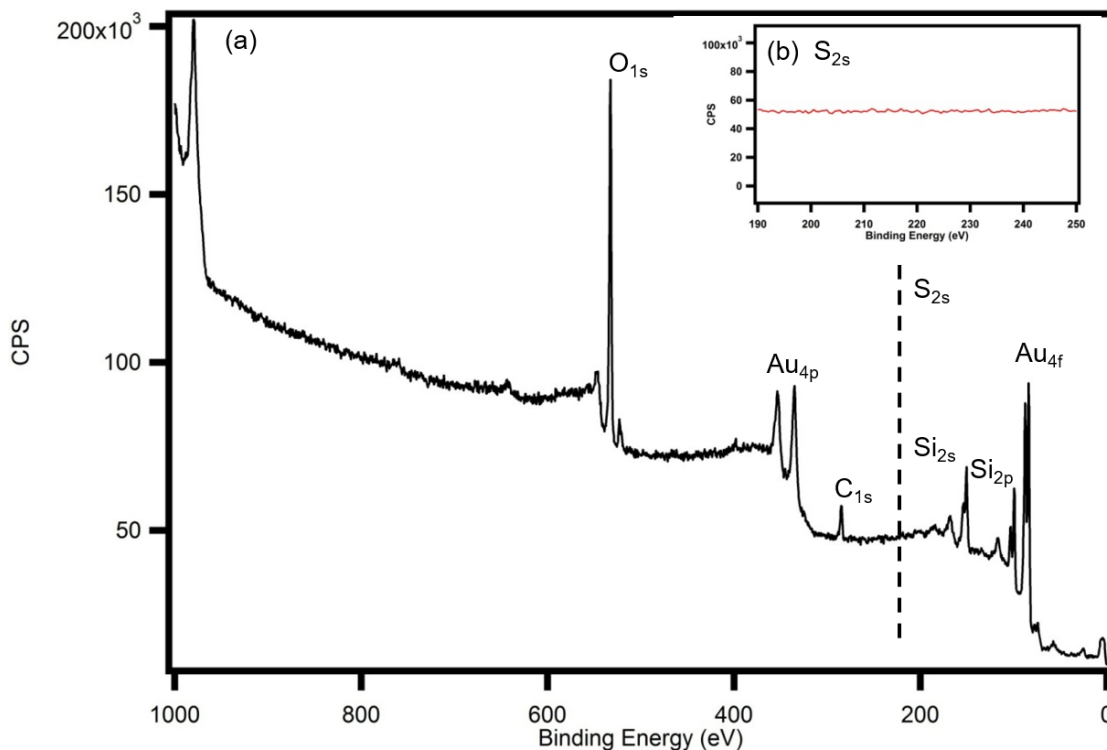


Figure 47. XPS spectrum of the gold films deposited at $T_d = 370^\circ\text{C}$, $P_{\text{THT}} = 45$ mtorr. (a) survey spectrum; (b) S_{2s} spectrum.

However, as a characteristic signal of sulfur, the peak (~ 229 eV, S_{2s}) was not found in both the survey and high resolution scan (Figure 47b). Thus there was no significant surface sulfur which implied THT were likely. Temperature is thought to play an important role on sulfur desorption. At high temperatures (e.g., 653 K), sulfur is desorbed from gold surface significantly in a short period.¹²⁴ So THT could be desorbed quickly during cool

down period of the gold CVD deposition. The moderate vacuum used during the depositions would be another factor as the sample was preserved under vacuum for 67 hours.¹²⁵

3.3 Gold Supply Control

Besides the surface activity of the surfactant, precursor supply is another significant factor for gold depositions. Typically, precursor supply is controlled by temperatures, flow conditions, and reactant additions. Precursor supply influencing gold nanoplates' formation is outlined in the following section.

3.3.1 Flake Density

With 35 mtorr of THT, gold depositions are considered at different temperatures. At 430°C, the large nanoplates (e.g., 5 μm) spread sparsely along with quantities of small nanoparticles (Figure 48a). At 370°C, dense gold nanoplates were deposited with uniform size (e.g., 5 μm) and a dense carpet of nanoparticles (Figure 48b). Regular nanoplates showed well-formed and smooth edges, which suggested more 4 preferably resided at the nanoplates. At 310°C, few identifiable shapes of gold could be found, only small nanoparticles (Figure 48c). In this case, density of the small particles would not likely to be increased compared with the runs at higher temperatures (e.g., 370°C and 430°C).

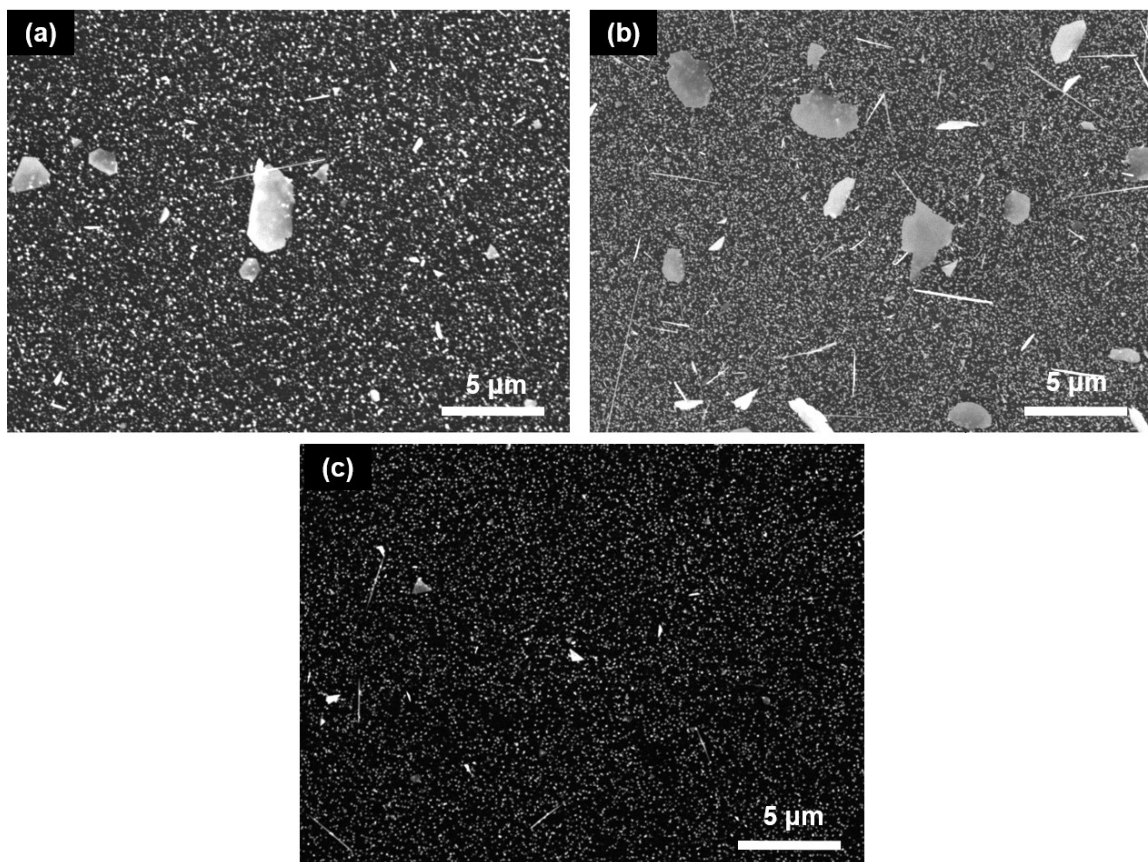


Figure 48. SEM images of gold particles at $P_{\text{THT}} = 35$ mtorr. (a) $T_d = 430^\circ\text{C}$; (b) $T_d = 370^\circ\text{C}$; (c) $T_d = 310^\circ\text{C}$.

The precursor **4** has limited thermal stability and its decomposition is sensitive to temperature.³² When heated, the **4** decomposed in the furnace, causing the pressure to increase approximately 5 mtorr. The pressure recovery as the temperature was lowered demonstrated that the precursor supply is not sustainable at high temperature. So at higher temperatures (e.g., 430°C), only isolated nanoplates were attained. However, low temperatures (e.g., 310°C) also cause shortage of the precursor supply. Slow decomposition generates surface-reactive precursors limiting the particle growth by surfactant chemisorption. Meanwhile, non-decomposed precursors are carried away along with the main

gas flow. Thus, a lower precursor concentration was experienced at the surface and produced a smaller number of gold nanoplates.

3.3.2 Shape Preference

Additionally, shapes can also be affected by gold supply during the deposition. At 310°C, small nanoplates were found which were mostly triangles, as well as ribbons (Figure 49a, b). In contrast, at 370°C and 430°C, large hexagonal nanoplates (e.g., 5 μm) were produced on the substrates (Figure 49c, d). Gold supply is mainly affected by temperatures, depending on decomposition rates. Slow decomposition leads to less precursor supply, producing less stacking-faulted hexagonal small nanoparticles. With less hexagonal seeds, singly twinned seeds would dominate the initial deposition, forming triangular nanoplates. Otherwise, nanoplates would be generated since those seeds are multiply twinned doubly with abundant stacking-faulted seeds (discussed in section 1.4).

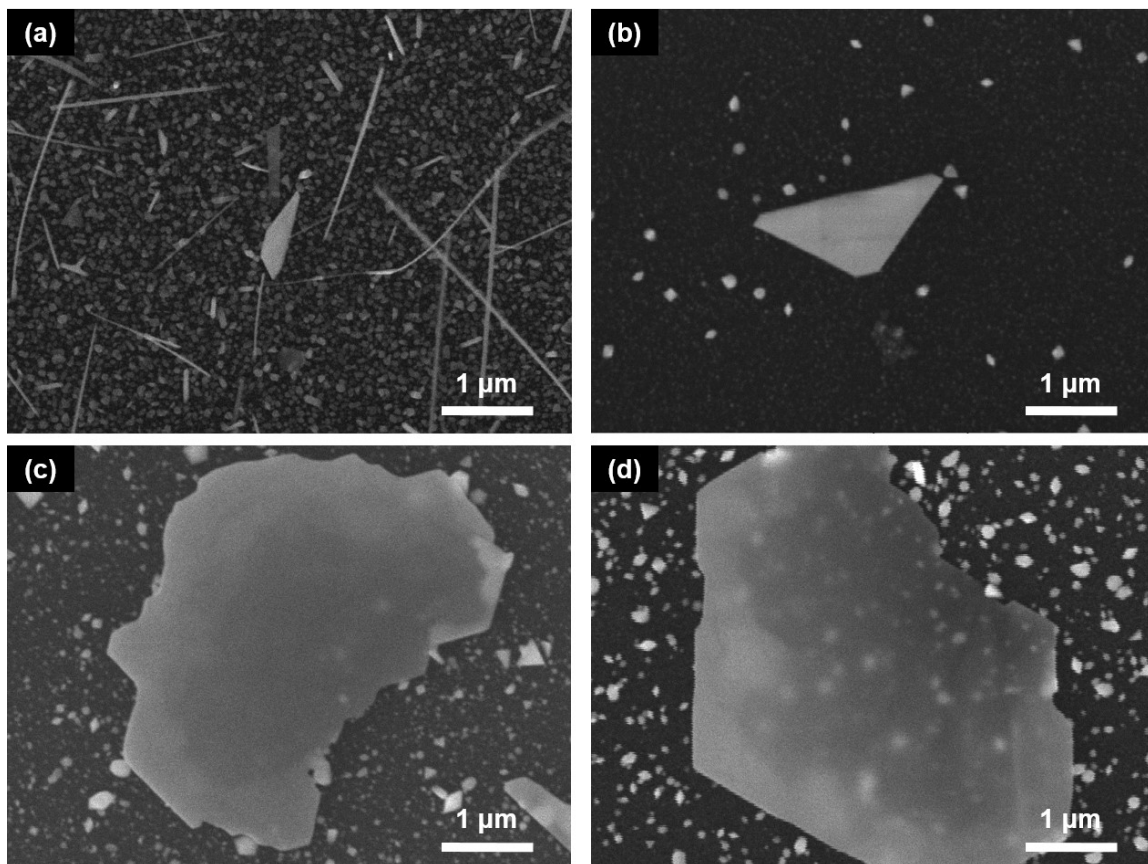


Figure 49. SEM images of gold particles with THT. (a) $T_d = 310^\circ\text{C}$, $P_{\text{THT}} = 15$ mtorr; (b) $T_d = 310^\circ\text{C}$, $P_{\text{THT}} = 45$ mtorr; (c) $T_d = 370^\circ\text{C}$, $P_{\text{THT}} = 45$ mtorr; (d) $T_d = 430^\circ\text{C}$, $P_{\text{THT}} = 35$ mtorr.

3.3.3 Particle Size

1) Exceeding Surfactant

At 370°C , only small nanoplates (e.g., $2\ \mu\text{m}$) could be found in the blank depositions using **4** only (Figure 50a). With 45 mtorr of THT, large gold nanoplates (e.g., $6\ \mu\text{m}$) with a smooth plane were evident (Figure 50b). Yet triangular nanoplates were found with 55 mtorr of THT, suggesting limited gold supply occurred (Figure 50c). The surface was rough with poorly-formed edges plane appeared, although there was no secondary nu-

creation. With 70 mtorr of THT, only small gold nanoparticles appeared on the substrates, smaller than those deposited without THT (Figure 50d).

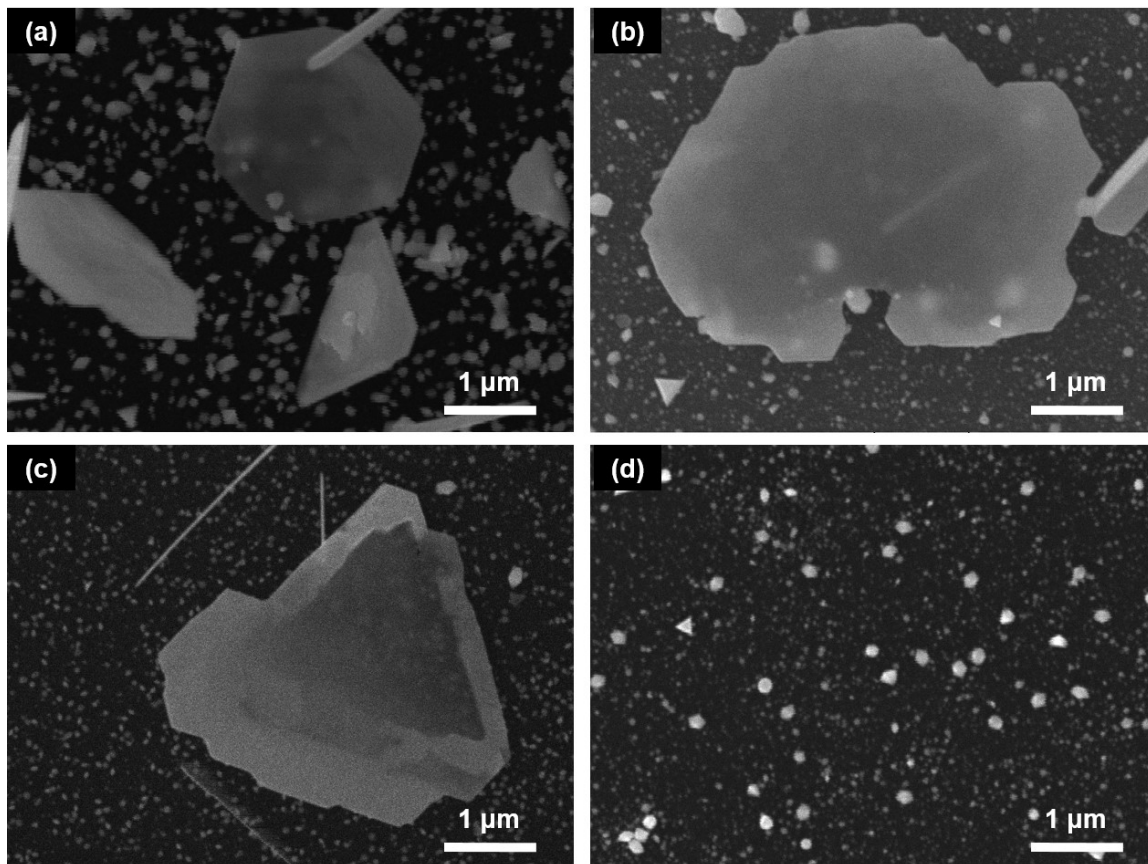


Figure 50. SEM images of gold particles deposited at $T_d = 370^\circ\text{C}$ with THT. (a) $P_{\text{THT}} = 0$ mtorr; (b) $P_{\text{THT}} = 45$ mtorr; (c) $P_{\text{THT}} = 55$ mtorr; (d) $P_{\text{THT}} = 70$ mtorr.

At 310°C , with 45 mtorr of THT, only small triangular or hexagonal nanoplates could be found, along with small nanoparticles and ribbons (Figure 51b). These particles were no larger than those from the blank depositions with **4** only (Figure 51a). With 55 mtorr and 70 mtorr of THT, gold particles with identifiable shapes were rare and the surface was sparsely covered by small nanoparticles (Figure 51c, d). These nanoparticles were smaller than from the blank depositions, and similar to the depositions at 370°C .

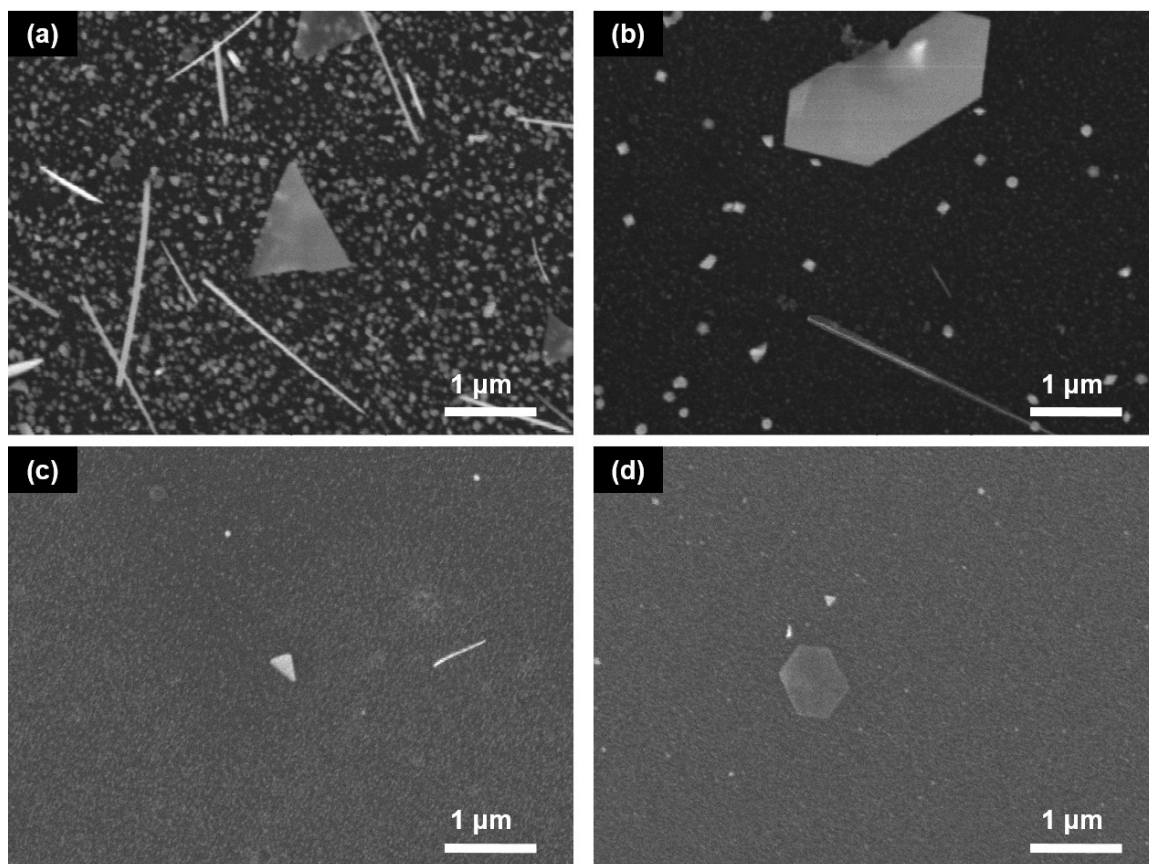


Figure 51. SEM images of gold particles deposited at $T_d = 310^\circ\text{C}$ with THT. (a) $P_{\text{THT}} = 0$ mtorr; (b) $P_{\text{THT}} = 45$ mtorr; (c) $P_{\text{THT}} = 55$ mtorr; (d) $P_{\text{THT}} = 70$ mtorr.

When THT was introduced prior to the introduction of **4**, there were no gold depositions, with condensed material remaining in the bubbler. This material was collected and characterized by ^1H nuclear magnetic resonance (NMR) analysis to inspect the composition. This showed that the precursor had decomposed, and no composition could be easily assigned.

The gold precursor was consumed very quickly, and can result in significant limitation of gold supply during the deposition. At high temperatures, the gaseous precursor concentration could be lowered by thermal decomposition. At lower temperatures (e.g.,

40°C), THT vapor could condense in the precursor bubbler. There, THT could react with **4** and leave the non-volatile byproducts in the bubbler. For general depositions, once saturated adsorption on the gold surface occurred, the excess THT might remain in the deposition atmosphere and reacted with **4**, diminishing precursor concentration.

2) The Best Points

To clearly outline the results based on the surface area of gold nanoplates and pressures of THT, an approximation of surface area was made (Figure 52). With obvious shape control, THT increased the surface area to about 20 μm^2 at 430°C, and it stabilized there even when more THT was added (1). At 370°C, increasing THT helped to enlarge the gold nanoplates until about 40 mtorr, where the size then started to decrease with excess THT (2). Few significant shapes could be determined at 310°C because of limited precursor concentration during the depositions (3).

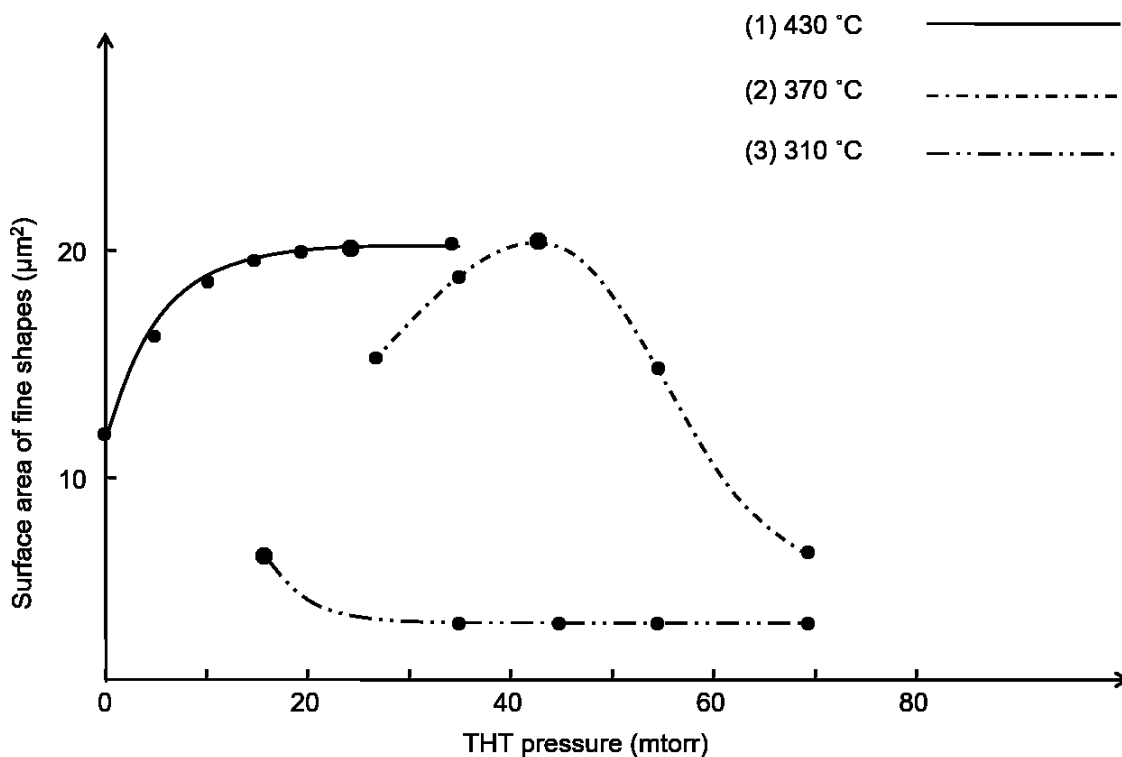


Figure 52. Surface area-THT pressure relation curve on fine gold particles. (1) $T_d = 430^\circ\text{C}$; (2) $T_d = 370^\circ\text{C}$; (3) $T_d = 310^\circ\text{C}$.

3.4 Summary

In this chapter, detailed research was performed on shape control of gold nanoplates via THT-assisted gold CVD. Large gold nanoplates (e.g., 6 μm) with a smooth surface were found, and confirmed to be single crystalline with a $\{111\}$ plane. The evidence of gold stacking fault was found by the identification of $\frac{1}{3}\{422\}$ diffractions in the SAED patterns.

The role of THT as a surfactant was studied by altering the over-pressure of the surfactant. Adding intermediate pressures of THT (e.g., < 45 mtorr) enhanced surface morphology of the gold nanoplates including suppression of secondary nucleation and nano-

particle formation. Sulfur was not found as an impurity, suggesting these structures were pure gold nanoplates.

Affected by THT and temperatures, the gold adatom supply was also an important factor on nanoplate growth. Gold particles formed triangles or hexagons via single or multiple twinning through stacking-faulted seeds whose concentration was dependent on precursor supply. In addition to density, adatom availability had a significant impact on size of the gold nanoplates. Excessive THT reacted with the precursors in the gas phase to limit the precursor concentration resulting to small size and sparsely deposited gold nanoparticles.

4 Conclusions

Dense large (e.g., 6 μm) gold nanoplates were attained via CVD at 370°C with 45 mtorr of THT. Also isolated nanoplates in similar size could be found at 430°C with THT pressures between 15 mtorr and 35 mtorr. Meanwhile, few identifiable shapes were found at 310°C.

Compared with the double-feeding-route system, the newly constructed single-feeding-route CVD apparatus was more successful for gold metal CVD. The blank depositions showed reproducible results which were similar to the previously reported depositions.³² Due to free radical reactions, THF was not useful as surfactant for the gold CVD at elevated temperatures. Although some shape control was evident, the selected NHC did not satisfy the requirements of shape-controlled CVD since only ribbons and small nanoplates were found in the deposited gold films.

THT, as a surfactant, was successfully used to prepare large gold nanoplates with a smooth $\{111\}$ plane via CVD. The gold nanoplates were confirmed single-crystalline due to the regular diffractions in SAED patterns. Showing $\frac{1}{3}\{422\}$ diffractions, the stacking fault on gold particles was evident, showing the plane to be $\{111\}$ facets. Both EDS and XPS showed the nanoplates were pure gold without elemental residue from surfactants.

Compared with nitrogen, THT showed evidence of significant improvement over shape control of gold particles, as well control of size and flake density. THT substituted carbene ligands on the gold $\{111\}$ plane to stabilize the shape due to the stronger coordinative interaction of the $\text{Au}^0\text{-S}$ bond. Secondary nucleation was significantly eliminated due to the preferable capping of THT. Size enhancement was also found by adding THT

during the gold depositions because THT-capped particles grew more. EDS and XPS presented evidence that THT was fully desorbed.

Gold adatom supply was found to be essential for shape control of gold nanoplates, and this supply was impacted strongly by temperatures. It would also have an effect on the mechanism of crystal twinning to select particle shape between triangles and hexagons. Particle size was also affected heavily by gold supply due to the competition with small nanoparticles. Excess THT was suggested to react with the gas phase precursor molecules to limit the concentration, which led to small particles on the substrates.

5 Future Work

THT was found to be effective for strong shape control on gold particles. Also, the exploration of gold CVD was enhanced because of better understanding of the growth mechanism of gold seeds and structures. Some work is suggested to be performed in the future.

Since the shape of nanoparticle seeds is sensitive to temperature, gold precursor should be continued to develop so that a wider range of temperatures can be accessed. This is an essential step to produce other specific shapes of gold particles via CVD.

Surfactant selection should be continued to find an even stronger shape controller for the gold depositions. Since sulfur was found to be effective for producing gold nanoplates, similar molecules with sulfur atoms could be considered, like diethyl sulfide and dibenzyl sulfide.

The growth mechanism of gold should be further explored. It remains unknown what the initial precursor concentrations and addition has on the ultimate particle shape. It is expected that some differences would be found at this point.

As bigger nanoplates were found, nitrogen flow could be another branch for future work: flow change seemed to result in different gold surface morphology. For a "greener" chemistry approach, huge enhancements would be expected if particle shape is able to change with inert gas flow only.

6 Experimental Section

General Considerations. Unless otherwise noted, reagents were ordered from Strem Chemicals, Sigma Aldrich or Alfa Aesar. All compounds were synthesized based on literatures.^{32,126,127} Acetone was distilled from reactant grade products and stored over active 3A molecular sieves. Air-sensitive experiments were performed in a nitrogen flowing Schlenk line or MBraun Labmaster 130 dry box. ¹H NMR data were attained from a Bruker AMX 300MHz spectrometer, calibrated by TMS (0 ppm) for CDCl₃ and C₆D₆ (7.16 ppm).

Tetrahydrothiophene Gold (I) Chloride (1). H₂AuCl₄·3H₂O (8.800 g, 21.4 mmol) was dissolved in a mixture of water (20 mL) and ethanol (100 mL) in a 250 mL beaker, forming a clear orange solution. At room temperature, THT (4.50 mL, 51.1 mmol) was dropped into the solution on a stirring plate, changing the color to deep yellow. The stirring was continued for 1 hour until a white suspension was produced. The white solid was filtered, and washed by diethyl ether (3×20 mL), then dried for 10 hours under vacuum, yielding 97.7%.

Lithium Hexamethyldisilazide·Diethyl Ether (2). In a 250 mL Schlenk flask, hexamethyldisilazane (7.202 g, 44.6 mmol) was stirred with diethyl ether (100 mL) for 5 minutes. On a Schlenk line, 1.6 M n-butyl lithium hexane solution (25.0 mL, 40.0 mmol) was dropped onto the suspension which was cooled to 0°C in an ice bath. The mixture was warmed to room temperature, and then stirred for 2 hours, turning to a clear and colorless solution. White solid was obtained after drying for 8 hours under vacuum, with a yield of 92.6%.

1,3-diisopropyl-imidazolidin-2-ylidene Gold (I) Chloride (3). In a dry box, 1,3-diisopropyl-4,5-dihydro-3*H*-imidazol-1-ium chloride (1.654 g, 8.68mmol) was suspended in a 250 mL Schlenk flask with tetrahydrofuran (100 mL). **2** (1.951 g, 8.08 mmol) was dissolved in diethyl ether (80 mL) in another flask. On a Schlenk line, the suspension was cooled to 0°C in an ice bath, and the **2** solution was dropped by cannula transfer. The mixture was warmed to room temperature and stirred for 1 hour, to get a clear yellow solution. Under nitrogen, **1** (2.590 g, 8.50 mmol) was added by 5 portions over 20 minutes to the yellow solution which was cooled to -78°C in a dry ice-isopropanol bath. Warmed to room temperature, the mixture was kept stirring for 18 hours. A dark purple solid was recovered after trap-to-trap distillation at 0°C, and dried for additional 2 hours under vacuum. Brought into a dry box, the solid was extracted by dichloromethane (3×20 mL) and filtered by using a glass frit. The dichloromethane was removed by a rotary evaporator, to get a dark orange solid with a yield of 96.3%. ¹H NMR (300 MHz, CDCl₃): δ 4.76 (sept, 2H, CH(CH₃)₂), δ 3.53 (s, 4H, CH₂CH₂), δ 1.22 (d, 12H, CH(CH₃)₂).

1,3-diisopropyl-imidazol-2-ylidene Gold (I) Hexamethyldisilazide (4). In a dry box, **2** (1.756 g, 7.27 mmol) was added to a 150 mL round bottom flask and dissolved in toluene (70 mL). **3** (2.704 g, 6.99 mmol) was suspended with toluene (150 mL) in another round bottom flask. Both mixtures were chilled to -35°C in a freezer. The **2** solution was added dropwise to the **3** suspension. The reaction was kept for 21 hours by stirring at room temperature, protected by foil from light, attaining a black suspension. The suspension was filtered through a 0.5 cm Celite pad which was washed by toluene (50 mL) afterwards, affording a yellow solution. Crude dark blue solid was obtained after drying. White purified product was found after sublimation (100 mtorr, 90°C) with a -78°C cold

finger, yielding 67.4%. ^1H NMR (300 MHz, C_6D_6): δ 4.82 (sept, 2H, $\text{CH}(\text{CH}_3)_2$), δ 2.40 (s, 4H, CH_2CH_2), δ 0.78 (d, 12H, $\text{CH}(\text{CH}_3)_2$), δ 0.62 (s, 18H, $\text{Si}(\text{CH}_3)_3$).

Chemical Vapour Deposition. Surfactant (5.0 g) was added to a small vial and placed in the surfactant bubbler, which was then frozen to -120°C in an ethanol-liquid nitrogen bath for 30 minutes. To remove air, the bubbler was evacuated and then sealed under vacuum, kept in a water bath at room temperature. **4** (50 mg) was added to an open-ended vial, and spread thoroughly on the wall. The vial was sealed in the precursor bubbler. Substrates were put at specific locations on a metallic boat which was placed at the precursor inlet end of the furnace pipe. The CVD system was then put under vacuum for 2 hours (160 mtorr) and the furnace (LINDBERG/BBLUE HTF 55322A Hinged Tube Furnace) was preheated to the desired temperatures (LINDBERG/BBLUE CC58114A Control Consoles). The feeding system except bubblers was heated and kept at around 100°C for 2 hours as well. Afterwards, the precursor bubbler was quickly heated and stabilized at around 87°C . The surfactants were released at designated pressures once the precursor bubbler reached 70°C . The depositions lasted for 2 hours, after which an additional 30 minutes was employed without surfactant input. Finally, the vacuum was removed by flowing nitrogen and the cooled substrates were collected after cooled overnight.

Substrate Preparation. Recycled silicon (100) was used for the depositions. Silicon pieces were cut to slides in a size of 1×6 (cm), and then the slides were sonicated in isopropanol for 30 minutes. Piranha solution (1:3 30% $\text{H}_2\text{O}_2/\text{H}_2\text{SO}_4$) was used for further cleaning, soaking for 1 hour. The slides were finally cleaned by deionized water. Distilled

water was used between each step of cleaning. The cleaned substrates were dried and stored in air at a 110°C oven before use.

Film Characterizations. Scanning electron microscopy (SEM, TescanVegaII XMU SEM), energy dispersive X-ray spectroscopy (EDS, Oxford Inca Energy 250X EDS), transmission electron microscopy (TEM, FEI Tecnai G2 F20 TEM) and selected area electron diffraction (SAED, Gatan ORIUS TEM CCD Camera) were completed at the Carleton University Nano Imaging Facility. Measurements of the SAED were performed by using GMS 3 software. X-ray photoelectric spectroscopy (XPS) was attained from a Specs/RHK multi-technique ultrahigh-vacuum system, with a XR-50 X-ray source (14.27 keV Al K α source) at University of Ottawa. The pressure during the investigation was controlled between 7×10^{-10} and 1×10^{-9} Torr. An Au-Al₂O₃ (100 nm) -Si (100) slide was used for calibration. The program CasaXPS was used to post-process the XPS data and Igor Pro 6.3 was utilized for plotting.

References

1. Gómez-Anquela, C.; García-Mendiola, T.; Abad, J. M.; Pita, M.; Pariente, F.; Lorenzo, E. Scaffold Electrodes Based on Thioctic Acid-Capped Gold Nanoparticles Coordinated Alcohol Dehydrogenase and Azure A Films for High Performance Biosensor. *Bioelectrochem.* **2015**, *106*, 335-342.
2. Zheng, P.; Li, M.; Jurevic, R.; Cushing, S. K.; Liu Y.; Wu, N. A Gold Nanohole Array Based Surface-Enhanced Raman Scattering Biosensor for Detection of Silver (I) and Mercury (II) in Human Saliva. *Nanoscale* **2015**, *7*, 11005-11012.
3. Mariani, S.; Scarano, S.; Spadavecchia, J.; Minunni, M. A Reusable Optical Biosensor for the Ultrasensitive and Selective Detection of Unamplified Human Genomic DNA with Gold Nanostars. *Biosens. Bioelectron.* **2015**, *74*, 981-988.
4. Mayer, K. M.; Shnipes, J.; Davis, D.; Walt D. R. Catalytic Kinetics of Single Gold Nanoparticles Observed via Optical Microwell Arrays. *Nanotechnology* **2015**, *26*, 055704.
5. Guo, H; Yan, X.; Zhi, Y.; Li, Z.; Wu, C.; Zhao, C.; Wang J.; Yu, Z.; Ding Y.; He, W.; Li, D. Nanostructuring Gold Wires as Highly Durable Nanocatalysts for Selective Reduction of Nitro Compounds and Azides with Organosilanes. *Nano Res.* **2015**, *8*, 1365-1372.
6. Moragues, A.; Neațu, F.; Pârvulescu, V. I.; Marcos, M. D.; Amorós, P.; Michelet, V. Heterogeneous Gold Catalyst: Synthesis, Characterization, and Application in 1, 4-Addition of Boronic Acids to Enones. *Catalyst* **2015**, *5*, 5060-5067.

7. Zhao, X.; Xue, J.; Mu, Z.; Huang, Y.; Lu, M.; Gu, Z. Gold Nanoparticle Incorporated Inverse Opal Photonic Crystal Capillaries for Optofluidic Surface Enhanced Raman Spectroscopy. *Biosens. Bioelectron.* **2015**, *72*, 268-274.
8. Wang, L.; Smith, K. W.; Dominguez-Medina, S.; Moody, N.; Olson, J. M.; Zhang, H.; Chang, W.; Kotov, N.; Link, S. Circular Differential Scattering of Single Chiral Self-Assembled Gold Nanorod Dimers. *ACS Photonics* **2015**, *2*, 1602-1610.
9. Zijlstra, P.; Paulo, P. M. R.; Orrit, M. Optical Detection of Single Non-Absorbing Molecules Using the Surface Plasmon Resonance of a Gold Nanorod. *Nat. Nanotechnol.* **2012**, *7*, 379-382.
10. Hou, W.; Cronin, S. B. A Review of Surface Plasmon Resonance-Enhanced Photocatalysis. *Adv. Funct. Mater.* **2013**, *23*, 1612-1619.
11. Qian, H.; Zhu, Y.; Jin, R. Atomically Precise Gold Nanocrystal Molecules with Surface Plasmon Resonance. *P. N. A. S.* **2012**, *109*, 696-700.
12. Bharadwaj, B.; Mukherji, S. Gold Nanoparticle Coated U-bend Fibre Optic Probe for Localized Surface Plasmon Resonance Based Detection of Explosive Vapours. *Sens. Actuators B Chem.* **2014**, *192*, 804-811.
13. Grzelczak, M.; Pe´rez-Juste, J.; Mulvaney, P.; Liz-Marz´an, L. Shape Control in Gold Nanoparticle Synthesis. *Chem. Soc. Rev.* **2008**, *37*, 1783-1791.
14. Wang, H.; Huff, T. B.; Zweifel, D. A.; He, W.; Low, P. S.; Wei, A.; Cheng, J. In Vitro and in Vivo Two-Photon Luminescence Imaging of Single Gold Nanorods. *P. N. A. S.* **2005**, *102*, 15752-15756.

15. Larsson, E. M.; Langhammer, C. Zorić, I.; Kasemo, B. Nanoplasmonic Probes of Catalytic Reactions. *Science* **2009**, *326*, 1091-1094.
16. Yavuz, M. S.; Cheng, Y.; Chen, J.; Cobley, C. M.; Zhang, Q.; Rycenga, M.; Xie, J.; Kim, C.; Song, K. H.; Schwartz, A. G.; Wang, L.; Xia, Y. Gold Nanocages Covered by Smart Polymers for Controlled Release with Near-Infrared Light. *Nat. Mater.* **2009**, *8*, 935-939.
17. Kim, S.; Jin, J.; Kim, Y. J.; Park, I. Y.; Kim, Y.; Kim, S. W. S. High-Harmonic Generation by Resonant Plasmon Field Enhancement. *Nature* **2008**, *453*, 757-760.
18. Hoffmann, B.; Bashouti, M. Y.; Feichtner, T.; Mačković, M.; Dieker, C.; Salaheldin, A. M.; Richter, P.; Gordan, O. D.; Zahn, D. R. T.; Spiecker, E.; Christiansen, S. New Insights into Colloidal Gold Nanoplates: Structural Investigation, Micro-Ellipsometry and Thinning Procedure towards Ultrathin Monocrystalline Layers. *Nanoscale* **2016**, *8*, 4529-4536.
19. Huang, J.; Callegari, V.; Geisler, P.; Brüning, C.; Kern, J.; Prangma, J. C.; Wu, X.; Feichtner, T.; Ziegler, J.; Weinmann, P.; Kamp, M.; Forchel, A.; Biagioni, P.; Sennhauser, U.; Hecht, B. Atomically Flat Single-Crystalline Gold Nanostructures for Plasmonic Nanocircuitry. *Nat. Commun.* **2010**, *1*, 150.
20. Kawasaki, M.; Masuda, K. Laser Fragmentation of Water-Suspended Gold Nanoplates via Spherical Submicroparticles to Fine Nanoparticles. *J. Phys. Chem. B* **2005**, *109*, 9379-9388.

21. Wang, J.; Chen, Z.; Hu, Y.; Jiang, X.; Chen D.; Zhang, W. Flaky Silver Powders Prepared with Nanofilm Transition Method: Application for Printable Electronics. *J. Mater. Chem. C* **2013**, *1*, 230-233.
22. Wang, W.; Cui, H. Chitosan-Luminol Reduced Gold Nanoflowers: from One-Pot Synthesis to Morphology-Dependent SPR and Chemiluminescence Sensing. *J. Phys. Chem. C* **2008**, *112*, 10759-10766.
23. Dinda, E.; Si, S.; Kotal, A.; Mandal, T. K. Novel Ascorbic Acid Based Ionic Liquids for the In Situ Synthesis of Quasi-Spherical and Anisotropic Gold Nanostructures in Aqueous Medium. *Chem. A Eur. J.* **2008**, *14*, 5528-5537.
24. Duan, G.; Cai, W.; Luo, Y.; Li, Z.; Li, Y. Electrochemically Induced Flowerlike Gold Nanoarchitectures and Their Strong Surface-Enhanced Raman Scattering Effect. *Appl. Phys. Lett.* **2006**, *89*, 211905.
25. Jiang, Y.; Wu, X. Li, Q.; Li, J.; Xu, D. Facile Synthesis of Gold Nanoflowers with High Surface-Enhanced Raman Scattering Activity. *Nanotechnology* **2011**, *22*, 385601.
26. Brust, M.; Bethell, D.; Kiely, C. J.; Schiffrin, D. J. Self-Assembled Gold Nanoparticle Thin Films with Nonmetallic Optical and Electronic Properties. *Langmuir* **1998**, *14*, 5425-5429.
27. Sun, X.; Dong, S.; Wang, E. Large-Scale Synthesis of Micrometer-Scale Single-Crystalline Au Plates of Nanometer Thickness by a Wet-Chemical Route. *Angew. Chem. Int. Ed.* **2004**, *116*, 6360-6363.

28. Ah, C.; Yun, Y.; Park, H.; Kim, W.; Ha, D.; Yun, W. Size-Controlled Synthesis of Machinable Single-crystalline Gold Nanoplates. *Chem. Mater.* **2005**, *17*, 5558-5561.
29. Zhang, J.; Liu, H.; Wang, Z.; Ming, N. Shape-Selective Synthesis of Gold Nanoparticles with Controlled Sizes, Shapes, and Plasmon Resonances. *Adv. Funct. Mater.* **2007**, *17*, 3295-3303.
30. Huang, Y.; Ferhan, A. R.; Gao, Y.; Dandapat, A.; Kim, D. High-Yield Synthesis of Triangular Gold Nanoplates with Improved Shape Uniformity, Tunable Edge Length and Thickness. *Nanoscale* **2014**, *6*, 6496-6500.
31. Qin, F.; Zhao, T.; Jiang, R.; Jiang, N.; Ruan, Q.; Wang, J. Sun, L.; Yan, C.; Lin, H. Thickness Control Produces Gold Nanoplates with Their Plasmon in the Visible and Near-Infrared Regions. *Adv. Optical Mater.* **2016**, *4*, 76-85.
32. Griffiths, M. B. E.; Koponen, S. E.; Mandia, D. J.; McLeod, J. F.; Coyle, J. P.; Sims, J. J.; Giorgi, J. B.; Sirianni, E. R.; Yap, G. P. A.; Barry, S. T. Surfactant Directed Growth of Gold Metal Nanoplates by Chemical Vapor Deposition. *Chem. Mater.* **2015**, *27*, 6116-6124.
33. Hampden-Smith, M. J.; Kudas, T. T. Chemical Vapor Deposition of Metals: Part 1. An Overview of CVD Processes. *Chem. Vap. Deposition* **1995**, *1*, 8-23.
34. Quinto, D. T. Technology Perspective on CVD and PVD Coated Metal-Cutting Tools. *Int. J. Refract. Met. H.* **1996**, *14*, 7-20.
35. Jensen, K. F.; Kern, W. *Thin Film Processes II*. New York: Academic Press, **1991**.

36. Narayanaswamy, A.; Xu, H.; Pradhan, N.; Peng, X. Crystalline Nanoflowers with Different Chemical Compositions and Physical Properties Grown by Limited Ligand Protection. *Angew. Chem.* **2006**, *118*, 5487-5490.
37. Tao, B.; Boykin, D. W. Simple Amine/Pd (OAc)₂-Catalyzed Suzuki Coupling Reactions of Aryl Bromides under Mild Aerobic Conditions. *J. Org. Chem.* **2004**, *69*, 4330-4335.
38. Ramirez, E.; Jansat, S.; Philippot, K.; Lecante, P.; Gomez, M.; Masdeu-Bultó, A. M.; Chaudret, B. Influence of Organic Ligands on the Stabilization of Palladium Nanoparticles. *J. Organomet. Chem.* **2004**, *689*, 4601-4610.
39. Koponen, E. S. B. Sc. Gold Film by Chemical Vapor Deposition. Thesis, Carleton University, Ottawa, ON, April 2014.
40. Crowell, J. E. Chemical Methods of Thin Film Deposition: Chemical Vapor Deposition, Atomic Layer Deposition, and Related Technologies. *J. Vac. Sci. Technol. A.* **2003**, *21*, S88-S95.
41. Tao, A. R.; Habas, S.; Yang, P. Shape Control of Colloidal Metal Nanocrystals. *Small* **2008**, *4*, 310-325.
42. Yacaman, M. J.; Ascencio, J. A.; Liu H.; Gardea-Torresdey, J. Structure Shape and Stability of Nanometric Sized Particles. *J. Vac. Sci. Technol. B* **2001**, *19*, 1091-1103.
43. Ino, S. Stability of Multiply-Twinned Particles. *J. Phys. Soc. Jpn.* **1969**, *27*, 941-953.

44. Elechiguerra, J. L.; Reyes-Gasgab, J.; Yacaman, M. The Role of Twinning in Shape Evolution of Anisotropic Noble Metal Nanostructures. *J. Mater. Chem.* **2006**, *16*, 3906-3919.
45. Salzemann, C.; Lisiecki, I.; Urban, J.; Pileni, M. -P. Anisotropic Copper Nanocrystals Synthesized in a Supersaturated Medium: Nanocrystal Growth. *Langmuir* **2004**, *20*, 11772-11777.
46. Marks, L. D.; Smith, D. J. High Resolution Studies of Small Particles of Gold and Silver: I. Multiply-Twinned Particles. *J. Cryst. Growth* **1981**, *54*, 425-432.
47. Marks, L. D. Surface Structure and Energetics of Multiply Twinned Particles. *Philos. Mag. A.* **1984**, *49*, 81-93.
48. Marks, L. D. Experimental Studies of Small Particle Structures. *Rep. Prog. Phys.* **1994**, *57*, 603-649.
49. Wang, J.; Narayanan, S.; Huang, J.; Zhang, Z.; Zhu, T.; Mao, S. Atomic-Scale Dynamic Process of Deformation-Induced Stacking Fault Tetrahedra in Gold Nanocrystals. *Nat. Commun.* **2013**, *4*, 2340.
50. Smith, D. J.; Petford-Long, A. K.; Wallenberg, L. R.; Bovin, J. O. Dynamic Atomic-Level Rearrangements in Small Gold Particles. *Science* **1986**, *233*, 872-875.
51. Kuhlmann-Wilsdorf, D. The Growth and Annealing of Stacking Fault Tetrahedra. *Acta Metall.* **1965**, *13*, 257-270.
52. Ahmadi, T. S.; Wang, Z.; Henglein, A.; El-sayed, M. A. "Cubic" Colloidal Platinum Nanoparticles. *Chem. Mater.* **1996**, *8*, 1161-1163.

53. Filankembo, A.; Giorgio, S.; Lisiecki, I.; Pileni, M. P. Is the Anion the Major Parameter in the Shape Control of Nanocrystals? *J. Phys. Chem. B* **2003**, *107*, 7492-7500.
54. Sun, Y.; Xia, Y. Shape-Controlled Synthesis of Gold and Silver Nanoparticles. *Science* **2002**, *298*, 2176-2179.
55. Chirea, M.; Freitas, A.; Vasile, B. S.; Ghitulica, C.; Pereira, C. M.; Silva, F. Gold Nanowire Networks: Synthesis, Characterization, and Catalytic Activity. *Langmuir* **2011**, *27*, 3906-3913.
56. Liu, Z.; Searson, P. C. Single Nanoporous Gold Nanowire Sensors. *J. Phys. Chem. B* **2006**, *110*, 4318-4322.
57. Karim, S.; Toimil-Molares, M. E.; Maurer, F.; Mische, G.; Ensinger, W.; Liu, J.; Cornelius, T. W.; Neumann, R. Synthesis of Gold Nanowires with Controlled Crystallographic Characteristics. *Appl. Phys. A* **2006**, *84*, 403-407.
58. Lofton C.; Sigmund, W. Mechanisms Controlling Crystal Habits of Gold and Silver Colloids. *Adv. Funct. Mater.* **2005**, *15*, 1197-1208.
59. Kirkland, A. I.; Jefferson, D. A.; Duff, D. G.; Edwards, P. P.; Gameson, I.; Johnson, B. F. G.; Smith, D. Structural Studies of Trigonal Lamellar Particles of Gold and Silver. *J. Proc. R. Soc. London, Ser. A* **1993**, *440*, 589-609.
60. Hwang, E.; Lee, J. Surfactant-Assisted Metallorganic CVD of (111) -Oriented Copper Films with Excellent Surface Smoothness. *Electrochem. Solid-State Lett.* **2000**, *3*, 138-140.

61. Bögels, G.; Buijnsters, J. G.; Verhaegen, S. A. C.; Meekes, H.; Bennema, P.; Bollen, D. Morphology and Growth Mechanism of Multiply Twinned AgBr and AgCl Needle Crystals. *J. Cryst. Growth* **1999**, *203*, 554-563.
62. Wang, Z.; Gao, R.; Nikoobakht, B.; El-Sayed, M. A. Surface Reconstruction of the Unstable {110} Surface in Gold Nanorods. *J. Phys. Chem. B* **2000**, *104*, 5417-5420.
63. Mahmoud, M. A.; Tabor, C. E.; El-Sayed, M. A.; Ding, Y.; Wang, Z. A New Catalytically Active Colloidal Platinum Nanocatalyst: the Multiarmed Nanostar Single Crystal. *J. Am. Chem. Soc.* **2008**, *130*, 4590-4591.
64. Miao, X.; Wang, T.; Chai, F.; Zhang, X.; Wang, C.; Sun, W. A Facile Synthetic Route for the Preparation of Gold Nanostars with Magnetic Cores and Their Reusable Nanohybrid Catalytic Properties. *Nanoscale* **2011**, *3*, 1189-1194.
65. Kumar, P. S.; Pastoriza-Santos, I.; Rodríguez-González, B.; De Abajo, F. J. G.; Liz-Marzan, L. M. High-Yield Synthesis and Optical Response of Gold Nanostars. *Nanotechnology* **2007**, *19*, 015606.
66. Niu, W.; Chua, Y. A. A.; Zhang, W.; Huang, H.; Lu, X. Highly Symmetric Gold Nanostars: Crystallographic Control and Surface-Enhanced Raman Scattering Property. *J. Am. Chem. Soc.* **2015**, *137*, 10460-10463.
67. Zhang, L.; Zhang, J.; Kuang, Q.; Xie, S.; Jiang, Z.; Xie, Z.; Zheng, L. Cu²⁺-Assisted Synthesis of Hexoctahedral Au-Pd Alloy Nanocrystals with High-Index Facets. *J. Am. Chem. Soc.* **2011**, *133*, 17114-17117.

68. Hong, J.; Lee, S.; Lee, Y.; Han, S. Hexoctahedral Au nanocrystals with High-Index Facets and Their Optical and Surface-Enhanced Raman Scattering Properties. *J. Am. Chem. Soc.* **2012**, *134*, 4565-4568.
69. Hao, E.; Bailey, R. C.; Schatz, G. C.; Hupp, J. T.; Li, S. Synthesis and Optical Properties of “Branched” Gold Nanocrystals. *Nano Lett.* **2004**, *4*, 327-330.
70. Jönsson, A. S.; Jönsson, B. The Influence of Nonionic and Ionic Surfactants on Hydrophobic and Hydrophilic Ultrafiltration Membranes. *J. Membrane Sci.* **1991**, *56*, 49-76.
71. Halder, A.; Ravishankar, N. Ultrafine Single-Crystalline Gold Nanowire Arrays by Oriented Attachment. *Adv. Mater.* **2007**, *19*, 1854-1858.
72. Krichevski, O.; Tirosh, E.; Markovich, G. Formation of Gold-Silver Nanowires in Thin Surfactant Solution Films. *Langmuir* **2006**, *22*, 867-870.
73. Nikoobakht, B.; El-Sayed, M. A. Preparation and Growth Mechanism of Gold Nanorods (NRs) Using Seed-Mediated Growth Method. *Chem. Mater.* **2003**, *15*, 1957-1962.
74. Nikoobakht, B.; El-Sayed, M. A. Evidence for Bilayer Assembly of Cationic Surfactants on the Surface of Gold Nanorods. *Langmuir* **2001**, *17*, 6368-6374.
75. Jana, N. R.; Gearheart, L.; Murphy, C. J. Wet Chemical Synthesis of High Aspect Ratio Cylindrical Gold Nanorods. *J. Phys. Chem. B* **2001**, *105*, 4065-4067.

76. Wu, H.; Chen, C.; Huang, M. Seed-Mediated Synthesis of Branched Gold Nanocrystals Derived from the Side Growth of Pentagonal Bipyramids and the Formation of Gold Nanostars. *Chem. Mater.* **2008**, *21*, 110-114.
77. Ha, T.; Kim, Y.; Park, S. Complete Separation of Triangular Gold Nanoplates through Selective Precipitation under CTAB Micelles in Aqueous Solution. *Chem. Commun.* **2010**, *46*, 3164-3166.
78. Chu, H.; Kuo, C.; Huang, M. Thermal Aqueous Solution Approach for the Synthesis of Triangular and Hexagonal Gold Nanoplates with Three Different Size Ranges. *Inorg. Chem.* **2006**, *45*, 808-813.
79. He, X.; Zhao, X.; Chen, Y.; Feng, J. The Evidence for Synthesis of Truncated Triangular Silver Nanoplates in the Presence of CTAB. *Mater. Charact.* **2008**, *59*, 380-384.
80. Wang, Z.; Yuan, J.; Han, D.; Zhang, Y.; Shen, Y.; Kuehner, D.; Niu, L.; Ivaska, A. Simultaneous Synthesis of Polyaniline Nanotubules and Gold Nanoplates. *Cryst. Growth Des.* **2008**, *8*, 1827-1832.
81. Jiang, P.; Zhou, J.; Li, R.; Gao, Y.; Sun, T.; Zhao, X.; Xiang, W.; Xie, S. PVP-Capped Twinned Gold Plates from Nanometer to Micrometer. *J. Nanopart. Res.* **2006**, *8*, 927-934.
82. Tsuji, M.; Hashimoto, M.; Nishizawa, Y.; Tsuji, T. Preparation of Gold Nanoplates by a Microwave-Polyol Method. *Chem. Lett.* **2003**, *32*, 1114-1115.

83. Bi, L.; Rao, Y.; Tao, Q.; Dong, J.; Su, T.; Liu, F.; Qian, W. Fabrication of Large-Scale Gold Nanoplate Films as Highly Active SERS Substrates for Label-Free DNA Detection. *Biosens. Bioelectron.* **2013**, *43*, 193-199.
84. Bullen, C.; Zijlstra, P.; Bakker, E.; Gu, M.; Raston, C. Chemical Kinetics of Gold Nanorod Growth in Aqueous CTAB Solutions. *Cryst. Growth Des.* **2011**, *11*, 3375-3380.
85. Diao, J.; Gall, K.; Dunn, M. L. Atomistic Simulation of the Structure and Elastic Properties of Gold Nanowires. *J. Mech. Phys. Solids* **2004**, *52*, 1935-1962.
86. Park, H.; Zimmerman, J. A. Modeling Inelasticity and Failure in Gold Nanowires. *Phys. Rev. B* **2005**, *72*, 054106.
87. Tosatti, E.; Prestipino, S.; Kostlmeier, S.; Dal Corso, A.; Di Tolla, F. D. String Tension and Stability of Magic Tip-Suspended Nanowires. *Science* **2001**, *291*, 288-290.
88. Kou, X.; Zhang, S.; Tsung, C.; Yeung, M.; Shi, Q.; Stucky, G. D.; Sun, L.; Wang, J.; Yan, C. Growth of Gold Nanorods and Bipyramids Using CTEAB Surfactant. *J. Phys. Chem. B* **2006**, *110*, 16377-16383.
89. Kim, F.; Sohn, K.; Wu, J.; Huang, J. Chemical Synthesis of Gold Nanowires in Acidic Solutions. *J. Am. Chem. Soc.* **2008**, *130*, 14442-14443.
90. Jia, J.; Wang, B.; Wu, A.; Cheng, G.; Li, Z.; Dong, S. A Method to Construct a Third-Generation Horseradish Peroxidase Biosensor: Self-Assembling Gold Nanoparticles to Three-Dimensional Sol-Gel Network. *Anal. Chem.* **2002**, *74*, 2217-2223.

91. Brust, M.; Walker, M.; Bethell, D.; Schiffrin, D. J.; Whyman, R. Synthesis of Thiol-Derivatised Gold Nanoparticles in a Two-Phase Liquid–Liquid System. *J. Chem. Soc. Chem. Commun.* **1994**, 7, 801-802.
92. Jana, N. R.; Gearheart, L.; Murphy, C. J. Wet Chemical Synthesis of High Aspect Ratio Cylindrical Gold Nanorods. *J. Phys. Chem. B* **2001**, 105, 4065-4067.
93. Fink, J.; Kiely, C. J.; Bethell, D.; Schiffrin, D. J. Self-Organization of Nanosized Gold Particles. *Chem. Mater.* **1998**, 10, 922-926.
94. Reimers, J. R.; Wang, Y.; Cankurtaran, B. O.; Ford, M. J. Chemical Analysis of the Superatom Model for Sulfur-Stabilized Gold Nanoparticles. *J. Am. Chem. Soc.* **2010**, 132, 8378-8384.
95. Häkkinen, H. The Gold-Sulfur Interface at the Nanoscale. *Nat. Chem.* **2012**, 4, 443-455.
96. Pensa, E.; Cortés, E.; Corthey, G.; Carro, P.; Vericat, C.; Fonticelli, M. H.; Bentitez, G.; Rubert, A. A.; Salvarezza, R. C. The Chemistry of the Sulfur-Gold Interface: in Search of a Unified Model. *Accounts Chem. Res.* **2012**, 45, 1183-1192.
97. Huo, Z.; Tsung, C.; Huang, W.; Zhang, X.; Yang, P. Sub-Two Nanometer Single Crystal Au Nanowires. *Nano Lett.* **2008**, 8, 2041-2044.

98. Hostetler, M. J.; Wingate, J. E.; Zhong, C.; Harris, J. E.; Vachet, R. W.; Clark, M. R.; Londono, J. D.; Green, S. J.; Stokes, J. J.; Wignall, G. D.; Glish, G. L.; Porter, M. D.; Evans, N. D.; Murray, R. W. Alkanethiolate Gold Cluster Molecules with Core Diameters from 1.5 to 5.2 nm: Core and Monolayer Properties as a Function of Core Size. *Langmuir* **1998**, *14*, 17-30.
99. Fu, X.; Shen, W.; Yao, T.; Hou, W. *Physical Chemistry*. Beijing: Higher Education Press. **2005**.
100. Hata, K.; Futaba, D. N.; Mizuno, K.; Namai, T.; Yumura, M.; Iijima, S. Water-Assisted Highly Efficient Synthesis of Impurity-Free Single-Walled Carbon Nanotubes. *Science* **2004**, *306*, 1362-1364.
101. Scherer, G. W. Drying Gels: I. General theory. *J. Non-Cryst. Solids* **1986**, *87*, 199-225.
102. Pam pach, R.; Haberkc, K. *Ceramic Powders*. Amsterdam: Elsevier Scientific Pub. Company, **1983**.
103. Karlstroem, G.; Carlsson, A.; Lindman, B. Phase Diagrams of Nonionic Polymer-Water Systems: Experimental and Theoretical Studies of the Effects of Surfactants and Other Cosolutes. *J. Phys. Chem.* **1990**, *94*, 5005-5015.
104. Yang, Z.; Han, N.; Fang, M.; Lin, H.; Cheung, H.; Yip, S. Wang, E.; Hung, F.; Wong, C.; Ho, J. C. Surfactant-Assisted Chemical Vapour Deposition of High-Performance Small-Diameter GaSb Nanowires. *Nat. Commun.* **2014**, *5*.

105. Panda, S. K.; Datta, A.; Dev, A.; Gorai, S.; Chaudhuri, S. Surfactant-Assisted Synthesis of SnS Nanowires Grown on Tin Foils. *Cryst. Growth Des.* **2006**, *6*, 2177-2181.
106. Palgrave, R. G.; Parkin, I. P. Surfactant Directed Chemical Vapour Deposition of Gold Nanoparticles with Narrow Size Distributions. *Gold Bull.* **2008**, *41*, 66-69.
107. Jadzinsky, P. D.; Calero, G.; Ackerson, C. J.; Bushnell, D. A.; Kornberg, R. D. Structure of a Thiol Monolayer-Protected Gold Nanoparticle at 1.1 Å Resolution. *Science* **2007**, *318*, 430-433.
108. Krüger, D.; Fuchs, H.; Rousseau, R.; Marx, D.; Parrinello, M. Pulling Monatomic Gold Wires with Single Molecules: an *Ab Initio* Simulation. *Phys. Rev. Lett.* **2002**, *89*, 186402.
109. Ocko, B. M.; Watson, G. M.; Wang, J. Structure and Electrocompression of Electrodeposited Iodine Monolayers on Gold (111). *J. Phys. Chem.* **1994**, *98*, 897-906.
110. Cheng, W.; Dong, S.; Wang, E. Iodine-Induced Gold-Nanoparticle Fusion/ Fragmentation/ Aggregation and Iodine-Linked Nanostructured Assemblies on a Glass Substrate. *Angew. Chem. Int. Edit.* **2003**, *42*, 449-452.
111. Atkins, P.; Paula, J. d. *Physical Chemistry* New York: W. H. Freeman. **2014**.
112. Chapman, S.; Cowling, T. G. *The Thermo Mathematical Theory of Non-uniform Gases: an Account of the Kinetic Theory of Viscosity, Thermal Conduction and Diffusion in Gases*. Cambridge: Cambridge University Press. **1970**.

113. Laurendeau, N. M. *Statistical Thermodynamics: Fundamentals and Applications*. Cambridge: Cambridge University Press. **2005**.
114. Vanhove, G.; Yu, Y.; Boumehdi, M. A.; Frottier, O.; Herbinet, O.; Glaude, P. A.; Battin-Leclerc, F. Experimental Study of Tetrahydrofuran Oxidation and Ignition in Low-Temperature Conditions. *Energy Fuels* **2015**, *29*, 6118-6125.
115. Binnig, G.; Quate, C. F.; Gerber C. Atomic Force Microscope. *Phys. Rev. Lett.* **1986**, *56*, 930.
116. Binnig, G.; Rohrer, H.; Gerber, C.; Weibel, E. Surface Studies by Scanning Tunneling Microscopy. *Phys. Rev. Lett.* **1982**, *49*, 57.
117. Singh, A.; Ranganathan, S. On the Indexing and Reciprocal Space of Icosahedral Quasicrystal. *J. Mater. Res.* **1999**, *14*, 4182-4187.
118. Fan, R.; Chew, S. W.; Cheong, V. V.; Orner, B. P. Fabrication of Gold Nanoparticles Inside Unmodified Horse Spleen Apoferritin. *Small* **2010**, *6*, 1483-1487.
119. Yamamoto, M.; Kashiwagi, Y.; Sakata, T.; Mori, H.; Nakamoto, M. Synthesis and morphology of star-shaped gold nanoplates protected by poly (N-vinyl-2-pyrrolidone). *Chem. Mater.* **2005**, *17*, 5391-5393.
120. Heyraud, J. C.; Metois, J. J. Anomalous $1/3$ 422 Diffraction Spots from {111} Flat Gold Crystallites: (111) Surface Reconstruction and Moire Fringes between the Surface and the Bulk. *Surf. Sci.* **1980**, *100*, 519-528.
121. Weast, R. C. *CRC Handbook of Chemistry and Physics*. Boca Raton: Chemical Rubber Company. **1984**.

122. Reimers, J. R.; Ford, M. J.; Halder, A.; Ulstrup, J.; Hush, N. S. Gold Surfaces and Nanoparticles are Protected by Au (0) -Thiyl Species and are Destroyed when Au (I) -Thiolates Form. *P. N. A. S.* **2016**, *113*, E1424-E1433.
123. Pauling, L. The Nature of the Chemical Bond. IV. The Energy of Single Bonds and the Relative Electronegativity of Atoms. *J. Am. Chem. Soc.* **1932**, *54*, 3570–3582.
124. Shadnam, M. R.; Amirfazli, A. Kinetics of Alkanethiol Monolayer Desorption from Gold in Air. *Chem. Commun.* **2005**, 4869-4871.
125. Hutt, D. A.; Leggett, G. J. Desorption of Butanethiol from Au (111) during Storage in Ultrahigh Vacuum: Effects on Surface Coverage and Stability toward Displacement by Solution-Phase Thiols. *Langmuir* **1997**, *13*, 3055-3058.
126. Usón, R.; Laguna, A. M.; Briggs, D. A.; Murray, H. H.; Fackler, J. P. (Tetrahydrothiophene) Gold (I) or Gold (III) Complexes. *Inorg. Synth.* **1989**, *26*, 85-91.
127. Lappert, M. F.; Slade, M. J.; Singh, A.; Atwood, J. L.; Rogers, R. D.; Shakir, R. Structure and Reactivity of Sterically Hindered Lithium Amides and Their Diethyl Etherates: Crystal and Molecular Structures of $[\text{Li}\{\text{N}(\text{SiMe}_3)_2\}(\text{OEt}_2)]_2$ and Tetrakis (2,2,6,6-Tetramethylpiperidinato)lithium). *J. Am. Chem. Soc.* **1983**, *105*, 302-304.